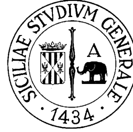

UNIVERSITÀ DEGLI STUDI DI CATANIA

IN CONVENZIONE CON

UNIVERSITÀ DEGLI STUDI DI PALERMO

DOTTORATO DI RICERCA IN

SCIENZA DEI MATERIALI E NANOTECNOLOGIE - XXXII CICLO

MONIA SPERA

OHMIC CONTACTS ON WIDE BAND GAP SEMICONDUCTORS

TUTOR:

PROF. MARCO CANNAS (UNIVERSITÀ DEGLI STUDI DI PALERMO)

DOTT. FABRIZIO ROCCAFORTE (CNR-IMM, CATANIA)

COORDINATORE: PROF.SSA MARIA GRAZIA GRIMALDI

TESI PER IL CONSEGUIMENTO DEL TITOLO DI DOTTORE DI RICERCA

Contents

Introduction 1
Chapter 1 - Properties of wide band gap semiconductors 5
1.1 Material properties 5
1.1.1 SiC crystalline structure 5
1.1.2 GaN crystalline structure 8
1.1.3 Substrates for the growth 9
1.1.4 Electronic properties 11
1.1.5 AlGaN/GaN heterostructures 14
1.2 Advantages of SiC and GaN for power electronics applications 22
1.3 Scientific and technological open issues related to SiC and GaN materials and devices 27
Chapter 2 – Background on metal/semiconductor contacts 31
2.1 Schottky barrier and current transport mechanisms 31
2.2 Ohmic contacts 35
Chapter 3 - Experimental techniques 39
3.1 Morphological, structural and optical characterization. 39
3.1.1 Atomic Force Microscopy (AFM) and Conductive AFM 39
3.1.2 X-Ray diffraction (XRD) 43
3.1.3 Transmission electron microscopy (TEM) 45
3.1.4 Photoluminescence Spectroscopy 47
3.2 Electrical characterization 48
3.2.1 Transmission Line Model (TLM) 48
3.2.2 Van der Pauw and Hall-effect measurements 52
3.3 Fabrication of test patterns for electrical characterization 56
Chapter 4 – Ohmic contacts on AlGaN/GaN heterostructures 61
4.1. State of the art on Ohmic contacts on AlGaN/GaN heterostructures 61

4.2. Characterization of the AlGaN/GaN heterostructures 64
4.3 Ti- and Ta- based Ohmic contacts on AlGaN/GaN heterostructures 68
4.4 Effects of layer thickness and annealing time on Ti- based contacts 77
4.5 Modification of the sheet resistance under Ohmic contacts on AlGaN/GaN heterostructures 82
Chapter 5 – Ohmic contacts on Silicon Carbide materials 91
5.1 Ohmic contacts on p-type implanted 4H-SiC 91
5.1.1. State of the art on implantation doping and Ohmic contacts on p-type 4H-SiC 91
5.1.2 Electrical activation of the p-type dopant after high temperature annealing 93
5.1.3 Study of Ti/Al/Ni Ohmic contacts on p-type implanted 4H-SiC 105
5.2 Ohmic contacts on 3C-SiC 109
5.2.1. State of the art on Ohmic contacts on 3C-SiC 109
5.2.2 Ohmic contacts on n-type 3C-SiC 110
5.2.3 Ohmic contacts on p-type 3C-SiC 114
Conclusion and outlook 121
Glossary 127
Curriculum Vitae 131
Acknowledgments 137
References 141

Introduction

In our industrialized world, the energy consumption is constantly increasing. Moreover, in spite of the efforts to save energy, the global demand for electricity will grow significantly in the next two decades. For that reason, energy saving and energy efficiency have become very important objectives of our society.

Power electronics is the key technology that controls the distribution and conversion of electrical energy from the source to the end user. Hence, power electronics regulates the power supply infrastructure, energy transmission and distribution systems, finding a large variety of applications in industry, transportation, renewable energy, home appliances, etc.

The origin of modern power electronics is commonly associated with the invention of transistors at the end of the 40s. Since then, semiconductor materials became available and solid-state devices started replacing the old vacuum tubes. At the beginning of this revolution, solid-state electronic devices were based on germanium, but this material was quickly replaced by silicon (Si), which remained for more than five decades the semiconductor of choice for power devices. However, some intrinsic properties of silicon (e.g., low critical electric field, low thermal conductivity, narrow bandgap) represent a limitation for the performance and the efficiency of power devices. Hence, the introduction of new semiconductor materials, enabling an improvement of the energy efficiency in power electronics devices, has become mandatory.

To this aim, Wide Band Gap (WBG) semiconductors are very promising to improve the performance of electronic devices, decreasing the power consumption. In particular, gallium nitride (GaN) and silicon carbide (SiC) are emerging in many applications, such as industry, transportation (i.e. power supply and power modules), renewable energies (power conversion) and aerospace (high temperature engines). The advantages offered by these semiconductors with respect to the traditional silicon reside in their intrinsic physical properties, such as a high breakdown field, a low intrinsic carrier concentration, a high saturation velocity and thermal conductivity.

However, the physical differences with respect to silicon make the technology of WBG devices definitively more complex.
Ohmic contacts are fundamental building blocks in microelectronics and optoelectronics devices, as they are the connection from the device to the external circuitry. The performance of a device strongly depends on the good operation of such contacts. Hence, it is important to understand the physics that governs the charge transport at these metal/semiconductor interfaces.

SiC is currently the most advanced WBG semiconductor, and it is today available in large area wafers (up to 150 mm in diameter) of good crystalline quality. This material is present in nature in different crystal structures, called polytypes. The hexagonal 4H-SiC and the cubic 3C-SiC are the emerging polytypes for high power and high temperature applications. Today many 4H-SiC devices, like Schottky diodes, or metal oxide semiconductor field effect transistors (MOSFETs) are commercially available and offer superior properties with respect to Si devices. For these devices, understanding the transport properties at metal/SiC interfaces is very important, either for Schottky or Ohmic contacts.

On the other hand, GaN is a fascinating material, well-known for the Nobel Prize for Physics assigned in 2014 for the research on light emitting diodes (LEDs). This material can be also interesting for power electronics applications. A peculiarity of GaN is the possibility to grow AlGaN/GaN heterostructures. In such systems, in the presence of a strained thin AlGaN layer, the gradient of piezoelectric and spontaneous polarization leads to the formation of a two-dimensional electron gas (2DEG) confined at the AlGaN/GaN interface. These heterostructures are employed in the fabrication of lateral devices called high electron mobility transistors (HEMTs), which are based on the presence of the 2DEG. One important issue of GaN HEMT technology is the formation of Ohmic contacts with low specific resistance on the AlGaN/GaN heterostructures for the source and drain electrodes. Moreover, in GaN-on-Si technology, it is important to have Au-free contacts. The electrical properties of such contacts depends on several parameters, and the current transport mechanisms in Au-free metallization are still under investigation.

In this thesis, some physical aspect related to Ohmic contacts on SiC and AlGaN/GaN heterostructures have been studied, employing several

morphological, structural and electrical characterizations. The aim of the work is to clarify some fundamental open questions on the transport mechanisms at the metal/semiconductor interfaces, which are also useful for the device technology.

The thesis is composed of five chapters. The first part of the thesis introduces the semiconductor properties, the basis physics related to metal/semiconductor interfaces and the experimental techniques.

Chapter 1 introduces the WBG semiconductors, which are object of this study. In particular, the crystalline structure and the electrical properties of 3C-SiC, 4H-SiC and GaN (focusing also on the AlGaN/GaN heterostructure) are presented, highlighting the advantages of these semiconductors with respect to the traditional silicon (Si).

Then, as this research work has been focused on Ohmic contacts, Chapter 2 reports some basic physical concepts useful for the comprehension of metal/semiconductor contacts and current transport mechanisms at these interfaces.

Chapter 3 synthetically describes the characterization techniques used in this thesis. Atomic Force Microscopy (AFM) and conductive atomic force microscopy (C-AFM) were used for morphological and nanoscale electrical characterization. X-Ray Diffraction (XRD) and Transmission Electron Microscopy (TEM) served for a structural analysis of the annealed contacts. Hall Effect measurements and current-voltage (I-V) measurements allowed the determination of the electrical properties of the semiconductor layers and the Ohmic contacts formed on them. The electrical characterizations required the fabrication of appropriate test patterns (e.g., TLM structures, VdP structures, etc.) in the clean room. The fabrication procedures are also described in the chapter.

The second part of the thesis reports the experimental results and their discussion.

Chapter 4 is focused on AlGaN/GaN heterostructures, and reports a study of Au-free Ohmic contacts, based on Ti and Ta metallization. In particular, the structural, morphological and electrical behaviour of Ti/Al/Ti and Ta/Al/Ta systems are compared, providing insights on the carrier transport mechanism at the different metal/semiconductor interfaces.

Chapter 5 reports on Ohmic contacts to SiC materials. The chapter is divided in two parts. First, the study of Ti/Al-based Ohmic contacts on p-type implanted 4H-SiC is reported together with the study of the electrical activation of the p-type implanted dopant by means of Hall Effect measurements. Then, the chapter presents an investigation on Ni- and Ti-based contacts on n-type and p-type cubic 3C-SiC.

Finally, a short chapter summarizes the main results of the work, giving some conclusion and an outlook for future research work on this topic.

Chapter 1 - Properties of wide band gap semiconductors

This chapter gives an introduction on the main properties of the wide band gap (WBG) semiconductors silicon carbide (SiC) and gallium nitride (GaN). After a short illustration of the crystalline structure of the two materials, particular attention will be given to the electronics properties and their impact on the performances of power devices. The advantages of using SiC and GaN with respect to the traditional silicon (Si) devices will be also highlighted.

1.1 Material properties

1.1.1 SiC crystalline structure

Silicon carbide (SiC) is a binary compound semiconductor formed up by group IV elements, carbon (C) and silicon (Si), tetrahedrally bonded in a 1:1 ratio [1,2]. Each Si atom shares electrons with four C atoms with a partially ionic (12%) – covalent (88%) bond. Fig. 1.1 (a) shows the basic structural unit, a tetrahedron having one C (or Si) atom in the centre surrounded by four Si (or C) atoms, with a C-Si binding energy of about 5 eV. The approximate distances between Si-C and Si-Si or C-C atoms are 1.89 Å and 3.08 Å, respectively. SiC can be present in nature in different stable crystal structures, called *polytypes*, having the same chemical composition (50% of Si and 50% of C), and equal basic tetrahedral structure, i.e., four atoms of Si (or C) linked to one C (or Si) atom. The various polytypes can exist in cubic (Fig. 1.1 (b)), hexagonal (Fig. 1.1 (c)), and rhombohedral crystal structures, all of them crystallize according to the laws of close spherical packing, resulting in binary structures constituted by identical layers. Among SiC polytypes, 3C-SiC, 4H-SiC, and 6H-SiC are the most widely used for electronic applications. Each polytype differs from the stacking sequence of the Si-C bilayers, which occurs in three

different provisions, commonly indicated with the notation ABC. The simplest hexagonal structure, called 2H-SiC, has the sequence ABA. The two hexagonal polytypes, 6*H*-SiC and 4*H*-SiC, take on the sequences ABCACB ABCACB, and ABCB ABCB, respectively.

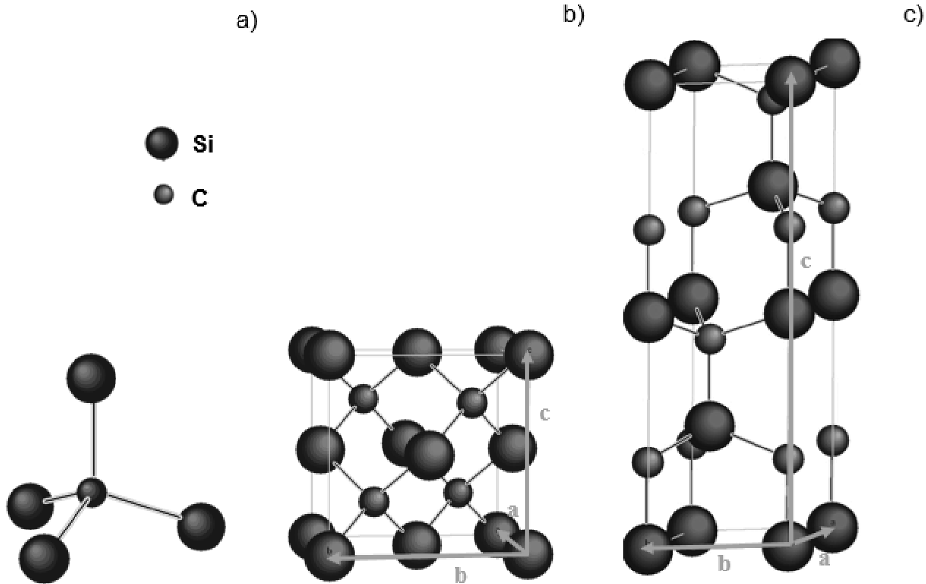

Fig. 1.1. SiC basic tetrahedral structural unit (a), cubic unit cell of the polytype 3C-SiC (b)and hexagonal unit cell of the polytype 4H-SiC (c).

The hexagonal crystal can have two different orientation, i.e., Si-face and C-face, depending if the material is grown with Si or C on top and corresponding to the (0001) and ($000\bar{1}$) crystalline faces. The cubic polytype, 3*C*-SiC, has the stacking sequence ABCABC. The different stacking sequences of 3C-SiC and 4H-SiC are schematically shown in Fig. 1.2. In the SiC crystal, a single Si-C bilayer can be viewed as a planar sheet of silicon atoms coupled with a planar sheet of carbon atoms. Hence, the number identifying each polytype refers to the number of Si-C bilayers before the sequence repeats itself [3].

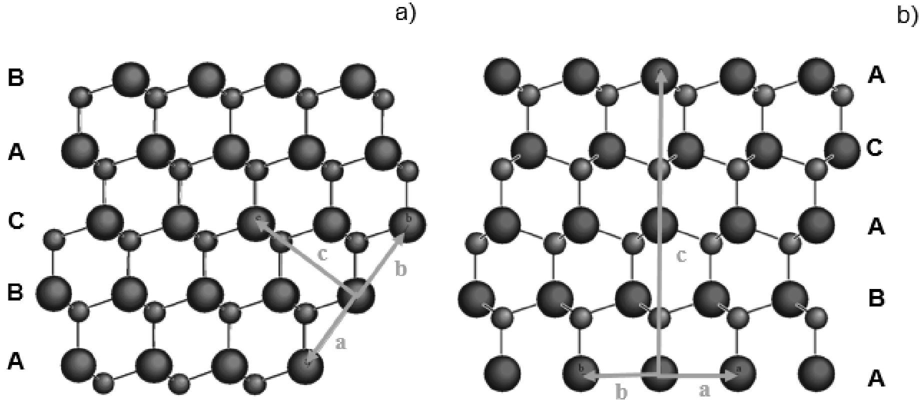

Fig. 1.2. Schematic of the different stacking sequences in 3C-SiC (a), and 4H-SiC (b) polytypes.

The polytypes have different geometrical characteristics. For a generic hexagonal NX-SiC polytype the lattice is characterized by the equation:

$$\frac{c}{Na} = \sqrt{\frac{2}{3}} \approx 0.8165 \qquad (1)$$

where *c* is the length of the spatial period, *N* is the integer number indicating the stack periodicity, *c/N* is the height of the tetrahedron, and *a* is the distance between the atoms in the Si-Si or C-C atoms. In agreement with the Fig 1.2, in 4H-SiC a=3.073 A and c=10.053 A, while 3C-SiC has a cubic unit cell with a=c=4.36 A [4].
The parameter that characterizes SiC polytypes is the *hexagonality* γ, which may vary from unity (pure hexagonal 2H-SiC) to zero (pure cubic 3C-SiC). The hexagonality is defined as the ratio between the number of atoms in hexagonal positions (N_H) and the total number of atoms in the unit cell (N_H+N_C):

$$\gamma = \frac{N_H}{N_H+N_C} \qquad (2)$$

The energy gap of the polytypes is related to the hexagonality, as will be mentioned in Section 1.1.4.

1.1.2 GaN crystalline structure

Gallium nitride (GaN) is a III-nitride binary compound semiconductor, whose thermodynamically stable phase at room temperature and atmospheric pressure is the wurtzite structure. The hexagonal unit cell of wurtzite (Fig.1.3) contains six atoms and each atom is tetrahedrally bonded to four atoms of the other type, with two lattice constants, a=3.18 A and c=5.18 A. Ga and N atoms are arranged in two interpenetrating hexagonal close packed lattices, each with one type of atom, shifted 3/8 c each other [5].

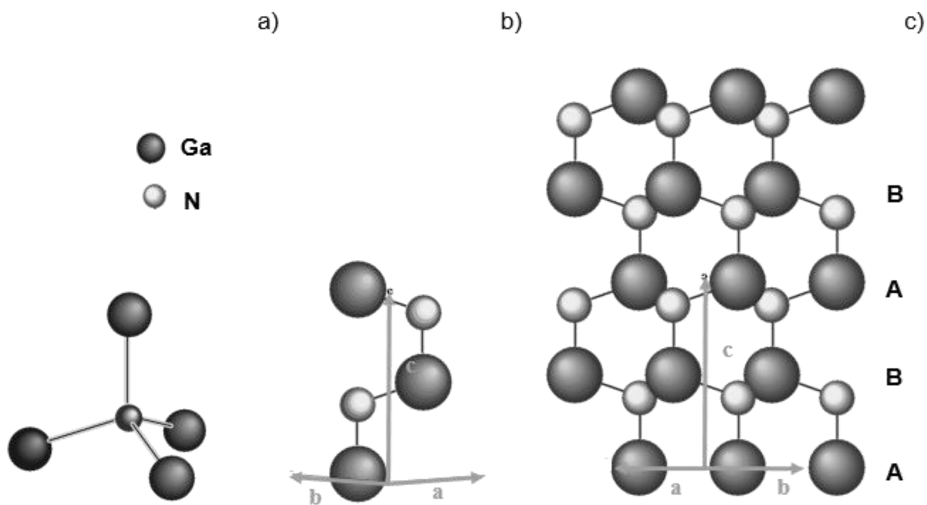

Fig. 1.3. A schematic of basic tetrahedral structural unit (a), unit cell cubic unit cell (b) and stacking sequences (c) of GaN crystal.

Ga and N atoms show a large difference in electronegativity, thus leading to a strong interaction between the covalent bonds. The wurtzite structure does not show inversion symmetry on the [0001] direction (*c axis*). Then, similarly to 4H-SiC and 6H-SiC, also the hexagonal GaN crystal can have two different orientations, i.e., Ga-face and N-face, if the material is grown with Ga or N on top and corresponding to the (0001) and ($000\bar{1}$) crystalline faces, respectively (Fig. 1.4).
Because of the electronegativity of N atoms, the Coulomb potential induces a iconicity, which is responsible for the formation of a "*spontaneous polarization*" P_{SP} along the [0001] direction, as schematically shown in

Fig. 1.4. The spontaneous polarization exists without any stress or strain in the crystal.

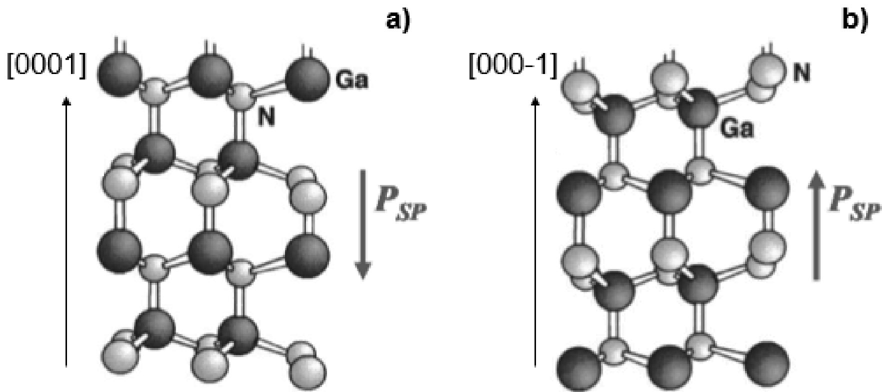

Fig. 1.4. Schematic of Ga-face (a) and N-face (b) GaN crystal. The orientation of the spontaneous polarization vector is also indicated.

Besides the spontaneous polarization, GaN-based materials exhibit piezoelectric properties. The important implications of the a piezoelectric contribution to the polarization in GaN-based materials will be discussed in Section 1.1.5.

1.1.3 Substrates for the growth

WBG semiconductors SiC and GaN are not always available as bulk crystals of large dimensions. In fact, while 4H-SiC bulk substrates (up to 150mm in diameter) are available and used for the growth of homoepitaxial layers, in the case of 3C-SiC and GaN the lack of good quality seed crystals makes the heteroepitaxial growth on a foreign substrate the preferred way to obtain the desired layers for the fabrication of electronics devices.
In general, a substrate is “good” if the lattice parameters and thermal expansion coefficients are very similar to those of the film to grow on it. In fact, the adjustment of the lattice parameters occurring during the heteroepitaxial growth generates strain and extended defects (like dislocations, stacking faults, etc.) in the grown layer.
3C-SiC layers are usually grown on Si substrates, in order to have the possibility of large area wafers at low cost. Unfortunately, due to the large lattice mismatch (20%) between Si (5.43 Å) and 3C-SiC (4.53 Å) a high

density of defects is generated in the interface, then, 3C-SiC heteroepitaxy on Si is an ongoing challenge.
The 3C-SiC material used in this thesis has been heteroepitaxially grown on Si(100) substrates. The 3C-SiC films are characterized by a high density of defects, such as anti-phase boundaries, microtwins and stacking faults and also voids that extend through Si under the interface. Even if many progresses have been made in material growth to improve the quality of 3C-SiC layers [6], the high density of material defects is still a major limitation for the practical application of this polytype for power devices. As an example, the 3C-SiC surface is usually characterized by large steps or islands, which have a strong impact on the electrical behaviour of the metal/semiconductor contacts, thus leading to a negative performance of the final device.
On the other hand, GaN material is typically grown on a large variety of substrates, because of the difficultly to synthetize good-quality large-area GaN bulk crystals. The most popular substrates for GaN growth are sapphire (Al_2O_3), silicon (Si) and silicon carbide (SiC). GaN shows large lattice (+16%) and thermal expansion coefficient mismatch (−34%) with respect to Al_2O_3 substrate, leading to a high defect density of the grown GaN epilayers. The 6H-SiC or 4H-SiC exhibit a favourable lattice mismatch (only 3.5%), and the grown material exhibits dislocation density in the range10^7–10^8 cm^{-2}.
The GaN-based layers used in this thesis were commercial materials grown on 150mm Si(111) wafer. The dislocation density in this material is of the order of 10^9 cm^{-2}, because of the large lattice mismatch (−17%) between GaN(0001) with respect to Si(111). However, Si is a cheap material in comparison with sapphire and SiC. Moreover, using Si as substrate for GaN growth opens interesting perspective to fabricate GaN power devices using the existing Si CMOS lines. For that reason, GaN on Si is receiving a great attention in the last decade by the power devices community [7].

1.1.4 Electronic properties

SiC and GaN exhibit outstanding electronic properties, which can have important implications in the operation of power devices. Table 1 reports some fundamental characteristics of the two SiC polytypes (3C-SiC and 4H-SiC) used in this thesis and GaN. For the sake of comparison, the properties of Si are also given [8,9]. The radar plot shown in Fig. 1.5 graphically summarizes the potential advantages of SiC and GaN with respect to Si.

	Si	**3C-SiC**	**4H-SiC**	**GaN**
E_G **(eV)**	1.12	2.35	3.28	3.39
E_C **(MV/cm)**	0.3	2.0	3.0	3-3.75
n_i **(cm^{-3})**	1×10^{10}	1.5×10^{-1}	5×10^{-9}	$\sim10^{-10}$
v_{sat} **($\times10^7$cm/s)**	1.0	2.0	2.0	3
μ **(cm^2/V·s)**	1350	900	800	1100-1300
k **(W/cm·K)**	1.5	3.2	3.7	1.3-2.1

Tab. 1.1. Properties of common 3C-SiC, 4H-SiC and GaN, compared to those of Si. The data are taken from refs. [10,11,12,13,14,15,16,17].

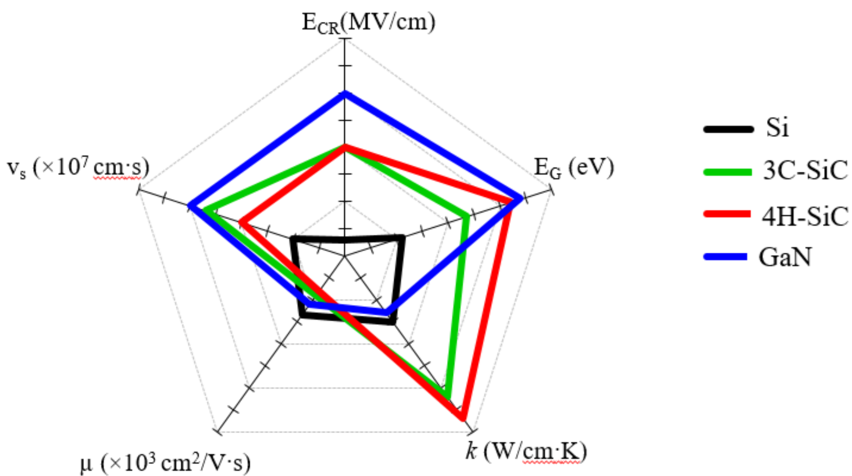

Fig. 1.5. Graphical comparison between the properties of Si, SiC and GaN.

As can be seen in Tab. 1.1, thanks to their large bandgap E_G, which is about 3 times larger than that of Si, SiC and GaN exhibit high values of the critical electric field, E_C (i.e., in the order of 2-4 MV/cm). In fact, the large bandgap implies a high impact ionization energy, thus resulting into high values of maximum electric field that the material can withstand before suffering physical breakdown. Interestingly, since in the case of SiC the band structure depends on the polytype, E_G follows a quasi-linear relation with the hexagonality γ [18], in particular it varies from 2.39 eV for the cubic (γ=0) C-SiC to 3.33 eV for the hexagonal (γ=1) 2H-SiC. The high critical field E_C gives the possibility to withstand the application of high bias values, thus making the materials suitable for high-voltage devices fabrication. Moreover, considering a targeted breakdown voltage, SiC and GaN devices can be fabricated using thinner active drift layers compared to Si, thus leading to a reduction of the electrical resistance.
Another important implication of the large band gap is the low intrinsic electron concentration n_i. Considering the parabolic approximation for conduction and valence bands [19], the intrinsic carrier concentration can be expressed as a function of the gap E_G and the temperature T:

$$n_i^2 = N_C(T)N_V(T)exp\left(-\frac{E_G(T)}{k_BT}\right) \quad (3)$$

where k_B is Boltzmann constant and $N_C(T)$ and $N_V(T)$ are the effective density of states in the conduction and valence bands, respectively. Then, a larger band gap leads to lower values of n_i, which is a very important aspect to operate at high temperatures. Fig. 1.6 shows the comparison of the ideal intrinsic concentration n_i as a function of the inverse of the temperature (1000/T) for SiC, GaN and Si, calculated using eq (3). As can be seen, at room temperature the values of n_i in SiC and GaN are about 18 orders of magnitude lower than in Si at room temperature.
Another very important parameter is the saturated drift velocity v_S, which determines the limit of response speed and operation frequency of a device.

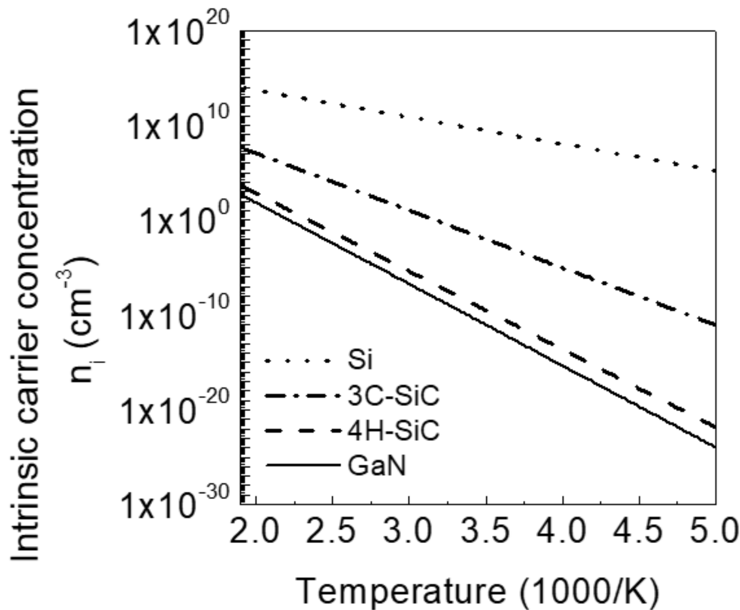

Fig. 1.6. Calculated intrinsic carrier concentration n_i as a function of the inverse of the temperature 1000/T for Si, 3C-SiC, 4H-SiC and GaN.

In a semiconductor, the carriers subjected to an electric field are accelerated until the saturation drift velocity is reached. Then, an additional increase of the electric field does not result in a further increase of the carriers' velocity (Fig. 1.7). It is worth noting that v_S in SiC and GaN is about twice that of Si, thus enabling to obtain high frequency operation.

The carrier mobility is also an important property for high current and high frequency devices. As an example, in GaN materials, the possibility to fabricate AlGaN/GaN heterostructures allows to reach carrier mobility up to 2000 $cm^2/V \cdot s$, owing to the presence of the two-dimensional electron gas (2DEG) formed at the AlGaN/GaN interface. The formation of 2DEG will be described later in Section 1.1.5.

Finally, the capability of heat dissipation in WBG materials is important in power devices. In this context, SiC has a thermal conductivity comparable to that of copper, which enables to operate at extremely high power levels and to dissipate large amounts of heat even without the use cumbersome cooling systems.

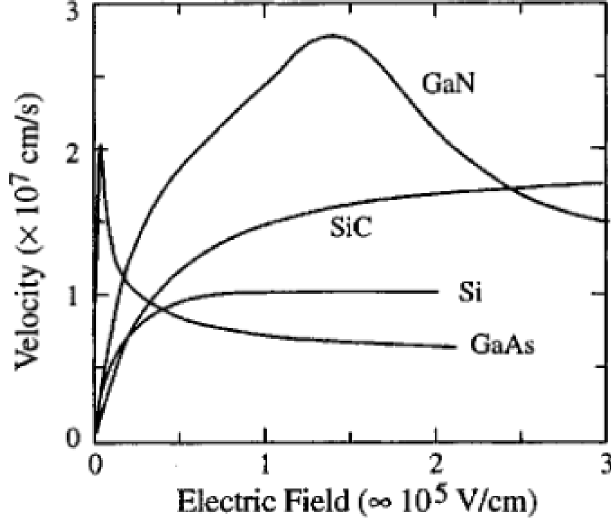

Fig. 1.7. Calculated saturation electron velocity v_S as a function of the electric field in different bulk semiconductors (SiC, GaN, GaAs and Si). The figure is taken from ref. [20].

1.1.5 AlGaN/GaN heterostructures

One of the most interesting characteristics of GaN is the possibility to grow heterostructures based on $Al_xGa_{1-x}N$ alloys. In an $Al_xGa_{1-x}N$ alloy the lattice constant a_{AlGaN} and the energy gap $E_{G\text{-}AlGaN}$ can be tailored by varying the Al concentration x, according to the following Equations:

$$a_{AlGaN}(x) = xa_{AlN} + (1-x)a_{GaN} \tag{4}$$

$$E_{G-AlGaN}(x) = xE_{G-AlN}(x) + (1-x)E_{G-GaN} - x(1-x) \tag{5}$$

Fig (1.8) plots a_{AlGaN} and $E_{G\text{-}AlGaN}$ as a function of x, calculated in agreement with the Eqs (4) and (5).

When a thin layer of semiconductor is epitaxially grown on another with a different lattice constant (e.g., AlGaN on GaN), it tends to assume the lattice constant of the layer. Hence, a deformation (strain) of the crystal will occur, as the crystal tends to be compressed or expanded to compensate the lattice mismatch. Above a critical thickness, the lattice mismatch does not

cause any deformation, but gives rise to the formation of extended crystal defects, like dislocations or cracks.

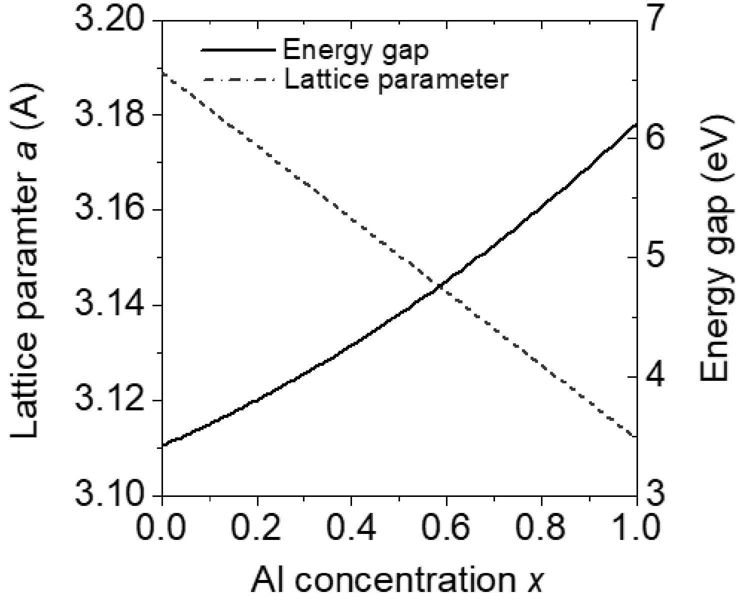

Fig. 1.8. Energy $E_{G\text{-}AlGaN}$ and lattice parameter a_{AlGaN} as a function of the Al concentration x for an $Al_xGa_{1-x}N$ alloy.

If the lattice constant of the deformed upper layer is smaller than that of the underlying layer, the system is in traction (tensile strain). Conversely, if the lattice constant of the upper layer is larger than that of the underlying layer, the deformed layer is in compression (compressive strain) [21]. Hence, besides the "spontaneous polarization" P_{SP} due to the dipole structure of GaN, the piezoelectric behaviour of the material due to a strain leads to an additional polarization called "*piezoelectric polarization*" P_{PE} (Fig. 1.9). The total polarization P_{Tot} will be:

$$P_{Tot} = P_{SP} + P_{PE} \tag{6}$$

The piezoelectric polarization P_{PE} is related to the piezoelectric coefficients e_{33} and e_{31}:

$$P_{PE} = e_{33} \cdot \varepsilon_z + e_{31} \cdot (\varepsilon_x + \varepsilon_y) \tag{7}$$

where $\varepsilon_z=(c-c_0)/c_0$ is the strain along the c-axis, $\varepsilon_x=\varepsilon_x=(a-a_0)/a_0$ are the in-plane strains assumed to be isotropic, and a_0 and c_0 are the equilibrium lattice constants. The lattice constant *a* and *c* follows the equation:

$$\frac{c-c_0}{c_0} = -2\frac{c_{13}}{c_{33}} \cdot \frac{a-a_0}{a_0} \quad (8)$$

where C_{13} and C_{33} are the elastic constants. Then, P_{PE} can be written by taking into account the direction of the c-axis:

$$P_{PE} = 2\frac{a-a_0}{a_0}\left(e_{31} - e_{33}\frac{c_{13}}{c_{33}}\right) \quad (9)$$

The term in brackets is always negative and it does not depend on the composition of the AlGaN layer. Then, P_{PE} will assume negative values for tensile strain ($a > a_0$) and positive for compressive strain ($a < a_0$). Fig. (1.10) shows the direction of P_{SP} and P_{PE}. In the case of Ga-face heterostructures the P_{SP} vector of GaN points towards the substrate (negative), so the alignment between P_{SP} and P_{PE} is parallel in case of tensile strain and antiparallel in case of compressive strain. In the case of N-face heterostructures, P_{SP} and P_{PE} have opposite signs, the P_{SP} vector points in the reverse direction, away from the substrate [22].

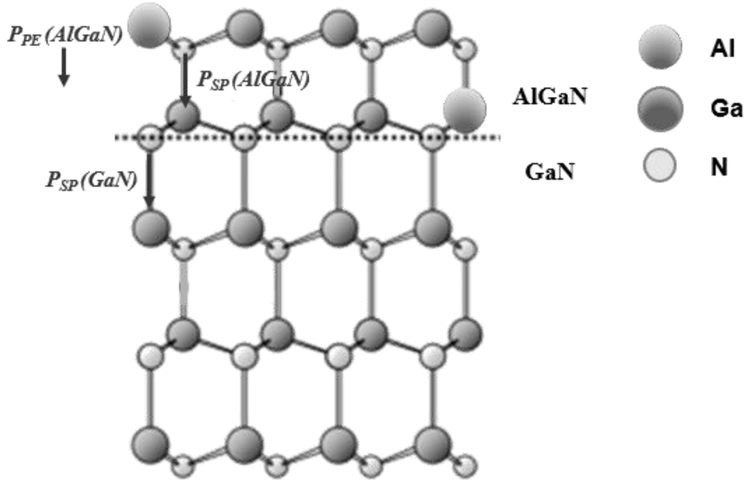

Fig. 1.9. Schematic of the AlGaN/GaN heterostructures.

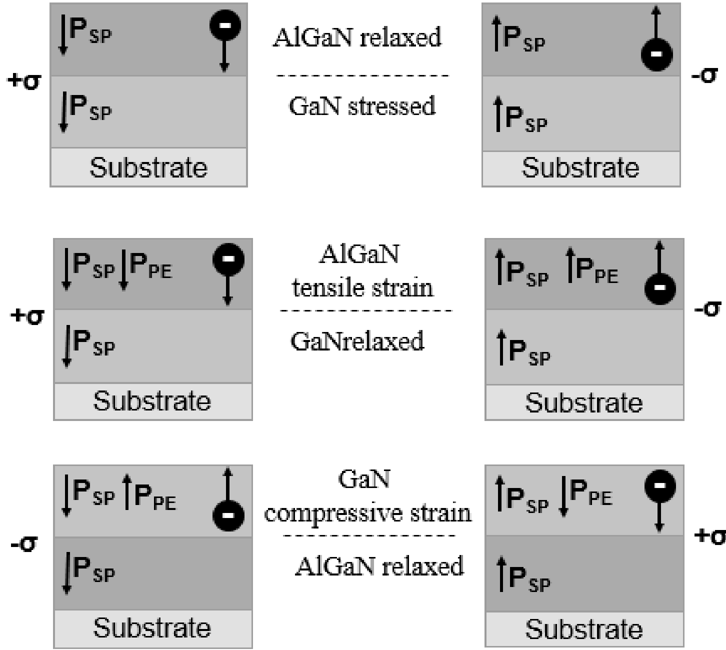

Fig. 1.10. Spontaneous and piezoelectric polarization vectors in Ga-face and N-face strained and relaxed AlGaN/GaN heterostructure. Figure adapted from [22].

The gradient of polarization in space leads to a polarization induced charge density, $\rho_P = \nabla P$.Then, in presence of a top/bottom interface (like in an AlGaN/GaN interface) the total polarization creates a polarization sheet charge density σ:

$$\sigma = \left[P_{(top)} - P_{(bottom)}\right] = [P_{SP} + P_{PE}]^{AlGaN} + [P_{SP} + P_{PE}]^{GaN} = \left[P_{SP}(x) + 2\frac{a(0)-a(x)}{a(x)}\left(e_{31}(x) - e_{33}(x)\frac{c_{13}(x)}{c_{33}(x)}\right)\right] - [P_{SP}(0)] \qquad (10)$$

where x is the Al mole fraction in the AlGaN layer.

In Ga-face structures, the total polarization of AlGaN layer is larger than of GaN layer because piezoelectric constants and spontaneous polarization increase moving from GaN to AlN. Then, a positive polarization charge is present at lower AlGaN/GaN interface that will be compensated by electrons leading to the formation of a *two dimensional electron gas* (2DEG) in the triangular quantum well at the AlGaN/GaN interface, whose ground sub-band level lies below the Fermi level E_F (Fig. 1.11). In N-faced structures a negative polarization charge will be compensated by holes that will accumulate at the interface.

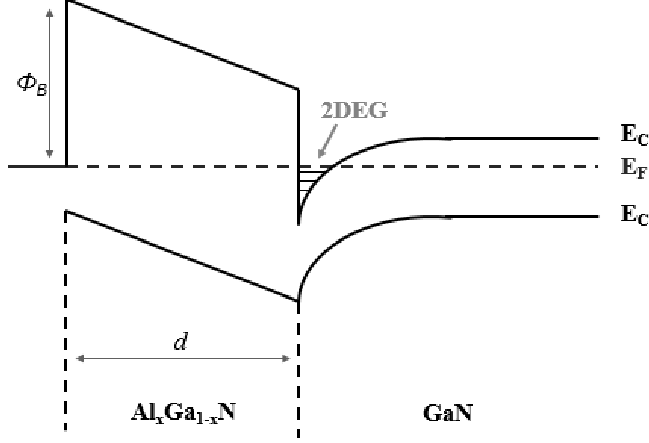

Fig. 1.11. Energy band diagram of a Ga-face AlGaN/GaN heterostructure, showing the formation of the two dimensional electron gas (2DEG) at the interface.

In the specific case of AlGaN/GaN systems, Ambacher et al. [22] proposed an analytical model to describe the properties of such heterostructures and of the 2DEG.
Accordingly, the sheet charge density n_s at the AlGaN/GaN interface can be expressed as:

$$n_s = \frac{\sigma_{int}}{q} - \left[\frac{\varepsilon_0 \varepsilon_{AlGaN}(x)}{d_{AlGaN} q^2}\right] \cdot \left[q\Phi_B(x) + \mathrm{E}_{F_0}(x) - \Delta E_C(x)\right] \quad (11)$$

where σ_{int} is the polarization charge density at the AlGaN/GaN heterojunction, Φ_B is the Schottky barrier height formed at the metal/AlGaN interface, E_{F0} is the Fermi level at the heterojunction with respect to the GaN conduction band edge, ΔE_C is the conduction band offset at the AlGaN/GaN interface. ε_{AlGaN} , d_{AlGaN} and x are the relative dielectric constant, the thickness and Al mole fraction of the AlGaN layer.
In particular, the model assumes an empirical dependence of the parameters in Eq. (9) (ε_{AlGaN}, Φ_B, E_F) on the Al mole fraction x [23]:

$$\varepsilon_{AlGaN}(x) = -0.5x + 9.5 \quad (12)$$

$$q\Phi_B(x) = 1.3x + 0.84\ eV \quad (13)$$

$$E_F(x) = E_0(x) + \frac{\pi\hbar^2}{m^*(x)} n_s(x) \tag{14}$$

where

$$E_0(x) = \left[\frac{9\pi\hbar q^2}{8\varepsilon_0 \sqrt{8m^*_{AlGaN}(x)}} \frac{n_s(x)}{\varepsilon_{AlGaN}(x)} \right]^{2/3} \tag{15}$$

and

$$m^*_{AlGaN}(x) \approx 0.22 m_e \tag{16}$$

As can be seen from these equations, the 2DEG density decreases by decreasing the Al concentration and/or by decreasing the AlGaN barrier layer thickness (see Fig. 1.12). Moreover, the sheet carrier concentration of the 2DEG decreases as the AlGaN thickness decreases down to a critical value d_{CR}. For an AlGaN layer thinner than d_{CR}, the formation of the 2DEG does not occur. The advantage of the generation of 2DEG in AlGaN/GaN consists of very high values of sheet carrier density (~ 10^{13} cm^{-2}) and mobility (1000–2000 cm^2 V^{-1} s^{-1}). The typical values of sheet charge density in 2DEG is about 4-5 times higher than in AlGaAs/GaAs heterojuntions [24].

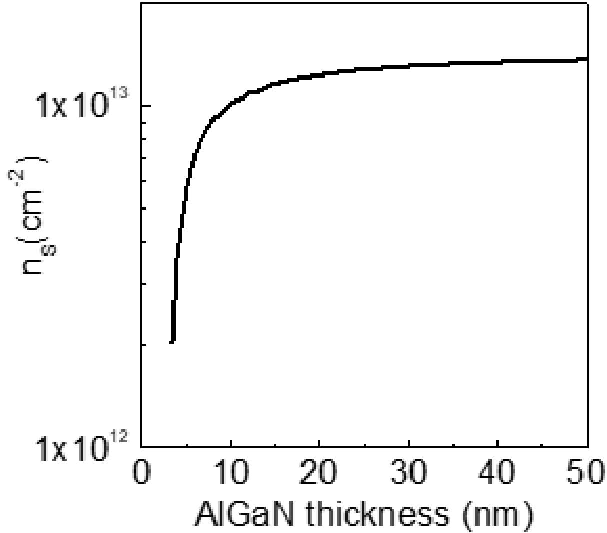

Fig. 1.12. Sheet carrier concentration of the 2DEG as a function of the AlGaN thickness layer, for an aluminium concentration of 26%.

AlGaN/GaN heterostructures can be used for the fabrication of peculiar devices named High Electron Mobility Transistors (HEMTs). A schematic of this device is reported in Fig.1.13 (a), together with the typical output characteristics of the transistor (Fig.1.13 (b)).

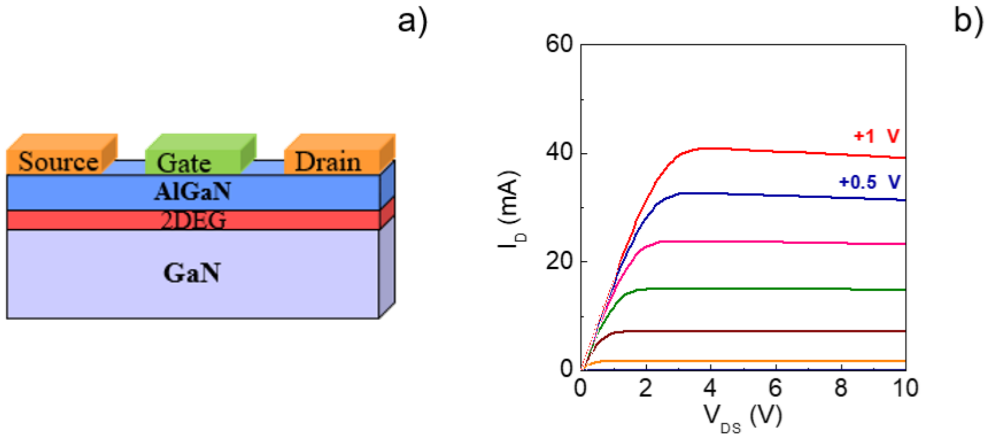

Fig. 1.13. Schematics of an AlGaN/GaN HEMT (a) with the typical output characteristics I_{DS}-V_{DS} (b).

These devices take advantage of the current flowing in the 2DEG channel, through the application of a bias between two source and drain Ohmic electrodes. The current in the channel is modulated by the application of a negative bias to a Schottky gate contact. In Fig. 1.13 (b) the typical output characteristics I_{DS}-V_{DS} of a HEMT are schematically reported as a function of the gate bias Vg. By applying a positive potential difference between source and drain (V_{DS}), the current will start to flow in the 2DEG. Then, on increasing V_{DS} the current increases with a linear trend up to a certain value, after that it starts to saturate. In Fig. 1.14 a schematic band diagram of an AlGaN/GaN HEMT structure is reported, illustrating how the different gate bias influences the 2DEG. At V_g =0 V, HEMTs devices are in the on-state (normally-on device), since there are occupied levels below the Fermi level in the sub-bands of the quantum well (the 2DEG). On the other hand, by decreasing the gate bias V_g to negative values ($V_g < 0$ V) the Fermi level shifts downwards, thus leading to a gradual depletion of the 2DEG, until the position of the Fermi level lies below the conduction band of AlGaN. Below a certain gate bias, called threshold voltage V_{th}, the 2DEG will be

completely depleted and the device will be in the off-state. Hence, in a standard normally-on AlGaN/GaN HEMT the threshold voltage is negative ($V_{th} < 0$ V).

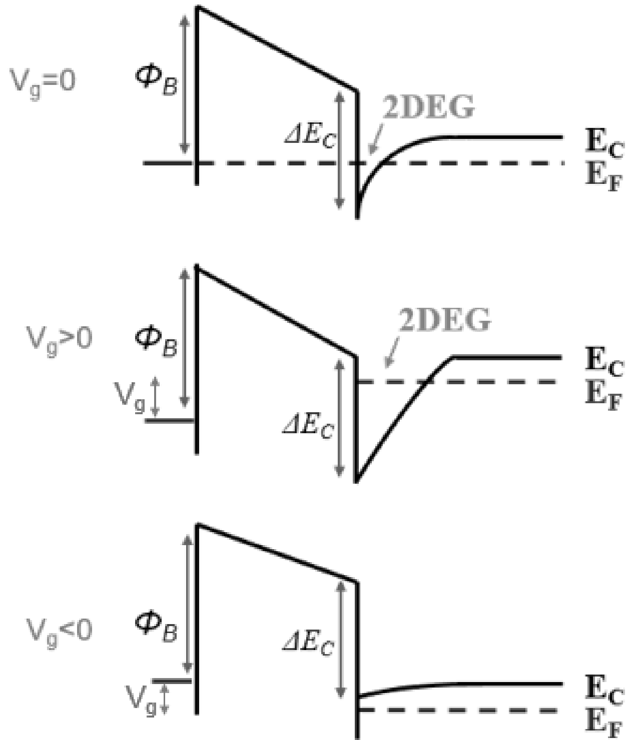

Fig. 1.14. Schematic of the AlGaN/GaN conduction band diagram in a HEMT structure for different values of the gate bias V_g.

In the specific case of AlGaN/GaN heterostructures, the good quality of Ohmic contacts is important in HEMTs devices. In fact, the resistance of source and drain electrodes must be minimized in order to minimize the total transistor resistance and, hence, the power consumption of devices.

1.2 *Advantages of SiC and GaN for power electronics applications*

Silicon has been the material of choice employed for the fabrication of power devices for more than four decades. However, today Si devices have reached their limits, imposed by the material properties. Hence, new semiconductors are needed to meet the requirement of a better energy efficiency and a reduction of the power consumption.

As anticipated in Section 1.1.4, SiC and GaN have outstanding electronic properties, making them the natural candidate to replace Si in the next generation of power electronics devices. As a matter of fact, today a variety of SiC and GaN devices are already available in the market.

In order to understand the advantages of wide band gap semiconductors for power electronics, basic device physics are introduced. Let consider the case of the abrupt parallel-plane (infinite) p^+-n junction, with uniformly doped regions, as schematically represented in Fig 1.15.

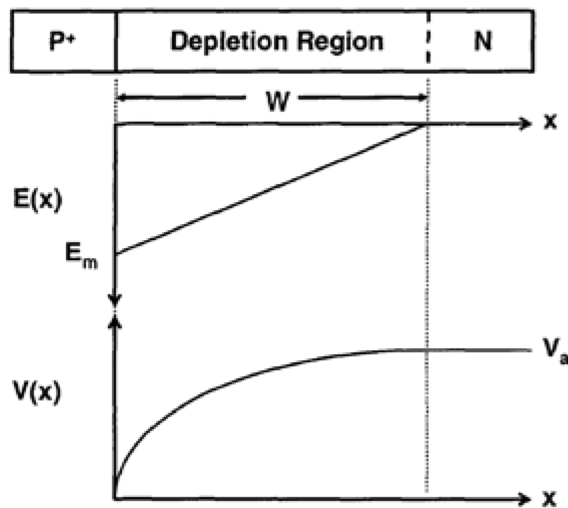

Fig. 1.15. Electric field E(x) and potential distribution V(x) in an abrupt parallel plane p^+n junction (figure from [25]).

The application of a reverse bias to the junction leads to the creation of a depletion region W_D in the n-type layer and the generation of an electric field E. The Poisson equation in this region gives:

$$\frac{d^2V(x)}{dx^2} = -\frac{dE(x)}{dx} = -\frac{Q(x)}{\varepsilon_S} = -\frac{qN_D}{\varepsilon_S} \tag{17}$$

where $Q(x)$ is the charge within the depletion region due to the presence of ionized donors, ε_S is the dielectric constant for the semiconductor, q is the electron charge, and N_D is the donor concentration in the uniformly n-type doped region.

The depth distribution of the electric field $E(x)$ is found by integrating Eq. (15), imposing the boundary condition that $E(x)$ is zero at the edge of the depletion region (at $x = W_D$).

$$E(x) = -\frac{qN_D}{\varepsilon_S}(W_D - x) \tag{18}$$

By integrating the electric field distribution through the depletion region, the potential distribution can be found as:

$$V(x) = \frac{qN_D}{\varepsilon_S}\left(W_D x - \frac{x^2}{2}\right) \tag{19}$$

The thickness of the depletion region (W_D) can be related to the applied reverse bias V_a by:

$$W_D = \sqrt{\frac{2\varepsilon_S V_a}{qN_D}} \tag{20}$$

The maximum electric field (E_m) at the beginning of the junction ($x = 0$) is given by:

$$E_m = \sqrt{\frac{2qN_D V_a}{\varepsilon_S}} \tag{21}$$

By increasing the reverse bias, the breakdown voltage V_B will be reached when the maximum electric field (E_m) reaches the critical electric field (E_C) of the semiconductor.

For an infinite length of the device drift layer (parallel plane approximation), the breakdown voltage of the diode will be given by:

$$V_B = \frac{\varepsilon_S E_C^2}{2qN_D} \tag{22}$$

Eq. 22 is graphically reported in Fig. 1.16 for Si, SiC and GaN, showing that V_B decreases with increasing doping concentration N_D of the device

drift layer. Clearly, WBG semiconductors are able to withstand a higher voltage compared to Si for any given doping concentration.

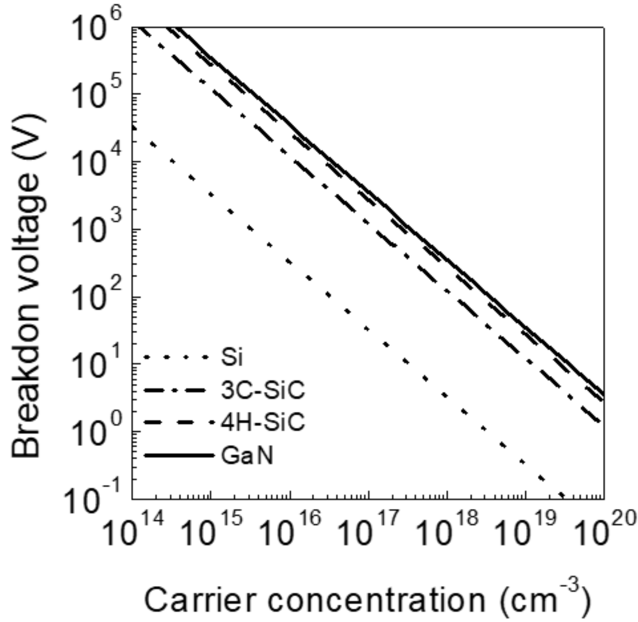

Fig. 1.16. Breakdown voltage V_B as a function of the doping concentration N_D of the drift layer for Si, SiC and GaN.

The onset of the avalanche breakdown is related to a maximum electric field at the junction called the *critical electric field* E_C for breakdown. The thickness of the depletion or drift region is related to the breakdown voltage by the expression

$$W_D = \frac{2V_B}{E_C} \tag{23}$$

The doping concentration in the drift region required to obtain this V_B is given by

$$N_D = \frac{\varepsilon_S E_C^2}{2qV_B} \tag{24}$$

By the combination of the equations reported above, the contribution of the drift region to specific on-resistance of the device can be written as:

$$R_{drift} = \frac{4V_B^2}{\mu \varepsilon_S E_{CR}^3} \quad (25)$$

Generally, in real devices, the total on-resistance R_{ON} is given by several contributions, e.g., the resistance of the contacts R_C, the resistance of the substrate R_{sub} and the resistance of the drift region R_{drift}. The contacts should have a very low specific resistance (typically of 10^{-6}-10^{-5} Ωcm^2). Similarly, the resistive contribution R_{sub} should be negligible for very high doping levels of the substrate. Then, the major contribution to the device on-resistance R_{ON} is that given by the drift layer ($R_{ON} \simeq R_{drift}$). Fig. 1.17 reports the theoretical on-resistance R_{ON} ($R_{ON} \simeq R_{drift}$) as a function of V_B for unipolar Si, SiC and GaN devices (Eq. 24).

The high value of the critical electric field E_C in WBG semiconductors (SiC and GaN) gives the possibility to fabricate devices with a thinner drift region for a targeted operating voltage. In this way, a lower specific on-resistance R_{ON} with respect to the Si devices is obtained. As a consequence of the low R_{ON}, a lower power dissipation of the devices and, then, a better energy efficiency can be obtained. A lower on-resistance translates also in the possibility to reduce the device area for a targeted current level.

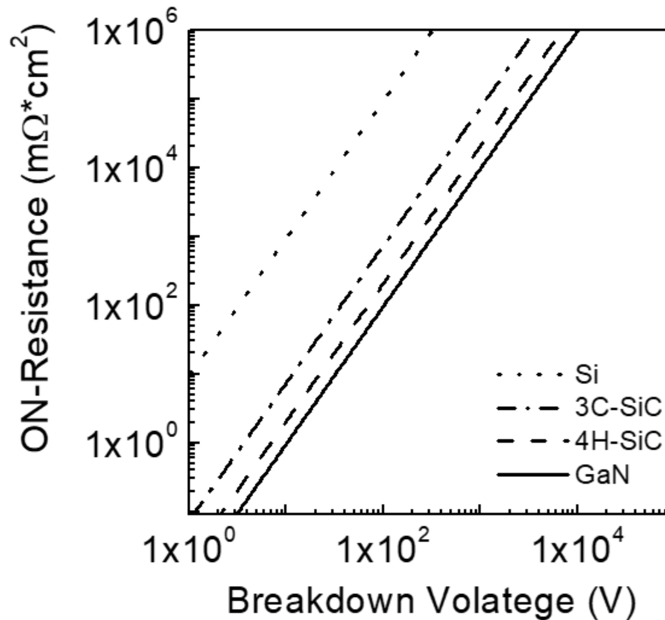

Fig. 1.17. Specific on-resistance R_{ON} as a function of the breakdown voltage V_B for unipolar Si, SiC and GaN devices.

Today, several families of SiC and GaN unipolar devices are available on the market (Schottky diodes, MOSFETs, HEMTs). Although the trade-off R_{ON} vs V_B of these devices is still far from the ideal limits reported in Fig. 1.17, they offer already significant advantages with respect to the Si counterparts in many applications. In fact, WBG based devices show increased power density and a reduction of the power losses in many applications.
Fig. 1.18 shows the possible fields of application of SiC and GaN devices, compared to Silicon application region, in a Power versus Frequency plot. Strategic products and entire market sectors, such as renewable energies, smart grids, downhole drilling, avionics and transportations, envelope tracking, Class-D audio amplifiers, etc., will benefit in the near future from the introduction of WBG devices [26]. These applications may need high-temperature or high-frequency operation, which cannot be achieved using Si devices.
Today, SiC is the most mature among the WBG semiconductors from the material quality, device processing and reliability perspective. On the other hand, GaN can reach higher switching speed than SiC or Si, thanks to its higher electron mobility and saturation velocity. However, due to its lower thermal conductivity, the power density potential is limited. Hence, SiC devices are the best choice for high-voltage applications (> 1200 V), while GaN is used for devices operating at a lower voltage range (200–650 V) but at high frequency.
Generally, the so "called" figures of merit (FOM) are used to compare the potential power electronic performances of different semiconductors. In particular, the Johnson FOM (JFOM) indicates the maximum capability to energize carriers by electric field, and is expressed as (vsat·Ec)/2π. In Si JFOM(Si)= 2×1011 V/s [27]. The values of the JFOM for WBG semiconductors, normalized with respect to Si, are: 2304 for GaN, 576 for 4H-SiC and 324 for 3C-SiC [28,29].

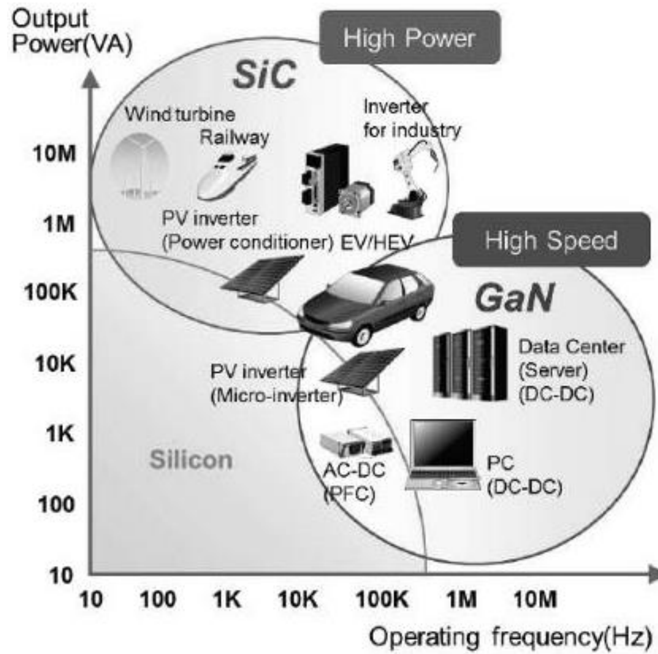

Fig. 1.18. Power versus frequency plot of the possible applications of SiC and GaN devices, compared to Silicon application region. The figure is taken from [30].

1.3 Scientific and technological open issues related to SiC and GaN materials and devices

This thesis has been focused on the study of Ohmic contacts on WBG, SiC and GaN, semiconductors. This is inherently a challenging issue, because the metal/semiconductor barrier height values are typically much higher than in silicon, thus making difficult to achieve low values of the specific contact resistance. The electrical quality of Ohmic contacts can have a significant impact on the total device on-resistance R_{ON} and, hence, on the power consumption. In fact, depending on the device geometry and the targeted breakdown voltage, the contribution of Ohmic contacts to the total device on-resistance can vary from few percent (for good contacts) to some tens of percent (for bad contacts) [31,32]

In spite of the outstanding properties of SiC and GaN, the full exploitation of their huge potential is still limited by several issues, mainly related to

the crystalline quality of the available materials and to the devices processing and reliability. In fact, the electrical properties of metal/semiconductor interfaces on these materials can be influenced by a poor surface morphology and by the presence of defects. In the case of GaN or 3C-SiC, the presence of a large number of defects, typically much higher than in Si, is due to the lattice and thermal expansion coefficient mismatch with the substrate on which they are grown. As introduced in the previous Sections, GaN is an optimum candidate for the fabrication of devices with low on-resistance, high breakdown voltage and high operation switching frequency [33]. However, the lack of free standing GaN substrates of good quality and reasonable cost has restricted the research mostly to GaN layers grown on foreign substrates and, hence, to lateral devices. In the last years, great progresses have been obtained in the epitaxial growth of GaN layers on silicon substrates. Today, large area GaN-on-Si heterostructures are available up to 200 mm in diameter and a variety of HEMTs for high-frequency applications are available on the market.

Owing to the peculiar nature of AlGaN/GaN heterostructures, the formation of Ohmic contacts on these systems is even more difficult than in GaN. In fact, as discussed in Section 1.1.5, the energy gap of an AlGaN barrier layer depends on the Al concentration and is higher than the gap of GaN. Moreover, the properties of the 2DEG depends on both the AlGaN thickness and on the Al concentration. Then, the variation of these parameters can lead to a significant variability of the Ohmic contact properties.

Besides these inherent difficulties in the formation and control of Ohmic contacts on AlGaN/GaN heterostructure, the practical need to have “Au-free” metallizations in the devices is another important issue. On the one hand, this requirement arises from the integration of GaN technology inside Si industry and from the need to reduce the manufacture cost of HEMTs devices. On the other hand, the presence of Au layers leads to some disadvantages, such as high annealing temperatures, high surface roughness and poor edge acuity that can compromise the device reliability [34]. Although several works on Au-free Ohmic contacts on AlGaN/GaN heterostructures have been already reported in literature, the mechanisms responsible for Ohmic contact formation in these systems remain still unclear. Metals with low work function values (Ti, Ta, Al…) should be

suitable for the formation of Ohmic contacts. The combinations of Ti/Al or Ta/Al layers have been proposed to form Ohmic contacts, showing that their electrical properties depend on several factors, e.g., the annealing temperature, annealing time and the metal layer thickness. However, the literature data are often obtained under different annealing conditions and on different materials, thus hindering to draw clear conclusions when comparing different systems. In particular, although Ti and Ta are very similar in terms of work function, a clear physical explanation of the different electrical behavior of these contacts has not been given. Moreover, in literature there is a lack of information on the barrier height properties and on the carrier transport mechanisms at the interfaces between Ti- and Ta- based contacts to AlGaN/GaN heterostructures.

Basing on these consideration, all these aspects have been studied in more detail in this thesis and will be described in Chapter 4.

4H-SiC shows excellent properties that allow to fabricate devices operating at high power, high frequency and high temperature, thus overcoming the limits of Si-based devices. However, also in this case the formation of Ohmic contacts is not an easy task, in particular on p-type doped 4H-SiC material. The main problem is the difficulty to find metals forming low Schottky barrier height. Moreover, the high ionization energy of the p-type dopant (Al) leads to a low holes concentration, thus leading to high specific contact resistance values [35]. Ion-implantation is used to achieve selective doping in 4H-SiC. The electrical properties of implanted 4H-SiC layers strongly depends on the post-implantation annealing conditions and have a strong influence on the final contact properties. Hence, the control of Ohmic contacts requires a deep understanding of the properties of p-type implanted layers upon activation annealing [36,37]. These aspects have been deeply investigated in this thesis and are reported in Chapter 5. This investigation has been preparatory for the study of the electrical properties of Ti/Al/Ni Ohmic contacts fabricated on these layers.

The cubic 3C-SiC can give some advantages with respect to the hexagonal 4H-SiC. In fact, due to the narrower band gap (~2.2eV) of this polytype [9], the SiO_2/3C-SiC interface is expected to have a lower density of interface states near the conduction band edge with respect to the SiO_2/4H-SiC system [38,39]. Consequently, a high inversion channel mobility can be achieved in metal-oxide-semiconductor field effect transistors

(MOSFETs) [40,41].Moreover, 3C-SiC is the only polytype that can be hetero-epitaxially grown on large diameter silicon (Si) substrates. For that reason, this polytype has been considered for many years a very promising solution for the fabrication of power devices on a large scale and at a low cost. In spite of these potential advantages, the application of 3C-SiC in power device technology has been always limited by the quality of the available material, that is still far from reaching an adequate electronic grade [6]. In fact, the sample morphology together with the surface preparation represent a crucial issue stull under investigation. For example, some external treatments, such as the chemical mechanical polishing (CMP), have been investigated in order to improve the electrical properties of the contacts, but need of a further development. Moderately doped 3C-SiC layers are today object of investigation, due to potential application on 3C-SiC MOSFETs. However, there are few studies on Ohmic contacts formation on both moderately n-type doped 3C-SiC and p-type 3C-SiC . In particular, forming good Ohmic contacts to p-type SiC is difficult, because of the low electrical activation and high ionization energy of the p-type dopant impurities. Hence, the final part of this thesis has been devoted to the study of Ohmic contacts on such materials, in order to fill the lack of literature data. In particular, two kinds of contacts, Ni on n-type 3C-SiC, and Ti/Al/Ni on p-type 3C-SiC, have been investigated to correlate their electrical response to the morphological and structural modification upon annealing treatments. These two kinds of contacts have been also evaluated independently of the 3C-SiC substrate (n-type or p-type) in order to understand the difficulties related to the metal choice for the Ohmic behaviour achievement.

Chapter 2 – Background on metal/semiconductor contacts

This chapter will synthetically provide the basic physical background for the comprehension of metal/semiconductor contacts. In particular, the discussion will be centred around the metal/semiconductor Schottky barrier formation, discussing the classical carrier transport mechanisms at these interfaces, and introducing the concept of specific contact resistance for Ohmic contacts.

2.1 Schottky barrier and current transport mechanisms

Metal/semiconductor contacts are important building blocks of microelectronics and optoelectronics technology, as they connect the devices with the external circuitry. Then, the knowledge of the physical properties and the carrier transport mechanisms at metal/semiconductors interfaces is a fundamental topic, object of investigation by the device community.

Typically, two types of metal/semiconductor contacts can be distinguished. *Schottky contacts* have a rectifying current-voltage behaviour (asymmetric I-V characteristics), due to the presence of a potential barrier to be overcome from the carriers at the interface. *Ohmic contacts*, instead, have linear and symmetric I-V characteristics.

The most important parameter that describes the electrical behaviour of a metal/semiconductor junction is the Schottky barrier height $q\Phi_B$. We recall that the metal work function $q\Phi_M$ is defined as the energy needed to bring an electron from the Fermi level of the metal to the vacuum level. Analogously, the semiconductor electron affinity χ quantifies the energy needed to bring an electron outside the semiconductor, i.e., the potential difference between the bottom of the conduction band and the vacuum level. The energy $q\Phi_S$ is the semiconductor work function, which is defined as the energy difference between the Fermi level in the semiconductor and the vacuum level. Fig.2.1 shows the energy band diagram of a metal and an n-type semiconductor before and after to be placed in contact.

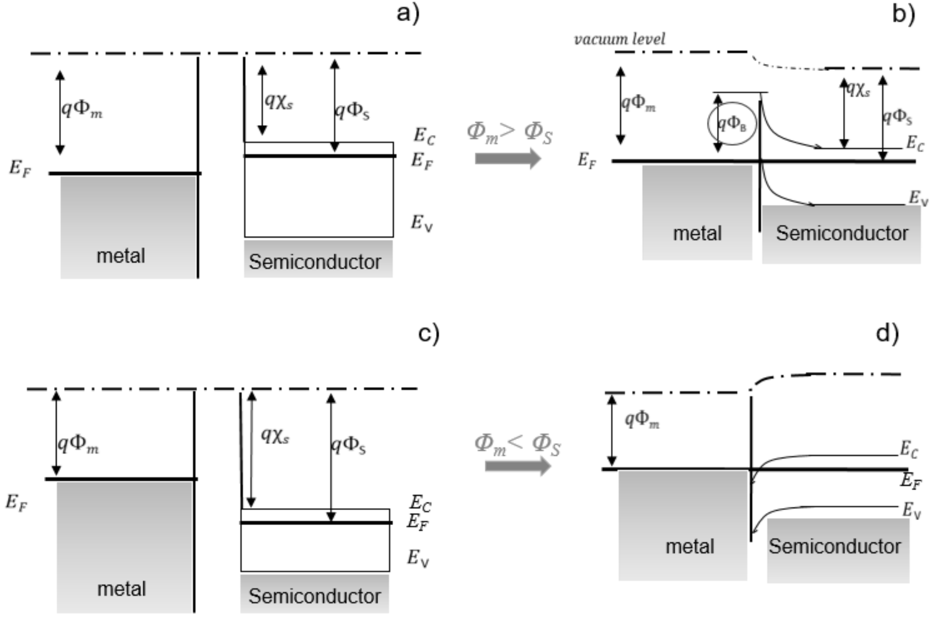

Fig. 2.1. Energy band diagram of a metal/semiconductor system (case on n-type semiconductor) before (a) and after the contact (b) in the configurations $q\Phi_M > q\chi$ and before (c) and after the contact (d) in the configurations $q\Phi_M < q\chi$.

First, let consider the most common case in which $q\Phi_M > q\chi$ (Fig.2.1(a)). Under this condition, when the metal and the semiconductor are in intimate contact, electrons will flow from the semiconductor to the metal, leaving a depletion region W behind. This electrons flux stops when the Fermi level is aligned all over the structure, leading to an upward band bending (Fig.2.1(b)) and the formation of a Schottky contact. The Schottky barrier height $q\Phi_B$ can be seen as the energy needed for electrons in the metal to penetrate the semiconductor, and can be expressed by the well-known Schottky-Mott relation [42]:

$$q\Phi_B = q(\Phi_M - \chi) \tag{26}$$

Similarly, in the case of a Schottky contact on a p-type semiconductor, the Schottky barrier height will be given by:

$$q\Phi_B = E_G - q(\Phi_M - \chi) \tag{27}$$

On the other hand, in the case of $q\Phi_M < q\chi$ (Fig.2.1(c)), the electrons will transfer from the metal to the semiconductor, giving rise to a downward

band bending at the interface (Fig.2.1(d)). In this condition, at the equilibrium there is no barrier for the electrons and an Ohmic contact is formed.

In general, the metal work functions fall in the range of 5-6 eV, while the semiconductors electron affinity values are about 4 eV. Hence, the condition $q\Phi_M > q\chi$ is always satisfied and almost all metals after deposition form Schottky contacts on moderately doped WBG semiconductors. The values of the Schottky barrier height formed on WBG semiconductors are typically higher than in Si, due to the lower electron affinity of these materials.

The doping level of the semiconductor is another important parameter, which has an impact on the current transport processes at the interface. Fig. 2.2 schematically shows a metal/n-type semiconductor junction and the possible classical transport mechanisms for different donor levels N_D of the semiconductor. If the semiconductor is lightly-doped ($N_D < 10^{17}$ cm^{-3}), the depletion region *W* is large enough to be crossed by electrons if they are thermally excited over the barrier. Hence, the current flow will obey the *Thermionic Emission* (TE) mechanism (Fig. 2.2 (a)). If the semiconductor has an intermediate doping ($10^{17} < N_D < 10^{19}$ cm^{-3}), the decrease of *W* enables the electrons to tunnel the barrier at a lower energy. This is an intermediate condition between the thermionic effect and the tunnel effect, called *Thermionic Field Emission* (TFE) (Fig. 2.2 (b)). Finally, for high doping levels ($N_D > 10^{19}$ cm^{-3}), the depletion region *W* becomes very narrow and the electrons can tunnel through the thin barrier according to the *Field Emission* (FE) mechanism (Fig. 2.2 (c)).

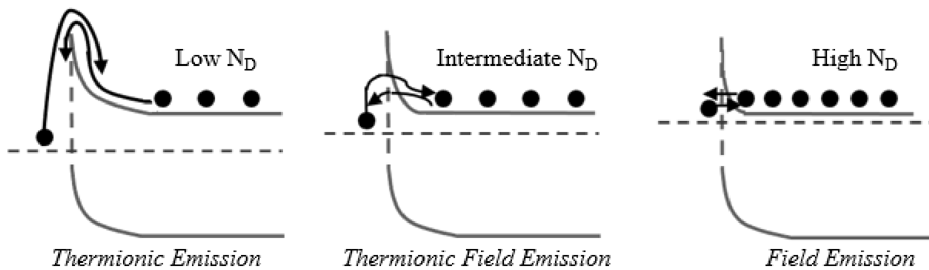

Fig. 2.2. Schematic of the metal/n-type semiconductor band structure for different doping levels. The dominant current transport mechanisms are indicated.

The parameter that rules out the occurrence of a transport mechanism is the characteristic energy E_{00}, defined as:

$$E_{00} = \frac{qh}{4\pi}\sqrt{\frac{N_D}{\varepsilon\varepsilon_0 m^*}} \qquad (28)$$

where m^* is the tunneling effective electron mass and h is Planck's constant. The comparison between E_{00} and the thermal energy kT shows the dominant mechanism: t TE for $kT>>E_{00}$, TFE for $kT \approx E_{00}$ and FE for $kT<<E_{00}$.

As reported above, the condition $q\Phi_M > q\chi$ leads to the Schottky contact formation. Considering a lightly doped semiconductor, the application of a voltage V through a metal/semiconductor junction leads to a current I given by the TE theory:

$$I = AA^*T^2e^{-q\Phi_B/kT}\left(e^{qV/nkT} - 1\right) = I_S\left(e^{qV/nkT} - 1\right) \qquad (29)$$

where I_S is the saturation current, A the contact area, A*=$4\pi qk^2m^*/h^3$ the Richardson' constant, $q\Phi_B$ the effective barrier height, k the Boltzmann' constant, T the temperature and n the ideality factor (that incorporates all those unknown effects that make the device non ideal). The I-V curve of a metal/semiconductor Schottky contact is schematically reported in Fig. 2.3.

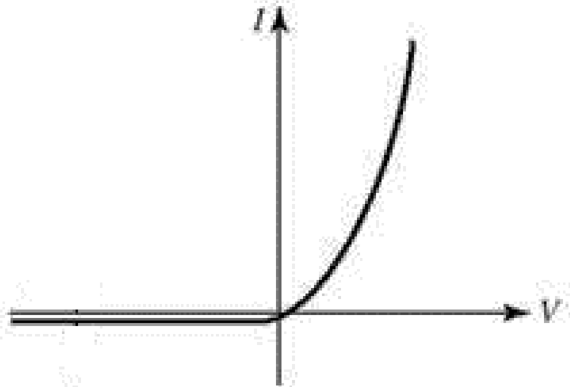

Fig. 2.3. Schematic of the I-V characteristic of a metal/semiconductor Schottky contact.

The barrier height is most commonly extracted from the saturation current I_S, determined by the linear extrapolation at V=0 of the semilog I-V curve

in forward bias. Then, the Schottky barrier height Φ_B can be calculated from the equation

$$\Phi_B = \frac{kT}{q} ln\left(\frac{AA^*T^2}{I_S}\right) \quad (30)$$

Fig. 2.4 shows a typical I-V characteristic of a Schottky contact with the application of the current-voltage method to extract $q\Phi_B$ from the linear fit of the curve reported in a semilogaritmic scale.

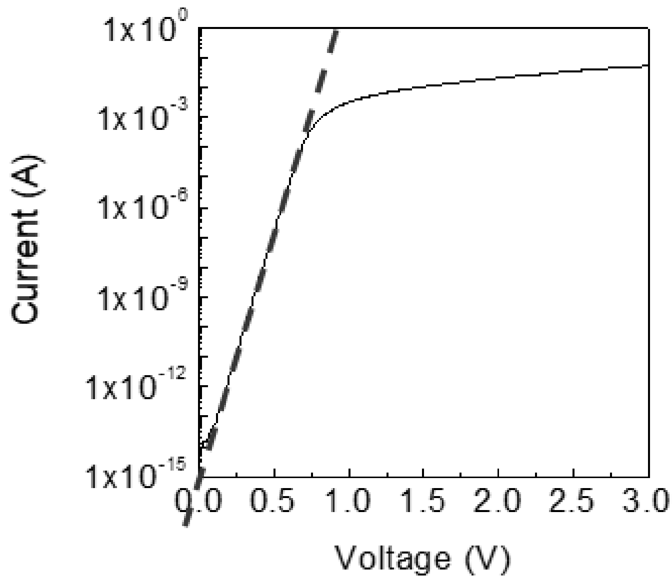

Fig. 2.4. Semilog plot of the I-V characteristic of a Schottky contact in forward bias. The linear fit to extrapolate the Schottky barrier is shown as dashed line.

2.2 Ohmic contacts

As seen before, it is very difficult to find metals with work functions satisfying the condition $q\Phi_M < q\chi$. Then, the formation of Ohmic contacts on WBG semiconductors is obtained using heavily doped materials and/or inducing the formation of intermetallic alloys by thermal annealing. In this case, a narrower depletion region *W* will be formed at the interface, favouring the electrons tunnelling through the interface. In contrast from the rectifying Schottky contact, the Ohmic contact behaves a linear I−V

curve, as schematically shown in Fig. 2.5. An important parameter that describes this behaviour is the contact resistance R_C (Ω). However, since R_C depends on the area of the contact, it is more useful to consider the specific contact resistance ρ_c $(\Omega\cdot cm^2)$, which is a parameter enabling a direct comparison between contacts independently from the geometry.

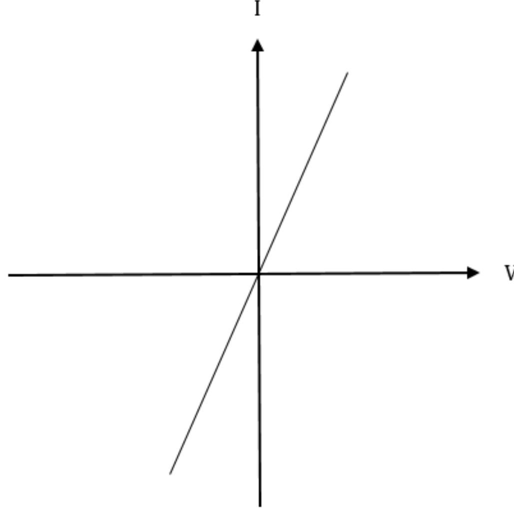

Fig. 2.5. Schematic of the I-V characteristic of a metal/semiconductor Ohmic contact.

The specific contact resistance ρ_c is defined as the derivative at V=0 of the voltage V with respect to the current density J:

$$\rho_C = \left(\frac{\delta V}{\delta J}\right)_{V=0} \tag{31}$$

The analytical expression of ρ_c (Eq. (31)) can be different, depending on the current transport mechanism linked to the semiconductor doping level. In particular, ρ_c will have a different dependence on the barrier height $q\Phi_B$ and on the temperature T.

The expressions of the current density at a metal/semiconductor contact, according to the classical FE, TFE and TE mechanisms, are given by:

$$J_{FE} = \frac{A^* T\pi exp[-q(\Phi_B - V_F)/E_{00}]}{C_1 k\, sin(\pi C_1 kT)}[1 - exp(-C_1 q V_F)] \tag{32}$$

With $C_1 = \frac{1}{2E_{00}} log\left[\frac{4(\Phi_B - V_F)}{-V_n}\right]$ (33)

$$J_{TFE} = \frac{A^*T\sqrt{\pi E_{00} q(\Phi_B - V_n - V_F)}}{k\cosh(E_{00}/kT)} exp\left[\frac{-qV_n}{kT} - \frac{q(\Phi_B - V_F)}{E_0}\right] exp\left(\frac{qV_F}{E_0}\right) \quad (34)$$

with

$$E_0 = E_{00}\coth(E_{00}/kT) \quad (35)$$

$$J_{TE} = A^*T^2 exp\left(-\frac{q\Phi_B}{kT}\right)\left(e^{qV/nkT} - 1\right) \quad (36)$$

Then, by substituting the above expressions of the current density in Eq. (31), enables to find the specific contact resistance ρ_c for the FE, TFE and TE mechanisms:

$$\rho_{C-TE} = \frac{k}{A^*Tq} exp\left(\frac{q\Phi_B}{kT}\right) \propto exp\left(\frac{q\Phi_B}{kT}\right) \quad (37)$$

$$\rho_{C-TFE} = \frac{\mathrm{k}\sqrt{E_{00}}\cosh(E_{00}/kT)\coth(E_{00}/kT)}{A^*Tq\sqrt{\pi q(\Phi_B - V_n)}} exp\left[\frac{q(\Phi_B - V_n)}{E_{00}\coth(E_{00}/kT)} + \frac{qV_n}{kT}\right] \propto exp\left[\frac{q\Phi_B}{E_{00}\coth(E_{00}/kT)}\right] \quad (38)$$

$$\rho_{C-FE} = \frac{k\, sin(\pi C_1 kT)}{A^*Tq\pi}\ exp\left(\frac{q\Phi_B}{E_{00}}\right) \propto exp\left(\frac{q\Phi_B}{E_{00}}\right) \quad (39)$$

Fig. 2.6 shows specific contact resistance as a function of doping density (a) and as a function of the temperature (b) for TE, TFE and FE current transport mechanisms, calculated for different values of Shottky barrier height.

The curves have been calculated for a p-type 4H-SiC, fixing the Richardson's constant of 146 A/cm^2K^2, effective mass of $0.91*m_0$ and the dielectric constant of 9.7. In Fig. 2.6 (b) the value of Schottky barrier height has been fixed at 0.55eV.

The method used to experimentally determine ρ_c is the Transmission Lined Model (TLM), which is described in section 3.2.1.

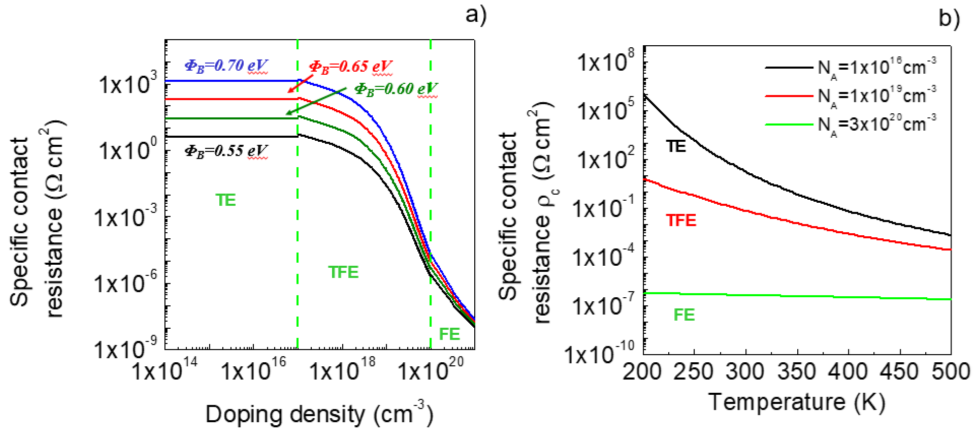

Fig. 2.6. specific contact resistance as a function of doping density (a) and as a function of temperature (b) for TE, TFE and FE current transport mechanisms calculated for a p-type 4H-SiC.

Chapter 3 - Experimental techniques

This chapter aims to give a synthetic description of the main characterization techniques, which were required during this thesis.
Atomic Force Microscopy (AFM) has been used in order to monitor the surface morphology of the WBG materials and of Ohmic contacts formed on them. The local current conduction in these systems was studied by means of conductive atomic force microscopy (C-AFM). Then, the structural analysis of the contacts has been performed by X-Ray Diffraction and Transmission Electron Microscopy, which allowed the identification of the new phase formed after thermal annealing and the quality and composition of the interface region.
The electrical properties of semiconductor layers have been studied by means of Van der Pauw and Hall effect measurements, which can give information on the resistivity ρ ($\Omega\cdot$cm), the carrier concentration (carriers/cm^3), their sign (i.e., holes or electrons) and their mobility μ (cm^2/V$\cdot$s). The electrical characterization of the contacts and devices have been carried out by means of current-voltage (I-V) measurements. To this purpose, specific test patterns have been fabricated to apply the Transmission Line Model. This production has been performed in the clean room of CNR-IMM and was a part of the experimental work. A description of the fabrication flow chart is also reported.

3.1 Morphological, structural and optical characterization.

3.1.1 Atomic Force Microscopy (AFM) and Conductive AFM

Atomic Force Microscopy (AFM) allows studying the morphology of a sample surface with nanoscale resolution. A typical AFM set up is schematically shown in Fig. 3.1(a). It consists of a cantilever probe, a sharp tip mounted on a piezoelectric material, a laser beam that is reflected from the cantilever, providing information on its deflection, and a position sensitive photo detector that collects the reflected laser beam. The AFM is

based on scanning the tip over the sample surface with mechanisms that lead the piezoelectric scanners to maintain the tip at a constant force, or constant height.

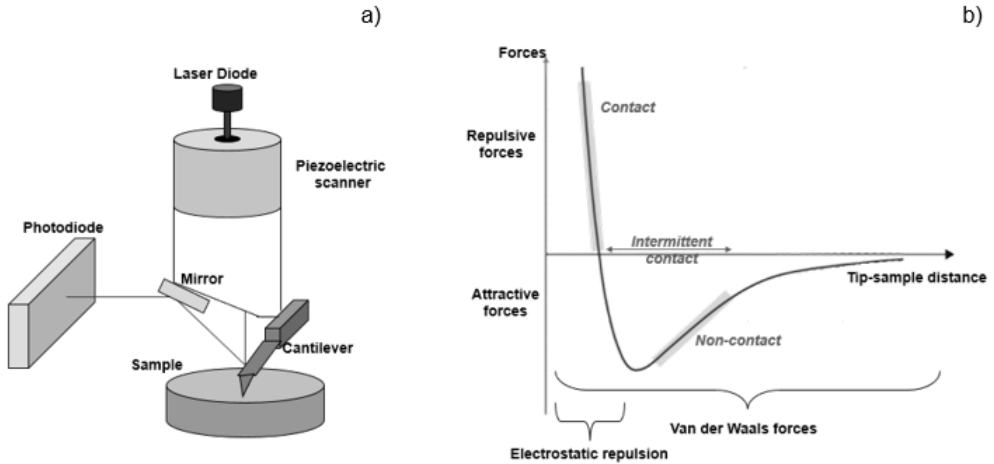

Fig. 3.1. Schematic set up of an atomic force microscope (a) and interaction forces between the tip and the sample surface (b).

The AFM exploits the interaction forces between the tip and the sample surface, which can be either attractive or repulsive. The attractive forces are the Van der Waals interaction, electrostatic force and chemical force. The repulsive forces can be considered as Pauli-exclusion interaction and electron–electron Coulomb interaction and, generally, they act in a short-range and follow an exponential decay or an inverse power law dependence with the distance. The interaction forces between the tip and the sample surface can be schematically represented by the curve shown in Fig. 3.1(b). When the interatomic distance is large, weak attractive forces dominate. As the atoms of the tip and the surface are gradually brought closer to each other, an increase of the attractive forces occurs. When the atoms become very close, the electrostatic repulsion becomes dominant.
Depending on the interaction force regime, AFM can be operated in static or dynamic mode.
The dynamic mode of AFM includes the *tapping* (or intermittent contact) mode, which exploits the cantilever oscillation at/or near its natural resonant frequency. The piezoelectric effect applies a force on the cantilever base leading the tip to vibrate at amplitudes which are typically

of some nm when the tip and the surface are not in contact. The oscillation amplitude is kept constant through a feedback loop. The oscillation frequency (Hz) is given by

$$\omega = \sqrt{\frac{k_{eff}}{m}} \tag{40}$$

where m the effective cantilever mass and k_{eff} is the effective force constant. Then, when the tip is moved toward the surface, it begins to alternately tap the surface and the amplitude of vibration changes according to the surface topography of the sample. When the tip passes over a hillock, its vibration amplitude decreases because there is less vibrating space and when it passes over a depression, its vibration amplitude increases. The oscillation amplitude changes are detected by the optical system and are compared with the set reference value, and generating an error signal in order to adjusts the tip–sample separation to maintain constant amplitude and thereby constant force on the sample. This signal is then used to plot the surface topography of the sample. The absence of repulsive forces permits the imaging of “soft’’ samples to provide analysis without sample degradation.
In the *static* mode, also named *contact* mode, the interaction forces between the tip and the sample surface are mainly repulsive. During the scan the force between the tip and the sample is kept constant, and its value is monitored by measuring the deflection d of the cantilever, according to the Hook’s law:

$$F_H = -k_c d \tag{41}$$

where k_c is the force constant of the cantilever. The tip is initially brought in contact with the sample until the required cantilever deflection is reached. Then the cantilever deflection is recorded by an optical detection system and is compared with a settled value leading to an error signal. This signal is used to actuate the piezoelectric positioning element by applying the required voltage and then the cantilever is raised or lowered in order to restore the desired deflection and thus maintains constant force between the tip and sample.
Besides providing the surface morphology with high spatial resolution, the AFM system can be used to simultaneously probe the electrical properties.

As an example, conductive AFM (C-AFM) analysis, are capable of nanometre resolution current mapping and local current-voltage measurements, by connecting a current amplifier to a conductive AFM tip. C-AFM measurements are typically carried out in contact mode, as a stable contact between the tip and sample are requested for local current measurements. The application of a potential difference between the tip and the sample leads to an electrical field which results in a net current flowing from the tip to the sample or vice versa. The C-AFM collects a current that depends on the effective contact area of the tip (A_{tip}) where the current density J flows:

$$I = J \cdot A_{tip} \quad (42)$$

Besides the effective contact area, the series resistance contributions of tip material and of the substrate also determine the measured current level. However these resistive terms are constant during the surface scanning and their weight is typically negligible, as compared to the contact resistance between the nanoscale tip and the sample.The current is converted by the preamplifier that transforms the signal into digital voltages that can be read by the computer (Fig. 3.2)).

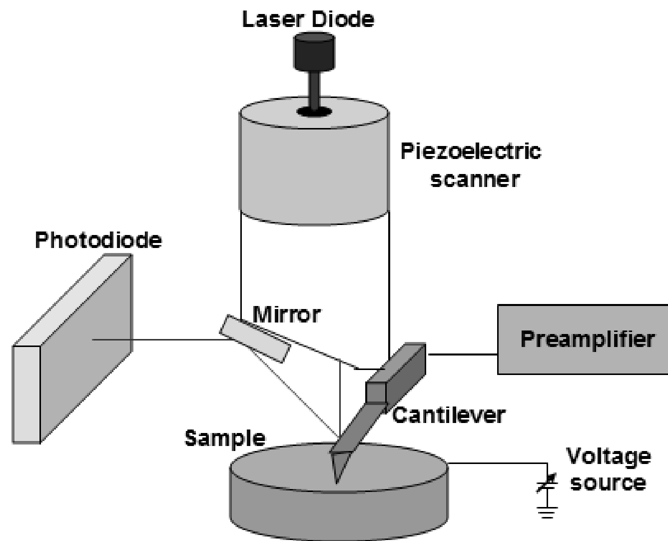

Fig. 3.2. Schematic for a C-AFM instrument.

In this work, AFM and C-AFM measurements have been carried out in order to study the surface of the samples subjected to different external treatments and to find possible correlations between the surface morphological features and the local electrical behavior of the materials. The instrument used was a Veeco Dimension 3100 microscope with Nanoscope V controller.

3.1.2 X-Ray diffraction (XRD)

X-Ray diffraction is a non-destructive technique used for structural characterization of crystalline materials, which enables to obtain information about chemical phase, grain size and strain of a crystal lattice. XRD is based on the scattering of X-rays from the sample excited with ionizing radiation. A beam of electrons accelerated by an electric field towards a metal produces a X-ray beam with the wavelength characteristic of the metal target. If an X-rays beam of wavelength λ collides onto a crystal lattice with an angle θ, some of the X-rays will be scattered by the lattice planes with interplanar distance d will positively interfere by a diffraction phenomenon described from the Bragg's law (Fig. 3.3):

$$n\lambda = 2d\sin(\Theta) \quad (43)$$

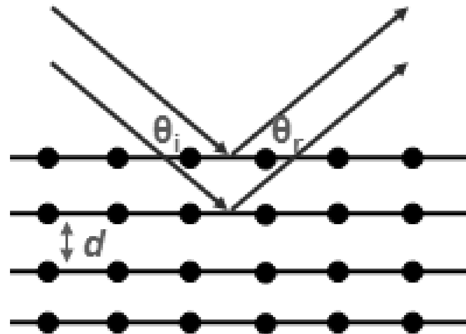

Fig. 3.3. Basic principle of the XRD: representation of the Bragg's law.

The X-ray beam can be considered as electromagnetic waves, which are scattered from electrons of the lattice atoms. Secondary spherical waves are created and they constructively interfere only in some directions where

their path-length difference $2d \sin \theta$ is an integer multiple of the wavelength "λ". X-rays are used to produce the diffraction patterns because their wavelength λ is typically of the same order of magnitude (1–100 angstroms) of the spacing *d* between planes in the crystal. The diffraction effects can be interpreted as a function of the position of atoms in the lattice. The Miller indexes *(hkl)* are associated with a family of parallel planes having interplanar distance $d_{(hkl)}$. Fig. 3.4 shows the typical θ-2θ geometry configuration for XRD analysis: the incident angle θ is defined between the X-ray source and the sample; the diffraction angle 2θ is defined between the incident beam and the detector; the X-ray source is fixed, the sample rotates at θ°/min and the detector rotates at 2θ°/min. Another possible configuration is the so-called θ-θ geometry: in this case, the sample is fixed and both the X-ray source and the detector rotate with a rate of θ°/min.

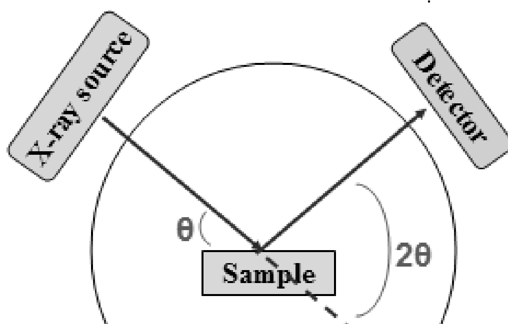

Fig. 3.4. Schematic of θ-2θ geometry configuration for XRD analysis.

In this work, XRD measurements have been carried out in "grazing incidence" mode using a Bruker-AXS D5005 θ- θ diffractometer operating with a Cu Kα radiation at 40 kV and 30 mA. In this configuration, the incident angles for the incoming X-ray is very small (<5°) so that X-rays are focused only in the uppermost part of the sample surface, leading to Bragg reflections only coming from the surface structure. The XRD analysis provided information on the new phases formed after the annealing processes of metal contacts.

3.1.3 Transmission electron microscopy (TEM)

The transmission electron microscopy (TEM) is widely used in material science for structural and chemical analysis. Through TEM analysis it is possible to obtain high-resolution images of the atomic planes of a crystalline structure, diffraction patterns, visualize material defects, etc.. An electron beam is generated with an e-gun by thermionic effect and is accelerated by a potential through the microscope column maintained at a constant pressure (Fig. 3.5).

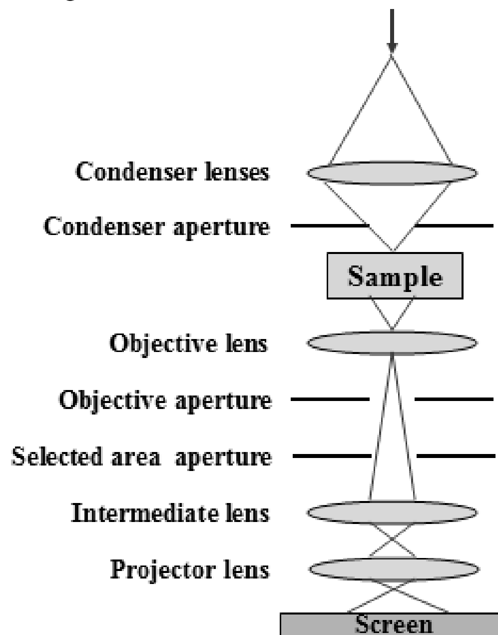

Fig. 3.5. Schematic of the beam pattern in a Transmission Electron Microscope.

The beam is focused on a thin sample (<100nm) through condenser lens that exclude high angle electrons. The electrons of the beam interact with the atoms of the sample and produce diffracted beams that, through a lens placed under the sample, are focused in order to reproduce the image of the investigated area. In particular, the transmitted and forward scattered electrons form a diffraction pattern in the back focal plane and a magnified image in the image plane. Then, the image or the diffraction pattern is magnified through additional lenses and projected onto a fluorescent screen.

The magnification depends on the focal length and the magnitude of the deflection of the electron beam will be proportional to the intensity of the magnetic field. The spatial resolution of TEM suffers from aberrations such as the chromatic one, caused by the loss of energy due to inelastic interactions with the atoms of the sample, and the spherical one, caused by the fact that beams emerging from the sample at large angles are not focused at the same point image. Another kind of aberration, called astigmatism, can be caused by defects in the construction of the lenses leading to deviations of the magnetic field from the axial symmetry.
When the electrons interact with the atoms of the sample, they can be elastically diffused without losing their kinetic energy, or they can inelastically interact with the electronic clouds losing part of their energy. If the sample is thick, all the incident electrons remain inside the sample. As the thickness decreases, after the inelastic interaction the electrons will be focused at different distances. The diffraction image contains a large number of points related to beams diffracted by different reticular planes, which satisfy the Bragg's law (Eq. (43)). All the diffracted beams interfere one to each other to form the sample image that can be enlarged using the transmitted beam (bright field image) or the diffracted beam (dark field image).
A stationary, parallel, coherent electron beam passes through the sample forming a magnified image in the image plane that is projected onto a fluorescent screen. In *scanning transmission electron microscopy* (STEM) a narrow beam (diameter ≈ 0.1 nm) is scattered across the sample. The objective lens recombines the transmitted electrons from all points scanned by the probe beam to a fixed region in the back focal plane to be detected.
Electron Energy Loss Spectroscopy (EELS) is the analysis of the energies distribution of electrons transmitted through the sample. In fact, EELS is measured by the electron energy loss due to inelastic collisions. This is only a primary process and is not based on a secondary event related to X-ray emission when an excited atom returns to its ground state. For this reason, it is a more efficient process, especially for low-Z elements. EELS is primarily used to provide microanalytical and structural information approaching the very high resolution of TEM.
In this thesis, TEM analyses have been used in order to obtain information on the microstructure and composition of the metal/semiconductor contacts

and interfaces upon annealing treatments. A 200 kV JEOL 2010 F microscope has been used.

3.1.4 Photoluminescence Spectroscopy

Photoluminescence spectroscopy is widely used for the investigation of optical processes within semiconductors, especially in WBG varieties such as SiC, GaN or AlGaN [43,44]. When these materials are exposed to light with energy $h\nu$ (h being the Planck constant and ν being the photon frequency) larger than the gap E_g, an electron is promoted up to the conduction band thus leaving a hole in the valence band. This excited state, formed by the electron-hole pair, can decay through two kinds of processes: 1) *radiative,* with spontaneous emission of photons (photoluminescence); *non-radiative,* assisted by phonons with a rate that depends on the temperature. The main photoluminescence processes are: 1) recombination of the electron-hole pair, also called exciton if it is in a bound state, the emitted photon has energy $h\nu_{em}$ very close to E_g; 2) transition from intragap states localized on point defects, the emission energy $h\nu_{em}$ is minor than E_g, the shift being of the order of 1 eV.

In this thesis we performed *time resolved luminescence spectra* by using the setup reported in Fig. 3.6, consisting of a *Tunable Laser System* as excitation source, a *Spectrograph* as a dispersion system and an *intensified CCD camera* as a detector. The Tunable Laser (VIBRANT OPOTEK) is an integrated system, in which the third harmonic (355 nm) of a pulsed Nd:YAG laser (pulse width of 5 ns, repetition rate of 10 Hz) is used to pump an Optical Parametric Oscillator (OPO) that converts it into a tunable output from 410 nm to 2400 nm. The laser is also equipped with a nonlinear crystal for the second-harmonic generation that covers the range 210 nm to 410 nm.

The light emitted from the sample was collimated in the spectrograph mounting a grating with 150 grooves mm^{-1} and a 300 nm blaze. Spectra were acquired by a CCD camera (PIMAX Princeton instruments), driven by a delay generator that regulates the time acquisition.

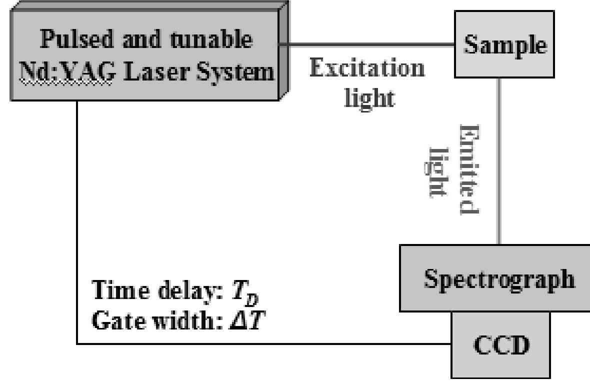

Fig. 3.6. Schematic of time resolved luminescence set up.

The main temporal parameters are the gate window, Δt, that is the time during which the CCD is enabled to reveal the luminescence light, and the delay, T_D, with respect to the arrival of the laser pulse. This allows the time-resolved detection, where the revealed signal, *F(t),* is the luminescence emitted from the sample, *I(t)*, integrated in a time interval that goes from T_D to ($T_D + \Delta t$), in agreement to:

$$F(t) = \int_{T_D}^{T_D+\Delta t} I(t')dt' \quad (44)$$

3.2 Electrical characterization

3.2.1 Transmission Line Model (TLM)

As discussed in Section 2.2, the parameter typically used to describe the Ohmic contacts is the specific contact resistance ρ_c (Ωcm^2), which is an intrinsic properties of the metal/semiconductor system and is independent of the contact geometry. The Transmission Line Model (TLM) [45], either linear TLM (L-TLM) or circular TLM (C-TLM), is the most common method used for the determination of ρ_c. The L-TLM method is schematically illustrated in Fig. 3.7.

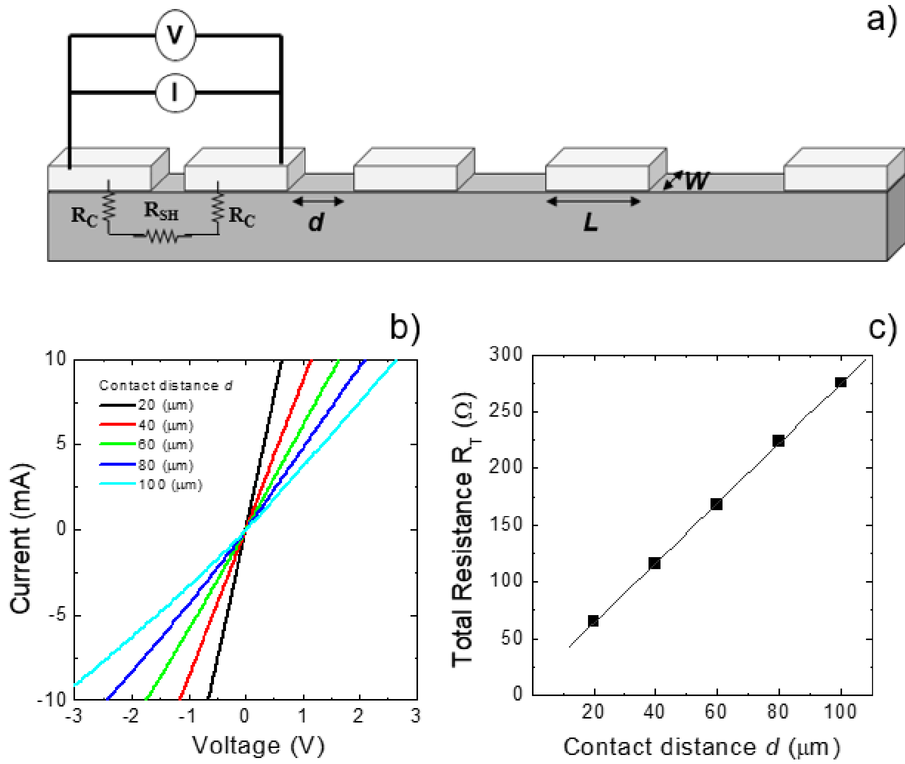

Fig. 3.7: Schematic of a L-TLM structure (a); Example of I-V measurements on adjacent TLM contacts placed at different distance *d* (b); linear plot of the total resistance R_T as a function of the contacts distance *d* (c).

A L-TLM structure consists of several contact pads with identical sizes, of length *L* and width *W*, placed at different distances *d* (Fig. 3.7 (a)).
When a current *I* is injected between two adjacent pads, the potential under a contact in a certain position *x* will depend on the specific contact resistance ρ_c and on the semiconductor sheet resistance R_{SH} following the equation:

$$V(x) = \frac{I\sqrt{R_{SH}\rho_c}}{W}\frac{cosh[(L-x)/L_T]}{\sinh(L/L_T)} \tag{45}$$

where is the so called transfer length L_T. The voltage drops nearly exponentially with the distance from the contact edge (x=0). The transfer length L_T is the distance where the voltage drops to 1/*e* of its highest value, and is is defined as:

$$L_T = \sqrt{\rho_c / R_{SH}} \tag{46}$$

The contact resistance R_c is calculated from the voltage drop V measured between two adjacent contacts at x=0, considering the Eq. (45):

$$R_c = \frac{V}{I} = \frac{\sqrt{R_{SH}\rho_c}}{W}\coth(L/L_T) = \frac{\rho_c}{L_T W}\coth(L/L_T) \tag{47}$$

Fig 3.7 (b) shows the I-V curves measured in a L-TLM structure between adjacents contacts as a function of the pads distances d. The total resistance R_T measured between two adjacent pads placed at a distance d is given by the sum of the contact resistance of the two pads (2 R_C) and the semiconductor resistance R_s.
Hence, R_{TOT} can be expressed as:

$$R_T = 2R_c + \frac{R_{SH}}{W}d \tag{48}$$

where R_{SH} is the sheet resistance of the semiconductor.
From the linear fit of the R_T vs d plot (Fig. 3.7(c)), it is possible to extract the contact resistance R_C and the transfer length L_T , as the intercepts of the fit at d = 0 and at R_T = 0, respectively. The semiconductor sheet resistance R_{SH} can be determined from the slope of the fit.
Finally, the specific contact resistance ρ_c can be determined as:

$$\rho_c = R_c W L_T tgh(L/L_T) \tag{49}$$

The TLM theory is based on the assumption that the current is forced to flow within the width of the resistor W. However, in the real case, part of the current flows also laterally, out of the contact width. For that reason, an isolation is realized around the contacts, very close to the contact width, with the aim of forcing the current to flow in one direction. The TLM method assumes that the contact width W and the width of the entire structure are identical. However, in the real cases, the contact width is smaller than the width of the TLM resistor. In our case, the isolation trench was at distance of 10 µm from the contact pad. Under these conditions, the current crowding effects at the contact edge are negligible, and do not significantly impact the contact resistance measurement. Hence, even in the presence of a lateral isolation, this condition is not satisfied, thus leading to a non-complete suppression of the lateral current. The way to

overcome this problem is to realize circular TLM structures, which do not need a lateral isolation and, hence, are simpler to be fabricated. The circular TLM (C-TLM) structure consists in a sequence of circular sized metallic contacts of radius *L* placed at different distance *d*, as schematically shown in Fig. 3.8).

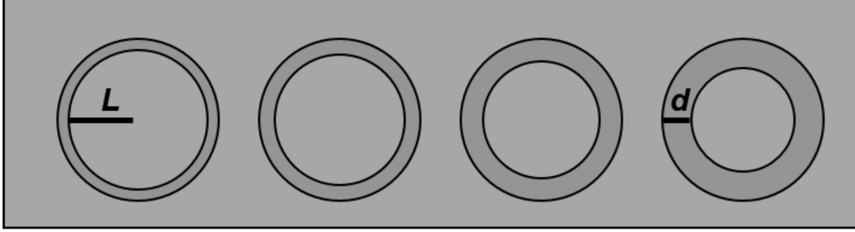

Fig. 3.8. Schematic of a C-TLM structure.

The contacts are circularly symmetrical. Then, by applying a bias between the external and the internal contact, the current will flow in the radial direction. In this case, the total resistance R_T is given by [46]:

$$R_T = \frac{R_{SH}}{2\pi}\left[\frac{L}{L_T}\frac{I_0(L/L_T)}{I_1(L/L_T)} + \frac{L_T}{L+d}\frac{L}{L_T}\frac{K_0(L/L_T)}{K_1(L/L_T)} + \ln(1+\frac{d}{L})\right] \quad (50)$$

where I and K are the Bessel functions of the first order.
For large structures, $L>>d$, Eq.(51) becomes

$$R_T = \frac{R_{SH}}{2\pi L}\left[L \cdot \ln\left(1+\frac{d}{L}\right) + 2L_T\right] = \frac{R_{SH}}{2\pi L}(d \cdot C + 2L_T) \quad (51)$$

Where $C = \frac{L}{d} ln\left(1+\frac{d}{L}\right)$ is the corrector factor.
And for $d/L<<1$, R_T takes the following expression

$$R_T = L_T\frac{R_{SH}}{\pi L} + \frac{R_{SH}}{2\pi L}d \quad (52)$$

Also in this case, the linear fit of the R_T vs d plot enables to extract the contact resistance R_C and the transfer length L_T , as the intercepts of the fit at $d = 0$ and at $R_T = 0$, respectively. R_{SH} can be determined from the slope. Considering the definition of L_T:

$$L_T = \sqrt{\rho_c / R_{SH}} \tag{53}$$

The ρ_c can be determined from:

$$\rho_c = R_{SH} L_T^2 \tag{54}$$

Clearly, the sensitivity of these techniques strongly depends on the metal/semiconductor properties. In fact, for high values of R_{SH} (and then R_T) it become very difficult to extrapolate low value of ρ_c.
The fabrication process of L-TLM and C-TLM adopted in this thesis is described in Section 3.3.

3.2.2 Van der Pauw and Hall-effect measurements

The combination of Van der Pauw and Hall effect measurements give information on the electrical properties of semiconductor layers, allowing the determination of the resistivity ρ (Ω·cm), the carriers concentration (carriers/cm^3), their sign (i.e., holes or electrons) and their mobility μ (cm^2/V·s).
The Van der Pauw method consists in a current-voltage measurement carried out in an appropriate configuration. Typically, different geometries can be realized to perform these measurements [47].

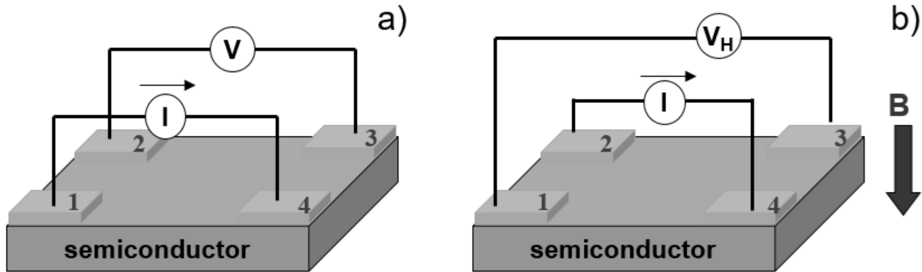

Fig. 3.9. Schematic of the experimental configuration used for Van der Pauw (a) and Hall effect measurements (b).

As an example, Fig. 3.9(a) schematically depicts a square shaped Van der Pauw structure, with four Ohmic contacts placed on the sample periphery.

Such kind of structure has been used in this thesis. The fabrication process is described in section 3.3.
In a Van der Pauw measurement, a current I is injected through one pair of contacts and the voltage V is measured on the other pair of contacts. From the measured resistance $R_{12,34}$ is possible to determine the sheet resistance R_{SH} (Ω/sq) and resistivity ρ of the semiconductor layer:

$$R_{12,34} = \frac{V_{34}}{I_{12}} \quad (55)$$

$$R_{SH} = \frac{\pi}{ln2} R \quad (56)$$

$$\rho = R_{SH} t \quad (57)$$

where t is the thickness of the layer.
The Hall effect measurements allows the determination of the sheet carrier density of a semiconductor layer. In the Hall measurements, a magnetic field B is applied perpendicular to the current flow (Fig. 3.9(b)). In this configuration, an electric field perpendicular to I and B directions is produced and the separation of the carriers induces a Hall voltage V_H between the second pair of contacts.
A charged particle in a magnetic field is subjected to the Lorentz force F_L, proportional to its velocity and to the magnetic field:

$$F_L = q(E + v \times B) \quad (58)$$

The current I can be expressed as a function of the carriers velocity and concentration. Hence, for a p-type semiconductor :

$$I = pAvq \quad (59)$$

while for an n-type semiconductor:

$$I = -nAvq \quad (60)$$

where p and n are the carrier densities and A is the cross-sectional area of the conductor.
Considering the case of a p-type semiconductor (which will be described in this thesis in chapter 5), the drift velocity v is given by:

$$v = \frac{I}{pAq} \tag{61}$$

The electric field is then given by:

$$E = Bv = \frac{BI}{pAq} \tag{62}$$

Then the Hall voltage is calculated from the integral of the electric field:

$$V_H = -\int_W^0 E_y = \frac{BI}{ptq} \tag{63}$$

The Hall coefficient R_H (m^3/C) is defined as:

$$R_H = \frac{V_H t}{IB} \tag{64}$$

From Eq. (64) it is possible to calculate the hole concentration value:

$$p = \frac{1}{qR_H} \tag{65}$$

Analogous consideration can be made for n-type semiconductors, thus leading to the following expression for the electron concentration:

$$n = -\frac{1}{qR_H} \tag{66}$$

Then, the combination of a Van der Pauw measurement (to determine the semiconductor sheet resistance) and a Hall measurement (to determine the sheet carrier density) makes possible to extract the carrier mobility as:

$$\mu_p = \frac{1}{qpR_{SH}} \tag{67}$$

$$\mu_n = -\frac{1}{qnR_{SH}} \tag{68}$$

In this work, a MMR Hall Effect Measurement System H-50 equipment has been used (Fig. 3.10).

Hall measurements were carried out either at room temperature to determine the sheet electron density of the 2DEG in AlGaN/GaN heterostructures (chapter 4), or for keeping the sample at different temperatures in the range of 300-500 K to study the electrical properties of p-type implanted 4H-SiC layers (chapter 5).

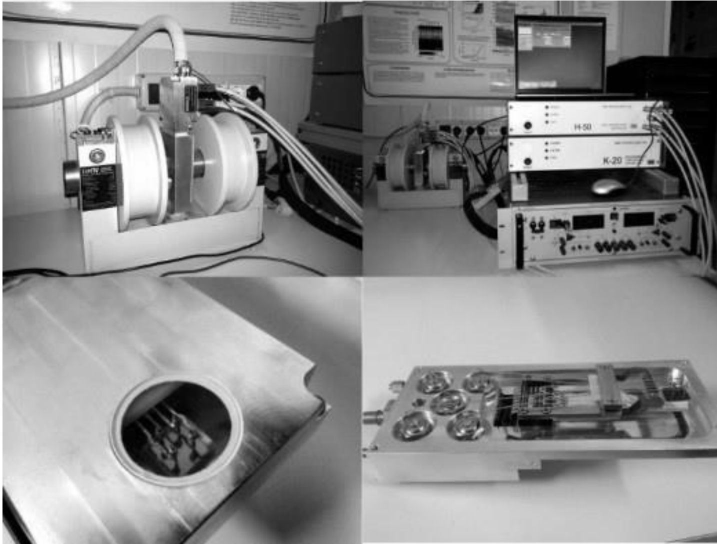

Fig. 3.10. Hall-effect measurement equipment of the CNR-IMM of Catania.

3.3 Fabrication of test patterns for electrical characterization

The electrical characterization of GaN and SiC samples carried out in this thesis required the fabrication of appropriate test patterns. This was a part of the experimental work and has been carried out in the clean room of CNR-IMM in Catania (photo on Fig. 3.11). The clean room is equipped with several tools, e.g., wet benches (for sample cleaning and wet etching), optical direct write lithography (for the definition of contacts), plasma etch (for the isolation of TLM and VdP structures), rapid thermal annealing furnaces (for Ohmic contact formation).

Fig. 3.11. Clean room of CNR-IMM in Catania.

Some processing steps (i.e., Al-implantation and high temperature annealing of 4H-SiC samples) been performed in the R&D line at STMicroelectronics in Catania. In this work, both L-TLM and C-TLM patterns have been used. The flow chart of fabrication is described as follows and is schematically shown in Fig. 3.12.

Process description	**Equipment**	**Notes**
Cleaning of the wafer	Wet bench	For AlGaN/GaN : - $HF:HCl:H_2O$ (10 min) For SiC: - $H_2SO_4:H_2O_2$ 3:1 (10min); - HF (10 min)
Photoresist deposition	Spin coater BLE	- AZ 3012 (2000 lap/min, 1 min) - Resist thickness: 1.5 um - Bake: 100 °C
Optical photolithography	DWL66 Heidelberg Instruments	Solide State Laser λ 405 nm., power 3 mW
Resist development	Wet bench	AZ 726 MIF
Postbake	BLE Hot Plate	T=120°C (2 min)
Plasma etching for isolation	ICP Roth and Rau	Ar/CHF_3
Resist removal	Resist removal	Acetone
Photoresist deposition	Spin coater BLE	Ar 5320 - 4000 lap/min (1 min) Resist thickness: 1 um Bake T=105 °C (3 min)
Optical photolithography	DWL66 Heidelberg Instruments	Solide state laser λ 405 nm., power 1 mW
Resist development	Wet bench	AR 300-26
Postbake	BLE Hot Plate	T=105°C (2min)
Metals deposition	QUORUM Q300TD	Metal deposited by sputter technique
Resist removal by lift-off process	Wet bench	- Acetone (T=90°C) - Ultrasound bath

Rapid Thermal Annealing	Jipelec JetFirst furnace	Temperature 400-950 °C (depending on sample) in Ar environment

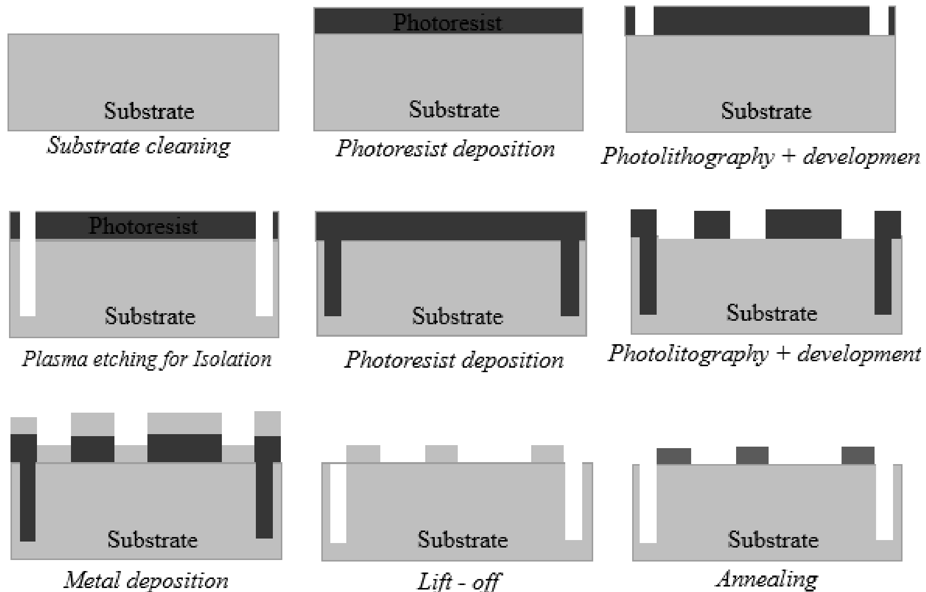

Fig. 3.12. Schematic representation of the flow-chart for the fabrication of the test patterns structures.

The fabricated L-TLM structures consisted of rectangular pads (100 µm × 200 µm), at distances *d* varying between 20 and 100 µm or 5 and 25 µm. The C-TLM structures have been fabricated with a radius of 200 µm and distances *d* varying between 5 and 25 µm. In the case of C-TLM structures, it is possible to avoid the fabrication steps of photolitography and plasma etch needed to obtain the isolation. In fact, in C-TLM the current is confined between the contacts because of the circular geometry.
Fig. 3.13 shows the mask design used for the fabrication of L-TLM and C-TLM performed by means of Autocad program, together with optical images of L-TLM and C-TLM structures.

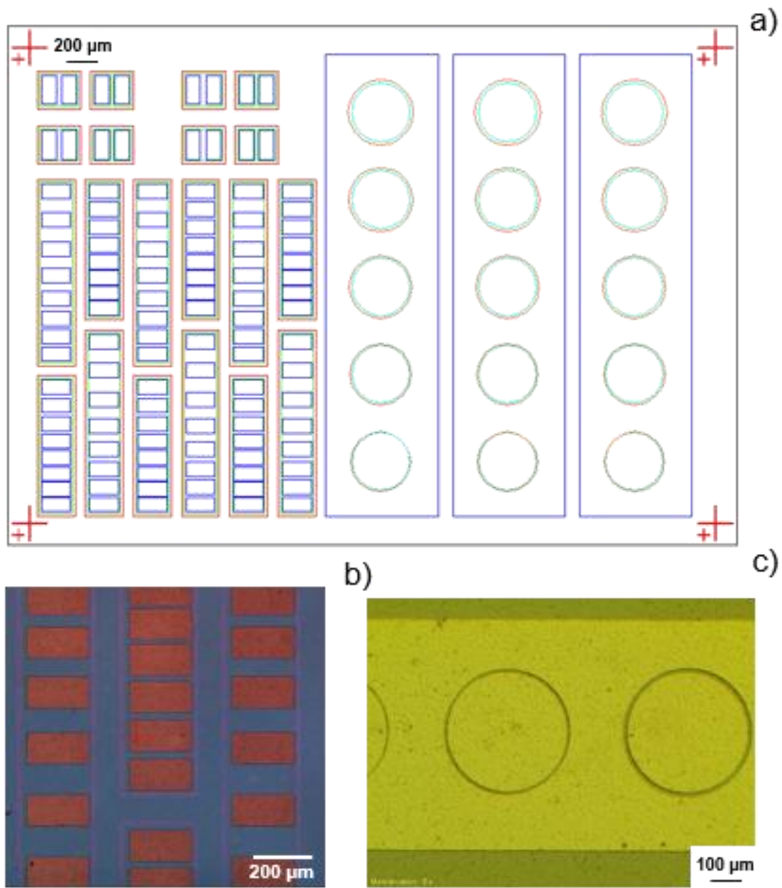

Fig. 3.13: Mask design used to fabricate the test pattern (a) and optical images of L-TLM (b) and C-TLM (c) structures.

Similarly, Van der Pauw structures have been fabricated following the same flow chart. In this case, the mask for the contacts definition consists of 4 squared contacts with contact length of -1 cm, placed at a distance of 4 mm one to each other. The Van der Pauw structure is fabricated on a 1x1 cm substrate square. Fig. 3.14 shows the masks design and the optical image of the Van der Pauw structure.

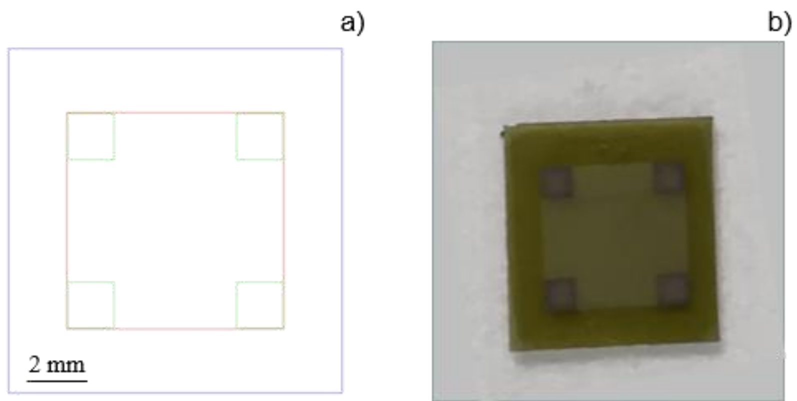

Fig. 3.14: Mask design used to fabricate the test pattern (a) and optical images of Van der Pauw structure (b).

Chapter 4 – Ohmic contacts on AlGaN/GaN heterostructures

As specified in Section 1.2, AlGaN/GaN heterostructures are very interesting systems employed for the fabrication of high electron mobility transistors (HEMTs). Good source and drain Ohmic contacts, with a low specific resistance, are required to improve the performance of HEMTs devices. Moreover, in GaN-on-Si technology, it is important to realize Au-free Ohmic contacts. This chapter reports a study of Au-free Ohmic contacts. The experiments were carried out both on Ti and Ta based contacts, comparing the structural, morphological and electrical behaviour and providing insights on the carrier transport mechanism at the metal/semiconductor interface. At the end of this chapter, a modification of the TLM method, which can be used to quantify the modification of the sheet resistance under the contact, will be described.

4.1. State of the art on Ohmic contacts on AlGaN/GaN heterostructures

Ohmic contacts on GaN-based materials have been widely investigated in the last decades [48], exploring several combinations of metals layers and annealing conditions. The most common solutions adopted on AlGaN/GaN heterostructures are Ti/Al/X/Au multilayers (where X = Ni, Mo, Ti…), which typically reach an Ohmic behavior after annealing at 800-850°C [49,50]. In these systems, each metal layer has a specific influence on the final structural and electrical properties of the contact. In particular, a low work function metal ("contact layer") is directly connected with the AlGaN substrate, in order to reduce the metal/semiconductor barrier height and enables a minimum the contact resistance. Refractory metals (e.g., Ti,Ta,. . .) are well suitable for this purpose, because they can react with AlGaN forming new intermetallic phases and nitrides at the interface [51]. An "overlayer", generally Aluminium (Al), is deposited on the top of the contact layer. In fact, Al can easily form low work function compounds

with the other metals. A third layer, called "barrier layer", made by high melting point metals (Ni, Ti, Pt, Pd, Mo, …), serves to stabilize the multilayer during annealing, limiting the inter-diffusion between the first two metal layers and the uppermost layer. Noteworthy, the barrier layer also participates in the reaction with the other metals and, hence, its choice has a non-negligible impact on the contact properties [52]. Finally, the uppermost "cap layer", typically Au, is used to prevent the surface oxidation, but it also forms highly conductive phases upon annealing, which improve the electrical conduction of the entire reacted stack and its contact resistance [34]. The presence of Au inside the stack is considered as one of the causes of the high surface roughness of the contacts after thermal annealing [53]. This aspect is very important, since the surface roughness, together with a poor edge acuity of the contacts, are detrimental for the device reliability. In addition, the increasing interest to integrate GaN-on-Si HEMTs technology on the existing Si CMOS fabrication lines imposes the adoption of "Au-free" solutions for source-drain Ohmic contacts. This is still a challenging aspect in GaN-based HEMT technology and was object of investigation in this thesis.

Several routes to obtain low resistance Au-free Ohmic contacts have been proposed in literature.

A first possibility is appropriately tailoring the AlGaN material to ameliorate the electrical properties of the contacts. The use of intentionally doped AlGaN barrier layer has been proposed to improve the contact resistance, but this approach inevitably leads to an increase of the gate leakage current of the device [54]. Moreover, the local n-type doping of AlGaN/GaN heterostructures below the contact by Si-ion-implantation favors the achievement of an Ohmic behavior. However, the implantation doping requires high temperatures for electrical activation that can severely degrade the nitride material surface [55]. The use of n-GaN layer under the metal has been employed to reduce the contact resistance, but this solution is significantly complex [56].

In principle, the easiest approach to fabricate Au-free Ohmic contacts is the removal of the Au cap layer from a conventional Ti/Al/X/Au stack. Indeed, several contacts based on Ti/Al or Ti/Al/Y covered by a cap layer have been reported (Ti/Al, Ti/Al/TiN, Ti/Al/W) [57,58,59,60,61,62]. Moreover, also the combination with Ta has been considered because of the low work

function, similar to Ti [63,60]. The electrical properties of Au-free contacts depends on several processing parameters, such as the metals thickness, the thermal annealing conditions, or the nitride material quality [64,65]. The formation of new phases at the interface after annealing is one of the key factor for the improvement of the electrical characteristics.
Many works in literature reported on the formation of TiN [53,61,66,67,68,69] or TaN [70,71] phases at the interface as a result of the reaction between Ti or Ta and AlGaN. In particular, this phase is formed because of the extraction of N atoms from AlGaN, inducing a high concentration of N-vacancies, which act as n-type doping, thus decreasing the contact resistance. Equally important is the formation of phases between Ti and Al or Ta and Al. In particular, in Ti-based contacts, it has been reported that for low annealing temperatures (<650°C) the favored phase is the Al_3Ti [60,72], while increasing the annealing temperature also the formation of Al_2Ti or Ti_2AlN phase occur [58]. In Ta- based contacts, the Ohmic behavior has been also related to the $TaAl_3$ phase formation into the metal stack, that is the most stable phase between 600 C and 1500 C for Ta concentrations between 25% and 35% [60,73]. However, in Au-free contacts it has been observed that the Ohmic behavior is achieved at annealing temperatures lower than temperatures required for Au-based contacts [50].
Another parameter that strongly influences the Ohmic contact formation is the Ti/Al ratio [58, 62]. In particular, for a certain annealing condition, an optimum Ti/Al relative thickness can be achieved in order to minimize the contact resistance. Thinner Ti layers are necessary to avoid the formation of voids below TiN and a thicker Al layer is able to reduce the aggressivity of the reaction between Ti and AlGaN [58,61,62,74]. Similarly to Ti-based Ohmic contacts, metal layer thicknesses strongly impact on the contact resistance, resulting in the lowest value of R_c for a Ta/Al ratio of about 10 [63,75].
Finally, a peculiarity of both Ti and Ta Au-free Ohmic contacts is the improved surface morphology with respect to the metallizations containing Au [34,38,53,59,63,76]. In fact, the annealing temperature required for the Ohmic contact formation, lower than the aluminum-layer melting point (<660°C), leads to a better morphology of the contact area [77]. Indeed, the

presence of Au leads to the formation of Al-Au phases, which are responsible for a high surface roughness of the reacted layer [78].
Beyond considering all the parameters discussed so far, a method to improve the electrical properties of Ohmic metals is to use “recessed contacts”. The recession consists in the complete or partial removal of the AlGaN barrier layer below the Ohmic contact. In particular, reducing the distance between the metal interface and the 2DEG favors the electron tunneling, reducing the specific contact resistance of recessed contacts with respect to conventional ones. Lee et al. [79] obtained good Ohmic contacts on AlGaN/GaN heterostructure using TiAlW contacts annealed at 870°C.
From a critical analysis of the literature results, some aspects related to Au-free Ohmic contact formation are still not clear, e.g., the role of the contact layer, the thickness of the metal, the phases responsible for Ohmic contacts formation, the mechanism of carrier transport at the interface, etc. To gain a deeper comprehension of the Au-free Ohmic contact formation based on low work function metals, in this thesis a comparative study of Ti- and Ta-based systems has been carried out. A special emphasis has been given to the correlation between the macroscopic electrical behaviour and the interfacial microstructure, corroborating the results by the determination of the metal/semiconductor barrier height by temperature dependent TLM measurements.

4.2. Characterization of the AlGaN/GaN heterostructures

Commercial AlGaN/GaN heterostrutcture grown on Si (111) substrates have been used for the study of the Ti- and Ta- based Ohmic contacts. The nominal AlGaN barrier layer was of 16 nm thick and the percentage of aluminum concentration was of 25%. First, a characterization of the incoming material has been carried out, employing different techniques.
Fig. 4.1 shows the AFM images of the AlGaN/GaN heterostructure surface acquired on different scan areas. As can be seen, for low areas, 2×2 μm^2 (Fig. 4.1 (a)) and 5×5 μm^2 (Fig.4.1 (b)), the surface appears quite smooth, showing the typical atomic steps of the AlGaN, with RMS values of 0.14 nm and 0.40nm, respectively. By increasing the scanning area, a higher

surface roughness is measured, RMS=0.73 nm for a 10×10 μm² area (Fig. 4.1 (c)) and RMS=1.56 nm for a 20×20 μm² scan area (Fig. 4.1 (d)).
The aluminum concentration of the AlGaN layer has been verified by means of photoluminescence measurements. Fig. 4.2 shows the PL spectrum acquired on the AlGaN/GaN heterostructure. In this spectrum, two signal have been detected, i.e., the peak at about 4.2 eV that is related to the emission from the AlGaN, and the peak at 3.4 eV that is related to the emission from the GaN. For comparison, Fig 4.2 shows also the PL emission of a bulk GaN sample, peaked at 3.4 eV, which corresponds to the GaN bandgap.

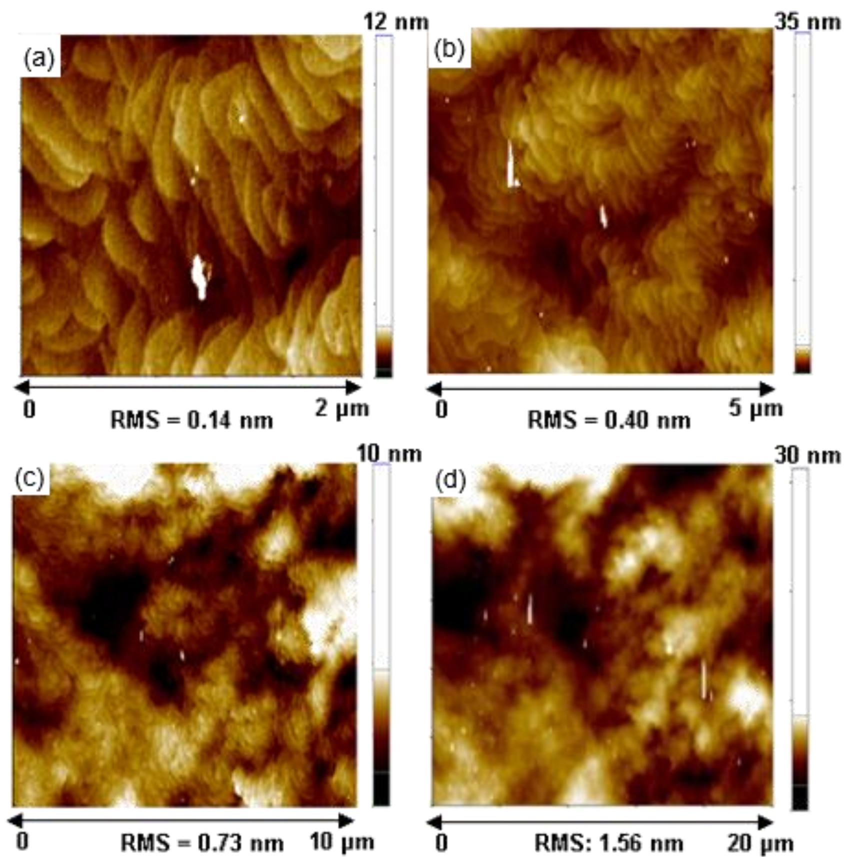

Fig. 4.1. AFM images acquired on 2×2 μm² (a), 5×5 μm² (b), 10×10 μm² (c) and 20×20 μm² (d) scan areas of AlGaN/GaN heterostructure surface.

From these data, it was possible to estimate the Al concentration(x) of the) in the $Al_xGa_{1-x}N$ alloy, using the relation:

$$E_g(Al_xGa_{1-x}N) \approx (1-x) \cdot E_g(GaN) + x \cdot E_G(AlN) \qquad (69)$$

By using the value of $E_g(Al_xGa_{1-x}N) \approx 4.2$ eV, determined by the PL measurements, allowed us to estimate a value of $x \approx 0.28$. This value is in reasonable agreement with the nominal Al concentration given by the material provider.

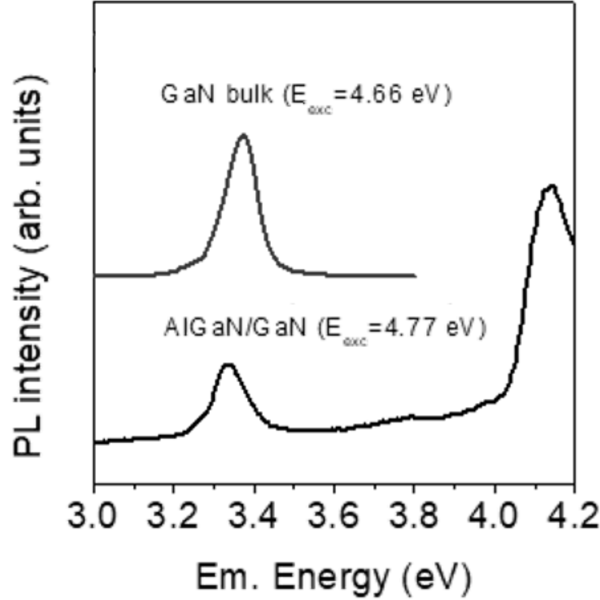

Fig. 4.2. Photoluminescence (PL) spectrum of the AlGaN/GaN heterostructures, excited at 4.77 eV (black line) and PL spectrum of GaN bulk and detected excited at 4.66 eV (red line). Both the spectra have been detected with a time window T_W =1 ms and a time delay T_D =0 ns.

Fig. 4.3 shows the cross section TEM analysis of the AlGaN/GaN heterostructures. From this image, it was possible to identify the heterostructure layers and measure an AlGaN barrier thickness of 16 nm. Finally, the sheet carrier density of the 2DEG at the AlGaN/GaN interface has been determined from Hall-effect measurements. The van der Pauw structure has been fabricated with the procedures described in section 3.3, using Ti(10nm)/Al(300nm)/Ti(20nm) square contacts at the sample corners, subjected to annealing at 600°C for 60s in Ar. Fig. 4.4 shows a representative I-V curve measured on van der Paw structures.

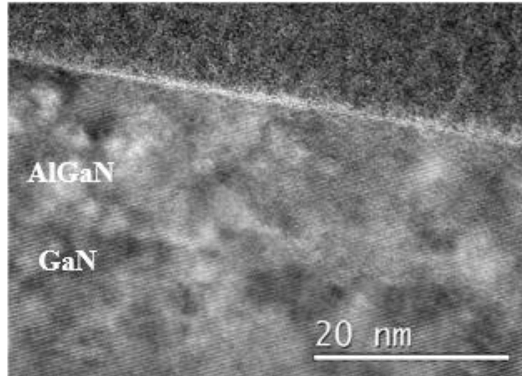

Fig. 4.3. Cross section TEM image of an AlGaN/GaN heterostructure used in this thesis.

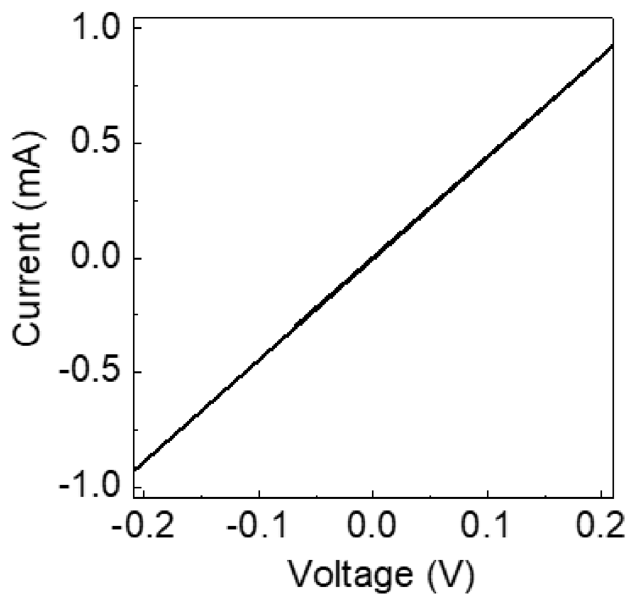

Fig. 4.4. I-V curve measured on van der Paw structures fabricated on AlGaN/GaN heterostructure.

From these measurements, a sheet carrier density of the two dimensional electron gas (2DEG) $n_s=7.45\times 10^{12}\ cm^{-2}$ could be determined.

4.3 Ti- and Ta- based Ohmic contacts on AlGaN/GaN heterostructures

The properties of $Ti_{(10nm)}/Al_{(300nm)}/Ti_{(20nm)}$ and $Ta_{(10nm)}/Al_{(300nm)}/Ta_{(20nm)}$ on AlGaN/GaN heterostructures have been investigated, performing a direct comparison of the two systems by means of morphological, structural and electrical characterization techniques. The metal stacks have been deposited by sputtering and TLM structures have been defined by lithography and lift-off, as described in Section 3.2.1. For the structural analyses, blanket samples have been used. Then, the contacts have been subjected to thermal annealing processes at different temperatures in the range 400°C- 600°C. Basing on previous literature results, moderate annealing temperatures (≤ 600°C) and short annealing times (≤ 3min) have been chosen in this thesis to avoid contact degradation. The electrical response has been analyzed with the TLM method (see section 3.2.1).
Figs. 4.5 (a) and 4.5 (b) report the I-V curves acquired on adjacent pads of TLM structures based on Ta/Al/Ta and Ti/Al/Ti. The curves have been measured between contacts placed at a distance of 20 μm after different annealing treatments.

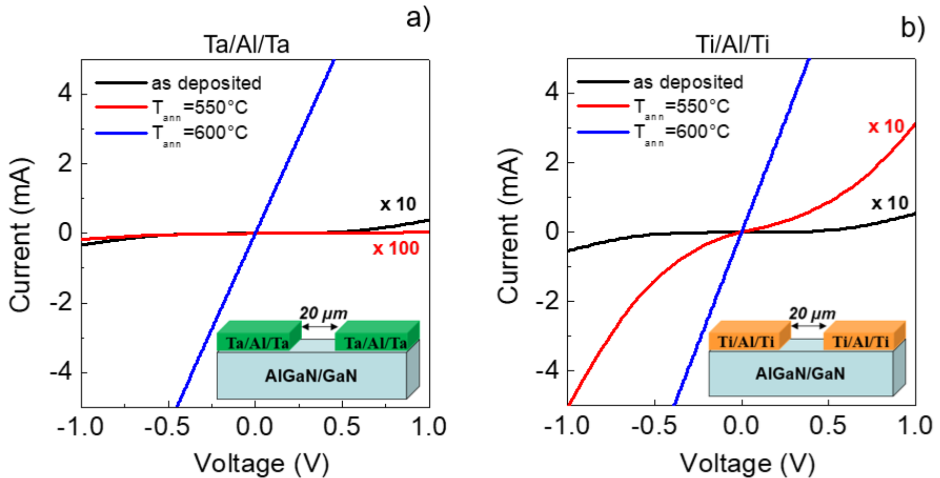

Fig. 4.5. I-V curves acquired between adjacent TLM pads placed at a distance of 20 μm in Ta/Al/Ta (a) and Ti/Al/Ti (b) after deposition (as deposited) and annealing at different temperatures (550°C and 600°C).

The I-V characteristics of the contacts exhibited a non-linear behavior after deposition (as deposited) and annealing at temperatures up to 550°C. Such curves reported in Fig. 4.5 have been multiplied by a factor of 10 or 100 in order to be more visible in the graph. The Ohmic behaviour is achieved after annealing at 600°C. Noteworthy, the Ti-based contact showed an Ohmic behavior after an annealing process of 60s at 600°C, while a longer annealing duration (180s) was needed for the Ta- based contact.
In order to understand the mechanism of Ohmic contact formation in the two systems, the samples at the onset annealing condition have been considered, i.e., the Ta/Al/Ta sample annealed at 600°C for 180s and the Ti/Al/Ti sample annealed at 600°C for 60s. The I-V curves acquired on TLM structures in both Ta/Al/Ta and Ti/Al/Ti samples annealed at 600°C are shown in Fig. 4.6 (a) and Fig. 4.6 (b), respectively. As can be seen, the current decreases with increasing the TLM pad distance. Moreover, Ti/Al/Ti contacts show a higher current level.
Fig. 4.6 (c) and Fig. 4.6 (d) report the total resistance R_{TOT} , determined from the slope of the I-V curves, as a function of the distance d between adjacent TLM pads. I-V curves have been acquired on several TLM patterns, and the reported results are an average on tests performed in different positions of the samples. As expected by the TLM theory, the average R_{TOT} increases linearly with the pad distance. The value of specific contact resistance ρ_c extracted for the Ti/Al/Ti contacts was $\rho_{c\ (Ti/Al/Ti)}$ = $1.6 \pm 0.6 \times 10^{-4}\ \Omega.cm^2$, i.e., more than a factor of two lower than the value extracted in Ta/Al/Ta ($\rho_{c\ (Ta/Al/Ta)}$ = $4.0 \pm 1.1 \times 10^{-4}\ \Omega.cm^2$). Similar semiconductor sheet resistance values R_{SH} were extracted for the two contacts, R_{SH} = 472±10 Ω/□ for the Ti/Al/Ti sample and R_{SH} = 475±9 Ω/□ for the Ta/Al/Ta sample.

The formation of Ohmic contacts is generally associated with the modification of the morphology and/or of the microstructure of the layers upon annealing. To highlight this aspect AFM, XRD and TEM analysis have been performed on the two samples. Fig. 4.7 (a) and Fig. 4.7 (b) show the morphologies of the Ti/Al/Ti and Ta/Al/Ta as deposited contacts acquired on a 20µm × 20µm region. The as deposited metals show a morphology with a low roughness value for both the Ta- and Ti-based contacts of 9 nm and 10 nm respectively.

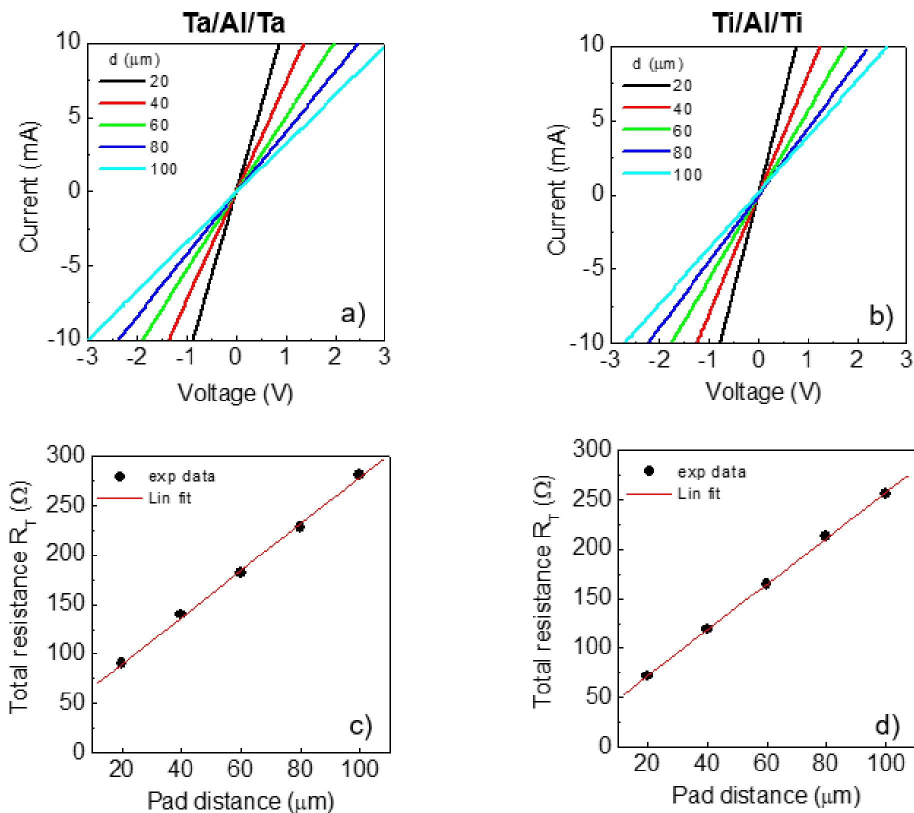

Fig. 4.6. I-V curves acquired on TLM structures in Ta/Al/Ta (a) and Ti/Al/Ti (b) contacts annealed at 600°C. Plots of the total resistance R_{TOT} as a function of the TLM pads distance *d* for Ta/Al/Ta (c) and Ti/Al/Ti (d).

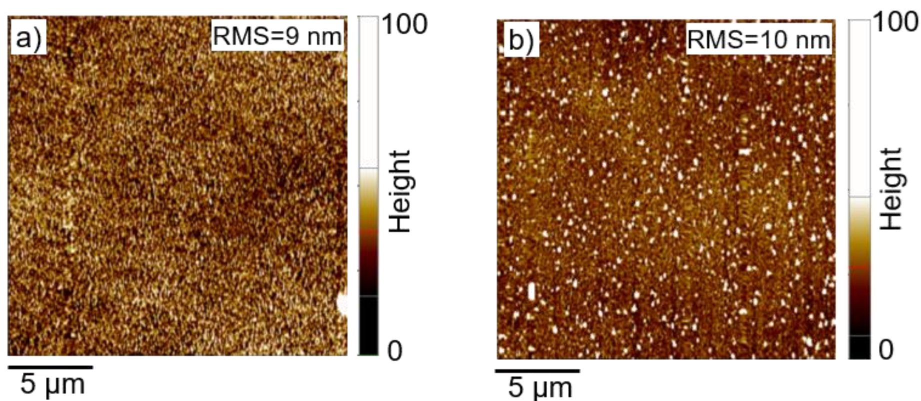

Fig. 4.7. AFM images of Ta/Al/Ta (a) and Ti/Al/Ti (b) as deposited contacts on 20μm ×20μm scan areas.

Fig. 4.8 (a) and Fig. 4.8 (b) show the morphology of the contacts annealed at 600°C, acquired on a 40µm × 40µm region. In both cases, the surface is characterized by flat areas with some isolated hillocks. The RMS roughness values are 48 nm and 79 nm for Ta- and Ti- based contacts respectively.

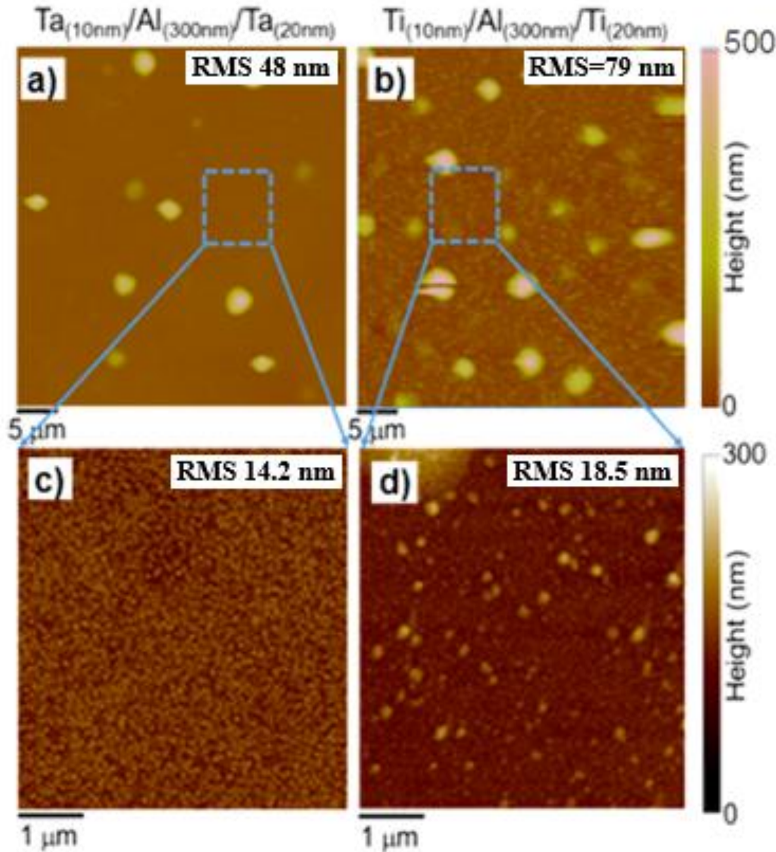

Fig 4.8. AFM images of Ta/Al/Ta contact on 40µm ×40µm (a) and 5µm ×5µm (c) scan areas and AFM images of Ti/Al/Ti contact on 40µm ×40µm (b) and 5µm ×5µm (d) scan areas after annealing at 600 °C.

These hillocks are more pronounced in the case of the Ti/Al/Ti system, thus justifying the higher RMS. Fig. 4.8 (c) and Fig. 4.8 (d) show the AFM images acquired on the flat areas on a 5µm × 5µm region. Interestingly, also in the flatter areas the Ta/Al/Ta contacts exhibited a lower roughness (RMS=14.2 nm) with respect to the Ti/Al/Ti samples (RMS=18.5 nm).

Despite the presence of such isolated hillocks, the two Au-free systems exhibited a flatter surface compared with that of standard Ti/Al/Ni/Au contacts formed at 800°C [76]. This result is important, since it demonstrates the technological advantage of using these contacts for device fabrication. The hillocks have been investigated from an electrical point of view by means of C-AFM analysis. The surface scanning has been performed with a conductive diamond coated tip, by applying a positive bias of +5V to the samples backside. Then, the current flowing to the tip across the metal/semiconductors interface was collected by a current amplifier connected to the tip. Figure 4.9 (a) and (b) show a representative morphological image and the corresponding current map on 20 μm × 20 μm scan area for the Ta/Al/Ta sample.

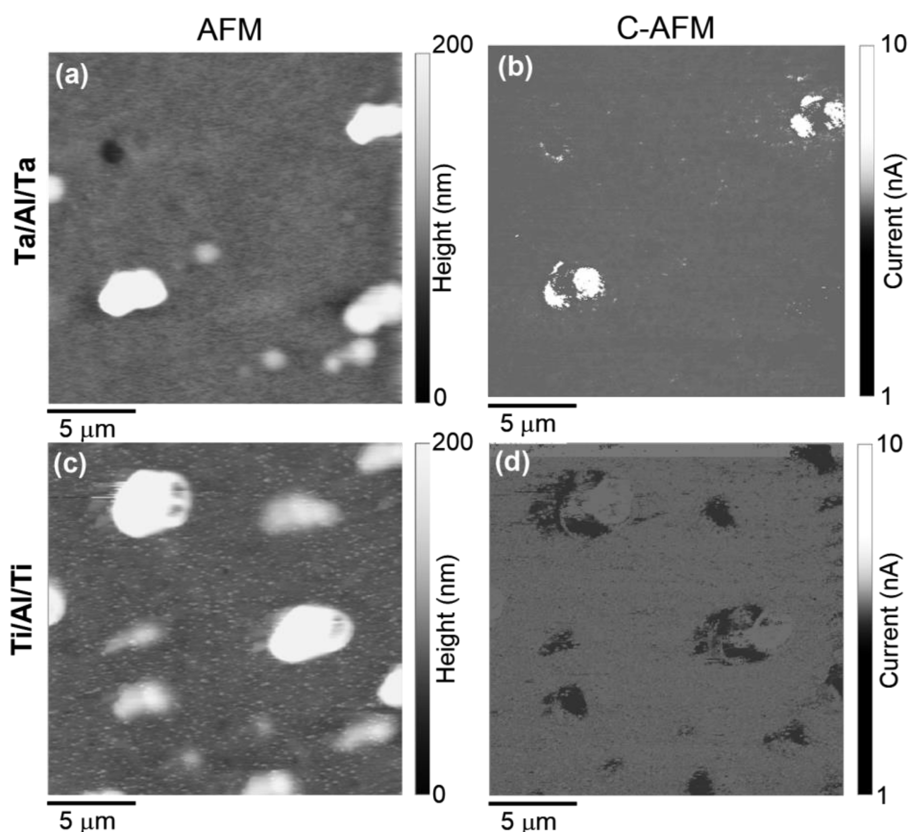

Fig. 4.9. (a) AFM image and (b) associated C-AFM map acquired on Ta/Al/Ta contact. (c) AFM image and (d) associated C-AFM map acquired on Ti/Al/Ti contact. The images were acquired on 20μm × 20μm scan areas.

The morphological and electrical analyses performed under the same conditions on the Ti/Al/Ti sample are reported in Figure 4.9 (c) and (d). As can be seen, there is a clear correlation between the surface features and the current maps on both samples. In particular, a uniform current level is detected in the flat areas of the samples. Furthermore, the hillocks in the Ta-based contacts display a higher conductivity with respect to the uniform background of the surrounding metal surface, whereas a lower conductivity has been observed over the hillocks in the Ti-based contacts. The different composition (e.g., the phase or the Al content presents in the core of the hillocks) can be responsible of the different conductivity detected by C-AFM analyses. However, the area occupied by the hillocks is only ~1% and ~5% of the overall contact area in Ta- and Ti- based systems, respectively. Hence, the contribution to the increase or the decrease of the total current flowing across the overall contact area is 1-2% in both cases. For these reasons, it can be argued that the presence of these hillocks on the surface does not significantly impact on the specific contact resistance.

XRD analysis, shown in Fig.4.10, has been performed to identify the main phases formed in the layer upon annealing at 600°C.

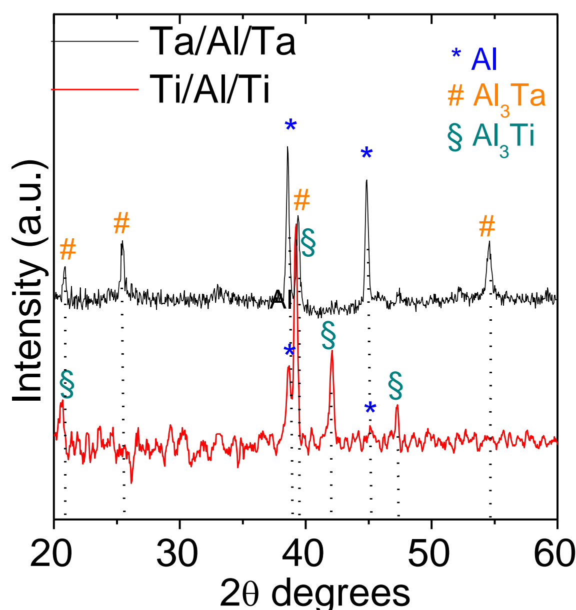

Fig 4.10. XRD patterns for Ta/Al/Ta and Ti/Al/Ti contacts annealed at 600°C, showing the presence of the Al_3Ta and Al_3Ti phases.

As can be seen, for Ti/Al/Ti contact Al_3Ti phase and unreacted Al have been identified. Typically, Ti reacts with Al and form Al_3Ti phase [80] for annealing temperatures higher than 450°C. According to the literature, in these systems unreacted Al can be still present also at higher annealing temperatures [58], which is consistent with our experimental observation. A similar behavior has been observed in the annealed Ta/Al/Ta contact. In this case, XRD analysis detected the Al_3Ta phase, coexisting with unreacted Al. In fact, the formation of Al_3Ta phase is expected in a temperature range between 600-1500°C [58,60]. The Al_3Ta and Al_3Ti phases are the most thermodynamically favored processes for the annealing temperature considered in our case [81].

As described in section 2.2, a quantitative description of the carriers transport mechanism through the metal/AlGaN interfaces can be given by monitoring the temperature dependence of the specific contact resistance ρ_c. For this purpose, TLM measurements have been performed using a hot chuck keeping the substrate at temperatures between 25°C and 175°C. The ρ_c values have been determined at each measurement temperature T. Fig. 4.11 shows the values of ρ_c as a function of the measurement temperature T for the two contacts.

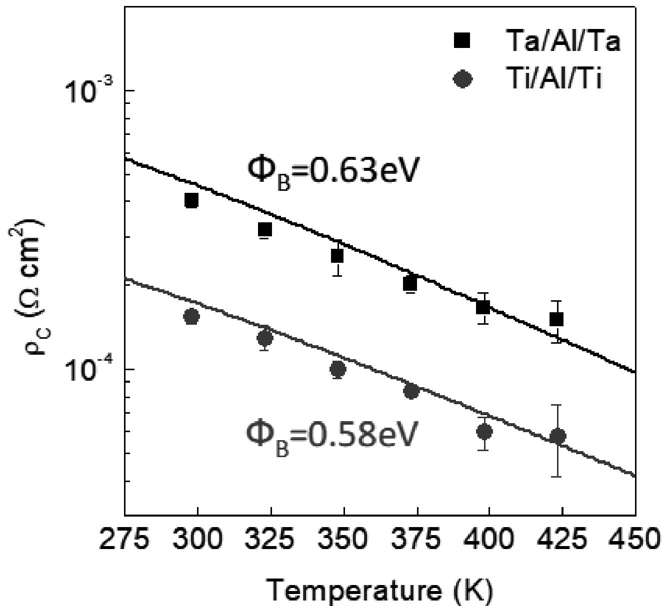

Fig 4.11. Specific contact resistance ρ_c as a function of the measurement temperature, T for the Ta/Al/Ta (squares) and Ti/Al/Ti (circles) contacts annealed

at 600°C. Solid lines are the fits of the experimental data with TFE model. The values of the barrier height extracted from the best fit procedure are also reported.

As can be seen, ρ_c decreases with increasing T and both samples exhibit a similar trend of the $\rho_c(T)$, in terms of temperature variation.

Among those described in chapter 2, the current transport mechanism that better fitted the experimental ρ_c values was the Thermionic Field Emission. Accordingly, the specific contact resistance ρ_C can be expressed as [82]:

$$\rho_c = \left(\frac{1}{qA^2}\right)\frac{k^2}{\sqrt{\pi(\Phi_B+V_n)E_{00}}}cosh\left(\frac{E_{00}}{kT}\right)\sqrt{coth\left(\frac{E_{00}}{kT}\right)}exp\left(\frac{\Phi_B+V_n}{E_0}-\frac{V_n}{kT}\right) \quad (70)$$

From the analysis of the data, the values of the Schottky barrier height could be determined as fit parameters, i.e., $\Phi_B = 0.58$ eV for Ti/Al/Ti and $\Phi_B = 0.63$ eV for Ta/Al/Ta. Moreover, the carrier concentration was $N_D=1.25\times10^{19}$ cm^{-3} for both contacts. This value is much higher than the nominal doping level of the AlGaN layer. This results can be explained by the fact that in AlGaN/GaN heterostructures a high carrier density is present in the 2DEG.

A structural analysis of the reacted layers was carried out by means of cross sectional TEM and STEM analysis. Fig 4.12 shows TEM (Fig. 4.12 (a) and 4.11 (b)) and STEM (Fig. 4.12 (c) and 4.12 (d)) images of the two samples annealed at 600°C. Clearly, a strong interaction between the metal layers of the stack occurred after annealing processes. In particular, a modification of the region close to the AlGaN is visible, as two different interface structures are observed in the samples. In the Ti/Al/Ti contact the formation of a continuous TiN layer, few nanometers thick, is visible at the interface with the AlGaN. On the top of this interfacial layer, the presence of an Al-Ti layer is detected, which is consistent with the XRD observation demonstrating the presence of Al_3Ti. The rest of the film closer to the surface region is composed of pure Al (Fig. 4.12 (b) and 4.12 (d)). On the other hand, in the Ta/Al/Ta sample, TEM analysis detected large Al_3Ta grains coexisting with pure unreacted Al. The Al_3Ta grains can be very large, often covering the entire metal thickness from the surface to the interface with the AlGaN. On the top, a Ta layer is still present (see Fig. 4.12 (a) and 4.12 (c)).

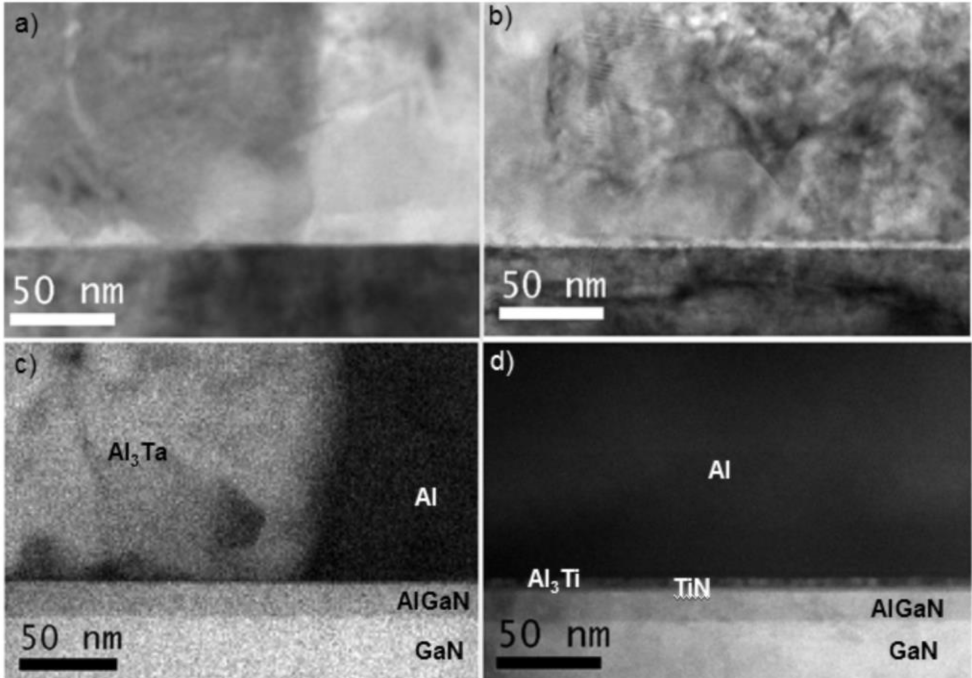

Fig 4.12. Cross section TEM images of Ta/Al/Ta (a) and Ti/Al/Ti (b) contacts and STEM images of Ta/Al/Ta (c) and Ti/Al/Ti (d) annealed at 600°C.

The TiN formation has been detected and reported in many works in literature on Ti-based contacts on GaN materials [83,84,85,86]. In fact, annealing of Ti/GaN (or Ti/AlGaN) systems can lead to a reaction with the TiN formation at the interface. Under these conditions, nitrogen vacancies are released from the material below the metal contact, which act as donors, increasing the net carrier concentration near the interface. Hence, TiN formation can be a key factor for the Ohmic behavior in our annealed Ti/Al/Ti stack.

The formation of an interfacial TaN layer was not observed in the case of Ta-based contacts. These contacts required a longer annealing time to reach the Ohmic behavior and exhibited a higher ρ_c. The reaction of Ti with respect to Ta is facilitated by the larger negative heat of formation of TiN (-336 kJ/mol) with respect to TaN (-247 kJ/mol) [54]. Then, it can be argued that the different interfacial microstructure is responsible for the different values of Φ_B determined by the temperature dependence of ρ_c.

4.4 Effects of layer thickness and annealing time on Ti- based contacts

A preliminary study to understand the role of the metal thickness and annealing time has been conducted on the Ti/Al/Ti contacts, which exhibited the best electrical properties. These samples have been annealed at 600°C for 180s so that the contact morphology was practically unchanged with respect to the sample annealed for 60s. In fact, also in this case, flat areas with some isolated hillocks are visible in the AFM images, leading RMS of 79 nm (almost coincident with the RMS of Ti- based contacts annealed for 60s).

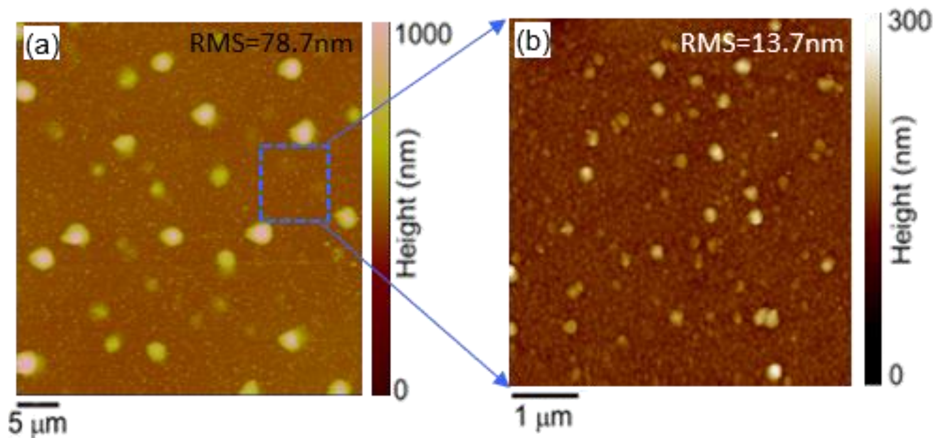

Fig 4.13. AFM images of Ti/Al/Ti contact on 40µm ×40µm (a) and 5µm ×5µm (b) scan areas after annealing at 600 °C for 180s.

Looking at the 5µm × 5µm region (Fig. 4.13 (a)) Ti/Al/Ti contacts annealed for 180s exhibited a lower roughness (RMS=13.7 nm) with respect to the Ti/Al/Ti samples (RMS=18.5 nm) annealed for 60s.
Fig. 4.14 shows the I-V curves acquired between TLM pads at a distance of 20 µm on Ti/Al/Ti contacts (T_{ann}=600°C, t_{ann}=60s and t_{ann}=180s). As can be seen, a further increase of the current occurs in Ti/Al/Ti annealed for a longer time, corresponding to a decrease of the specific contact resistance down to $\rho_{c\,(Ti/Al/Ti\ 180s)} = (7.0\pm0.3)\times10^{-5}\ \Omega.cm^2$.

In spite of this electrical difference, XRD analysis, not reported here, did not show significant structural changes with respect to the Ti/Al/Ti sample annealed for 60, i.e Al_3Ti phase and unreacted Al.

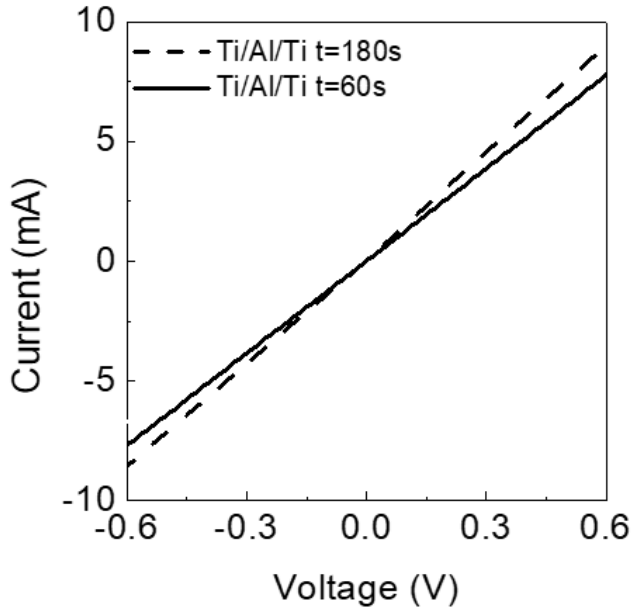

Fig. 4.14. I-V curves acquired on TLM pads placed at a distance of 20 μm in Ti/Al/Ti (T_{ann}=600°C, t_{ann}=60s and t_{ann}=180s).

Temperature dependent TLM measurements have been performed between 25°C and 175°C. Figure 4.15 shows the values of ρ_c as a function of the measurement temperature T . Also in this case, TFE was the current transport mechanism that better fits the experimental ρ_c data. From the fit, an additional lowering of the Schottky barrier height was detected, i.e., Φ_B = 0.52 eV. Then, it is clear that the increase of annealing time leads to an improvement of the electrical response of the Ti/Al/Ti contacts. However, XRD and AFM analysis did not detect differences with the contacts annealed for 60s. However, the increase of the annealing time leads to a stabilization of the contact/AlGaN interface resulting in a lowering of the barrier height and specific contact resistance.

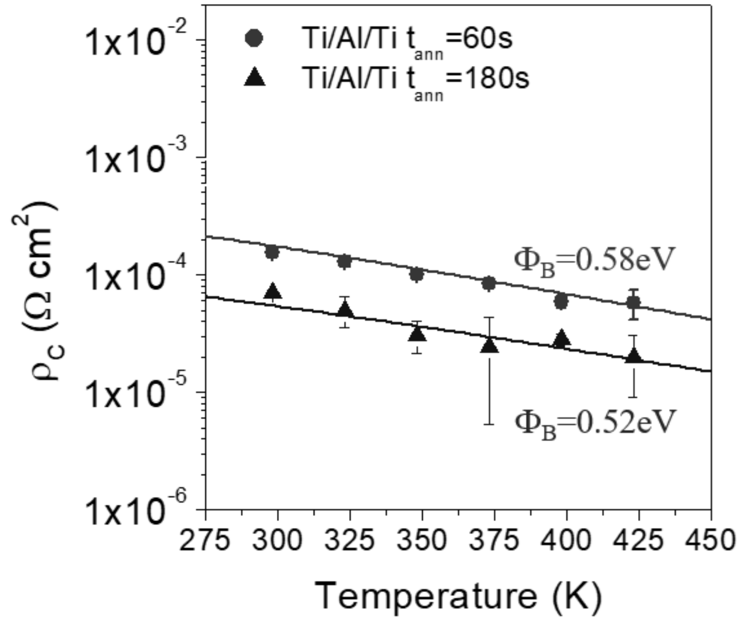

Fig 4.15. Comparison of the temperature dependence of ρ_C for the Ti/Al/Ti contacts annealed at 600°C for 60s and for 180s. The continuous lines represents the fit of the experimental data with TFE model.

As mentioned at the beginning of this chapter, several parameters influence the behavior of a contact, such as metal thickness, thermal annealing temperature, surface treatments etc. [64,87]. In particular, the metal thickness ratio plays an important role on the electrical performance, since different metal thickness can lead to different phases formation during annealing. This aspect, however, is still not well understood and is object of discussion.

This aspect was preliminary investigated by monitoring the behavior of a contact with a 4 times thicker Ti layer at the interface, i.e., $Ti_{(40nm)}/Al_{(300nm)}/Ti_{(20nm)}$. This contact shows an ohmic behavior after annealing at 600°C for 180s. Fig. 4.16 shows the comparison between morphology of the Ti- based contacts ($Ti_{(10nm)}/Al_{(300nm)}/Ti_{(20nm)}$ T_{ann}=600C t_{ann}=60s and $Ti_{(40nm)}/Al_{(300nm)}/Ti_{(20nm)}$ T_{ann}=600C t_{ann}=180s) with the different thickens Ti layers.

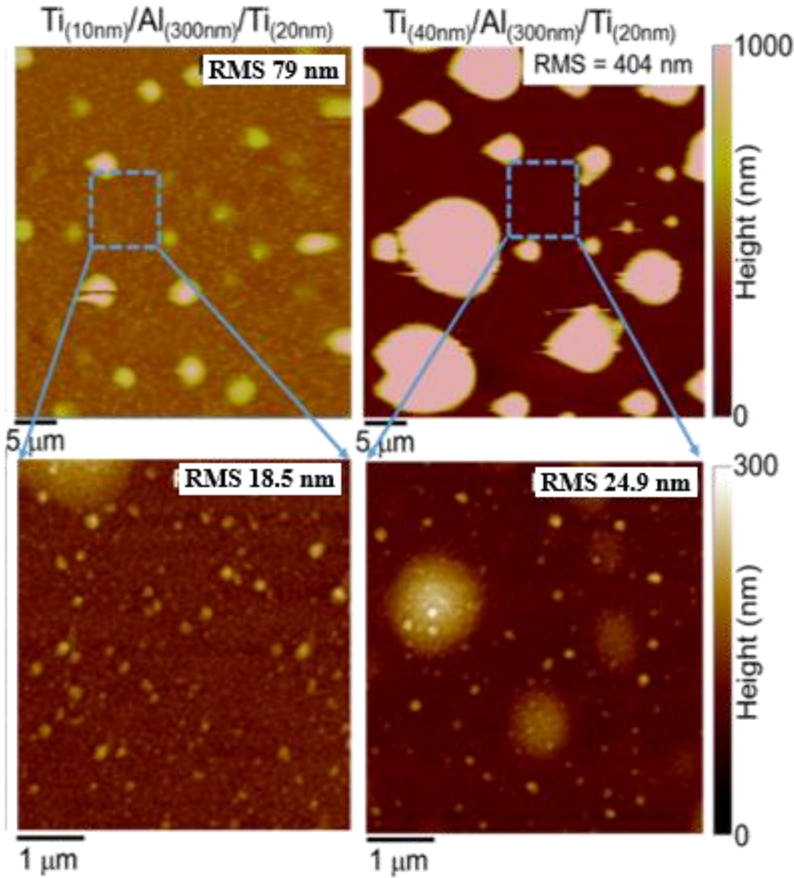

Fig 4.16: AFM images of $Ti_{(10nm)}/Al_{(300nm)}/Ti_{(20nm)}$ contact on 40µm ×40µm (a) and 5µm ×5µm (c) scan areas and AFM images of $Ti_{(40nm)}/Al_{(300nm)}/Ti_{(20nm)}$ contact on 40µm ×40µm (b) and 5µm ×5µm (d) scan areas, after annealing at 600 °C and a time of 60s and 180s respectively.

As can be seen, the surface of the $Ti_{(40nm)}/Al_{(300nm)}/Ti_{(20nm)}$ exhibited much larger hillocks than the $Ti_{(10nm)}/Al_{(300nm)}/Ti_{(20nm)}$ sample, thus resulting into a higher value of roughness (RMS=404nm). The RMS of the $Ti_{(40nm)}/Al_{(300nm)}/Ti_{(20nm)}$ was higher than that of the $Ti_{(10nm)}/Al_{(300nm)}/Ti_{(20nm)}$ also when determined on the flatter regions (i.e., outside the hillocks).

On these contacts, I-V curves shown in Fig. 4.16 have been acquired between adjacent TLM pads at a distance of 20 µm. As can be seen, a significant lower value of current is measured in the contact with thicker Ti

layer. In fact, the TLM analysis revealed a much higher value of specific contact resistance $\rho_{c\ (Ti40/Al/Ti)} = (2.2\pm0.9)\times10^{-3}\ \Omega.cm^2$.

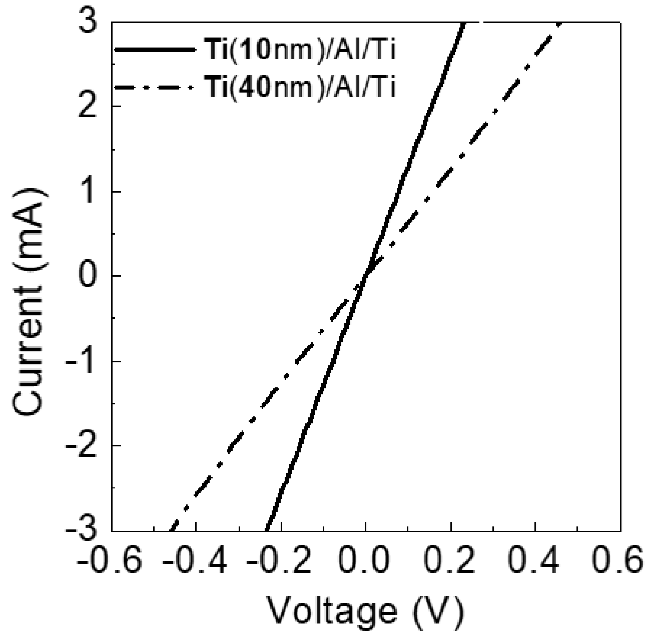

Fig. 4.17. I-V curves acquired on pads of TLM structures placed at a distance of 20 μm in $Ti_{(10nm)}/Al_{(300nm)}/Ti_{(20nm)}$ and $Ti_{(40nm)}/Al_{(300nm)}/Ti_{(20nm)}$ annealed at 600°C and a time of 60s and 180s respectively.

Figure 4.18 shows the temperature dependence of ρ_c for the $Ti_{(40nm)}/Al_{(300nm)}/Ti_{(20nm)}$ contact. For comparison, the results obtained in the $Ti_{(10nm)}/Al_{(300nm)}/Ti_{(20nm)}$ sample are also reported . In this case, from the fit of the experimental data, a Schottky barrier height of $\Phi_B = 0.66$ eV could be determined for the $Ti_{(40nm)}/Al_{(300nm)}/Ti_{(20nm)}$ sample, higher than the value ($\Phi_B = 0.58$ eV) determined in the $Ti_{(10nm)}/Al_{(300nm)}/Ti_{(20nm)}$) sample.
Then, the use of a thicker Ti layer in contact with the AlGaN/GaN heterostructures showed a worsening of the contact performance resulting in a higher specific contact resistance and Schottky barrier value. Moreover, in this case the reaction within the metal layer exhibit a higher surface roughness.

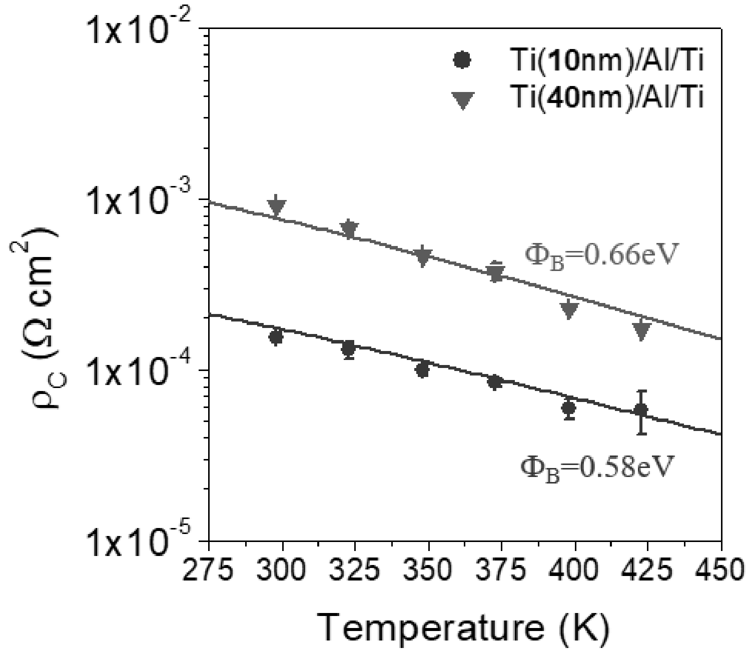

Fig 4.18. Specific contact resistance ρ_C as a function of the measurement temperature T for the $Ti_{10nm}/Al_{300nm}/Ti_{20nm}$ and $Ti_{40nm}/Al_{300nm}/Ti_{20nm}$ annealed at 600°C and a time of 60s and 180s respectively. The continuous lines are the fits of the experimental data with TFE model.

4.5 Modification of the sheet resistance under Ohmic contacts on AlGaN/GaN heterostructures

As explained in chapter 2, the most common method to determine the specific contact resistance in Ohmic contacts is the TLM method. This method is based on the assumption that the sheet resistance of the semiconductor, R_{SH} (Ω/□), is identical to the value assumed under the contacts, R_{SK} (Ω/□) [88]. However, in the presence of thermal induced reactions between the metal stacks and the AlGaN (as those described in the previous sections), this assumption may not be valid, and the sheet resistance under the contact can be different from its value outside the contact ($R_{SK} \neq R_{SH}$) as can be seen in Fig. 4.19.

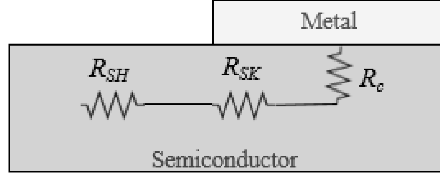

Fig. 4.19. Schematic representation of the case $R_{SK} \neq R_{SH}$. .

As a matter of fact, changes of the electrical properties of n-type GaN below the contacts have been already deduced by temperature dependent electrical measurements in Ohmic contacts [89]. To determine the value of the sheet resistance under the contact R_{SK}, the standard TLM method can be corrected, by measuring the *end contact resistance* (R_E), that is, the resistance due to the voltage drop at the end of the contact [90].

In this thesis, we have performed this kind of measurement in order to estimate possible changes of the sheet resistance under the contact. For this purpose, $Ti_{(15nm)}/Al_{(200nm)}/Ni_{(50nm)}/Au_{(50nm)}$ Ohmic contacts, formed with an annealing at 800°C in Ar, have been chosen as a reference for testing this methodology. Fig. 4.20 (a) shows a representative I-V characteristics measured on TLM patterns between adjacent contacts. The experimental values of the total resistance R_T, determined from these curves at each distance d, are reported in Fig. 4.20 (b). From a linear fit of the data, it was possible to extract the values of $R_C = 5.7 \pm 0.2\ \Omega$, $L_T = 2.1 \pm 0.1\ \mu m$ and $R_{SH} = 535.5 \pm 12.1\ \Omega/\square$. The specific contact resistance determined from this analysis was $\rho_C = (2.4 \pm 0.2) \times 10^{-5}\ \Omega \cdot cm^2$.
The estimation of the sheet resistance under the contact, $R_{SK,}$ can be done, by the modified TLM method proposed by Reeves et al. [88]. First, metal sheet resistance was measured by four points probe measurements. Its value (1.93 $\Omega/\square$) is low enough to apply the model.

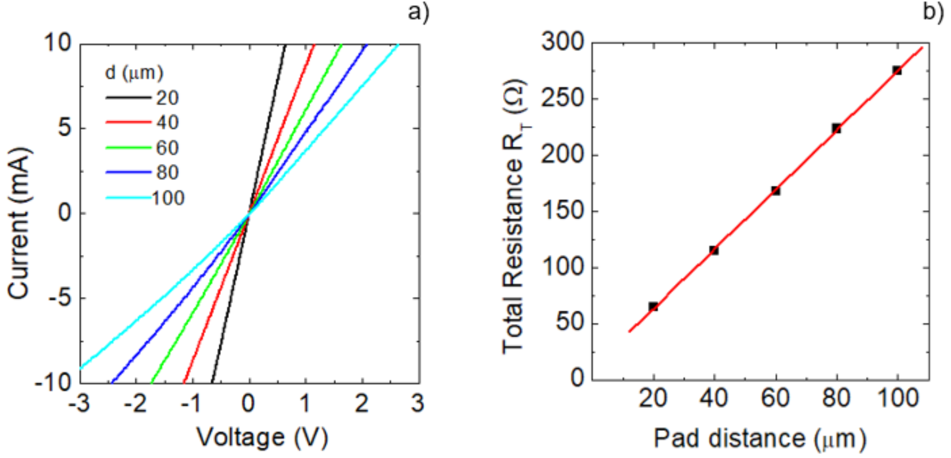

Fig 4.20. (a) I-V characteristics acquired on TLM patterns of Ti/Al/Ni/Au contacts formed with an annealing at 800°C; (b) Plot of the total resistance R_T as a function of pad distance *d*, used to determine the electrical parameters.

Considering that R_{SK} can be different from its value outside the contact ($R_{SK} \neq R_{SH}$), the expression of the total resistance R_T measured between two adjacent TLM pads (Eq. (48)) is modified as [88]

$$R_T = 2\frac{R_{SK}L_{TK}}{W} + \frac{R_{SH}}{W}d \tag{71}$$

and the expression of the contact resistance becomes [88]

$$R_c = \frac{\sqrt{R_{SK}\rho_{ck}}}{W}\coth(L/L_{TK}) \tag{72}$$

where L_{TK} is the corrected transfer length value

$$L_{TK} = \sqrt{\rho_{ck}/R_{SK}} \tag{73}$$

and ρ_{CK} is the corrected specific contact resistance, which take into account the modification of the semiconductor under the contact.

To determine R_{SK}, an additional measurement of the *end contact resistance* (R_E) is necessary [45], where R_E can be considered as the resistance due to the voltage drop at the end of the contact length. The standard procedure used to measure this parameter is to force a constant current (*I*) between two adjacent TLM pads and to measure the potential (*V*) between one of these pads and an opposite outside TLM pad. Then, R_E, given by the ratio *V/I*, can be expressed as :

$$R_E = \frac{\sqrt{R_{SK}\rho_{ck}}}{W}\frac{1}{sinh(L/L_{TK})} \quad (74)$$

Combining the Eqs. (73-75) gives:

$$\frac{R_c}{R_E} = cosh(L/L_{TK}) \quad (75)$$

Hence, from the measure of R_E it is possible to determine the correct value of the transfer length L_{TK} using Eq. (76). Then, the value of R_{SK} can be estimated from:

$$R_{SK} = \frac{R_{SH}L_T}{L_{TK}} \quad (76)$$

However, measuring R_E from the voltage drop at the end of the contact is difficult, due to the extremely low values of voltage drop. Hence, Reeves *et al.* [88] demonstrated an equivalent procedure to determine R_E, using standard I-V measurements carried out on a "three terminals test-pattern", as schematically depicted in the inset of Fig. 4.20. From the resistance measurements between the adjacent contacts 1-2 and 2-3 (R_1 and R_2) placed at a distance *d*, and between the two external ones 1-3 (R_3), it is possible extract the end contact resistance R_E as [88]:

$$R_E = \frac{1}{2} = (R_1 + R_2 - R_3) \quad (77)$$

Fig. 4.21 shows the I-V characteristics acquired in the three terminals test-pattern. In our case, from the values of the three resistances it was possible to extract values of R_E=1.2 ± 0.6 Ω and L_{TK} = 44.6 ± 10.2 µm. Then, by applying Eqs. (73-77) the sheet resistance under the contact R_{SK}= 26.1 ± 5.0 Ω/□ was determined. This value is much lower than the value of the sheet resistance measured outside the contacts (R_{SH} = 535 ± 12 Ω/□) by the standard TLM analysis. This result is typically correlated with the structural modification of the semiconductor below the contact [86,91,92, 93]. However also other parameters, as the specific contact resistance or the resistivity of the metal can have an influence on the value of R_{SK} [94].

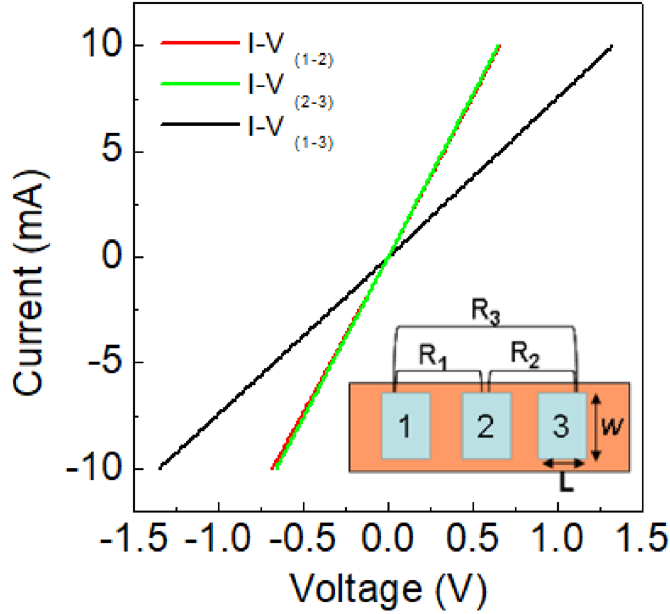

Fig 4.21. I-V characteristics acquired on a three terminals test pattern (schematically shown in the inset) for the determination of the *end contact resistance* R_E. The value of R_E can be extracted as $R_E = \frac{1}{2}(R_1 + R_2 - R_3)$.

Then, it is also possible to correct the specific contact resistance ρ_{CK} as:

$$\rho_{ck} = R_E W L_{TK} sinh(L/L_{TK}) \quad (78)$$

In our case, the corrected value of ρ_{CK}=(5.0 ± 1.2) × 10^{-4} Ω·cm^2 is about 20 times higher than the value obtained by standard TLM method ρ_C =(2.4 ± 0.2) × 10^{-5} Ω·cm^2 . Evidently, ρ_{CK} is correlated to the calculated sheet resistance under the contact R_{SK}, as the ratio ρ_{CK}/ρ_C is proportional to R_{SH}/R_{SK}.

To explain the modification of the semiconductor sheet resistance under the contact, morphological and structural analyses of the annealed Ti/Al/Ni/Au contact have been carried out. Fig. 4.22 shows an AFM image acquired on a 10 × 10 μm^2 area on the contact surface, showing the presence of grains/hillocks, which indicate the occurrence of a thermal reaction between the metal layers.

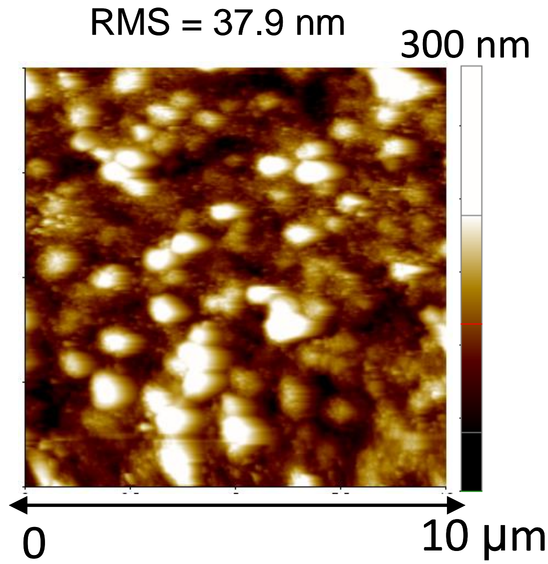

Fig 4.22. AFM image (10×10 □m²) of the surface of a Ti/Al/Ni/Au Ohmic contact formed with an annealing at 800°C.

Then, XRD and TEM analyses have been performed to inspect the microstructure of the reacted metal stack and the interface with the AlGaN.

The XRD patterns (Fig. 4.23 (a)) show several peaks, associated with the formation of new phases, mainly Al_2Au and AlNi, with the presence of a Au_2Ti minor phase and some unreacted Au.

The formation of Al-Au phases is believed, on one side, to provide preferential conduction paths for the current and, on the other side, to be responsible for the rough surface morphology of this kind of contacts [34,88]. Cross section TEM micrograph (Fig. 4.23 (b)), combined with EFTEM mapping, revealed a significant intermixing of the metal layers. In particular, the Al-Ni phase has been mainly observed in the uppermost part of the reacted layer, while a considerable Au in-diffusion towards the AlGaN has taken place, as can be deduced by the presence of Al-Au phases. Close to the interface, a non-uniform layer containing Au has been identified, together with the presence of Ti and N. Hence, TiN has formed during the annealing process, and it is visible in the TEM image as darker grains near the interface. Plausibly, the decrease of the sheet resistance observed under the contact R_{SK}, can be correlated to the electrical modification of the interface induced by the TiN formation.

The decrease of the sheet resistance under our Ti/Al/Ni/Au Ohmic contact qualitatively resembles the results obtained by Hajasz *et al.*[86] on the Au-free Ti/Al system. However, they measured a decrease of R_{SK} by a factor of 2.13 with respect to R_{SH}, i.e., much lower than in our case (R_{SH}/R_{SK}=20.5). Such difference suggests that the modification of R_{SK} in AlGaN/GaN heterostructures can depend on several parameters, such as the contact resistance or the resistivity of the metal [94,95], or even the geometry of the TLM pads.

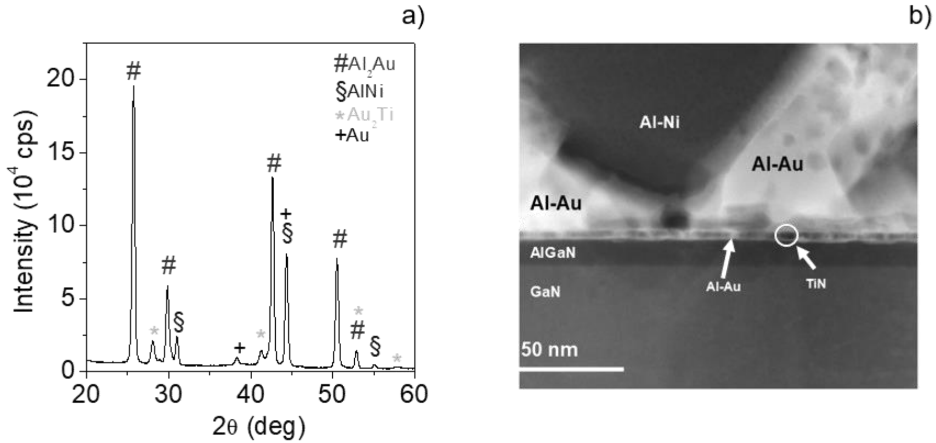

Fig 4.23. (a) XRD pattern of a Ti/Al/Ni/Au contact formed with an annealing at 800°C; (b) Cross section TEM image of the same contact, showing the reacted metal layer and the underlying AlGaN/GaN heterostructure.

The end contact resistance method has been used to determine R_{SK} and ρ_C in systems with different metallizations (Ti/Al/Ti, Ta/Al/Ta, TiAlW) annealed at different temperatures on the same AlGaN/GaN heterostructure. Interestingly, the value of ρ_{CK} could be correlated to the calculated R_{SK}, as the ratio ρ_{CK}/ρ_C is proportional to R_{SH}/R_{SK}. In Fig. 4.24, the calculated values of ρ_C are reported as a function of R_{SK} for these systems. The results show a correlation between R_{SK} and ρ_C. In particular, for low values of ρ_C (up to ~ 10^{-3} Ωcm^2) R_{SK} results to be lower than $R_{SH,}$ whereas higher values of ρ_C result in $R_{SK} > R_{SH}$. The trend shown in Fig. 4.24 is in agreement with the results obtained by Henry et al. [92] on GaAs structures. Further investigations on the structural changes of the different metallization schemes could help to explain the observed behaviour.

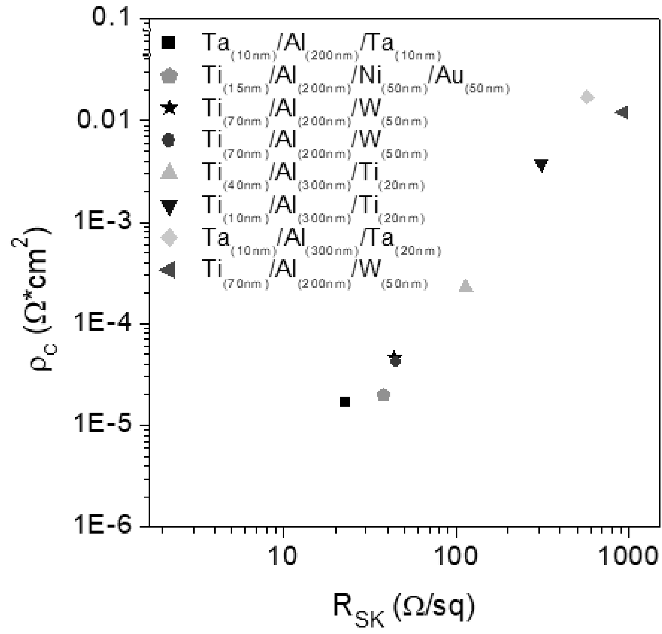

Fig. 4.24 Values of ρ_C as a function of R_{SK} for different metallization schemes on the same AlGaN/GaN heterostructures.

Chapter 5 – Ohmic contacts on Silicon Carbide materials

As anticipated in the first chapter, among the SiC polytypes, the hexagonal 4H-SiC is today the most mature for power electronics applications. However, some fundamental questions are strongly debated to improve the device technology. In particular, the fabrication of Ohmic contacts on 4H-SiC that is crucial in Junction Barrier Schottky (JBS) diodes and metal oxide semiconductor field effect transistors (MOSFETs), remains a difficult task. On the other hand, the cubic 3C-SiC is still in its infancy. In fact, although it has been studied for long time, its crystalline quality has not reached an adequate level for the fabrication of reliable electronics devices. Hence, understanding the mechanism of Ohmic contact formation on 3C-SiC is an interesting topic.

This chapter reports the experimental results achieved in this thesis on Ohmic contacts to SiC materials. In the first part, the realization of Ohmic contacts on p-type implanted 4H-SiC is described. In particular, as the specific contact resistance is strongly influenced from the semiconductor doping, the electrical activation of the p-type implanted dopant (aluminium) was first studied for different annealing conditions by means of Hall effect measurements. On the implanted layers, Ti/Al-based Ohmic contacts have been fabricated and characterized. The second part is dedicated to the study of Ohmic contacts on the cubic polytype 3C-SiC. In this case, both n-type and p-type layers were used for the experiments, comparing different metallizations based on Ni and Ti.

5.1 Ohmic contacts on p-type implanted 4H-SiC

5.1.1. State of the art on implantation doping and Ohmic contacts on p-type 4H-SiC

As mentioned before, Ohmic contacts are fundamental building blocks of many SiC-based devices, linking the signal transfer from the

semiconductor to the external circuit [35]. Such contacts are required in both n-type and p-type doped regions in real devices but their fabrication is difficult on p-type materials. In fact, because of the wide band gap of 4H-SiC, it is not easy to find metals giving a low Schottky barrier on the p-type doped regions. Moreover, the high ionization energy of the p-type dopant makes the tunnelling contacts extremely difficult [35].

Because of the extremely low diffusion coefficients of the dopant species in SiC even at high temperatures [96,97], selective area doping of 4H-SiC during devices fabrication is obtained uniquely through ion implantation. In fact, all the commercially available 4H-SiC power devices, i.e., Schottky diodes, JBS diodes, MOSFETs, are fabricated using ion-implantation to create selectively doped regions or resistive edge terminations [96].

The main dopant species for SiC are Nitrogen (N) and Phosphorous (P) for n-type doping and Aluminum (Al) for p-type doping. High post-implantation annealing temperatures (> 1500°C) are typically required to bring these species in substitutional positions and achieve their electrical activation [98,99,36]. In particular, selectively doped p-type regions are key parts of both JBS and MOSFETs and the control of their electrical properties has a significant impact on several devices parameters (e.g., Ohmic contacts formation, device on-resistance, threshold voltage and channel mobility, etc.). Hence, understanding the dependence of the properties of p-type implanted layers on the activation annealing temperature is very important to set the optimal conditions to create good Ohmic contacts on p-type 4H-SiC. Although several literature investigations reported on the properties of Al-implanted 4H-SiC layers [100,101,102], the large variety of experimental conditions and the evolution of the annealing procedures make this topic always object of scientific discussions.

Hall-effect measurements are often used to study the electrical properties of p-type 4H-SiC layers, in order to determine key parameters like the holes concentration and mobility [37]. A critical issue of this methodology is the choice of the Hall scattering factor r_H for SiC [103,104]. In fact, the difficulty to extract the mobility and the free hole concentration from Hall measurements is related to the correct knowledge of r_H. Many authors often interpret the experimental Hall results on p-type 4H-SiC assuming $r_H=1$, which, in turn, leads to an overestimation of the doping level in the material

[101,105]. Only few works specifically reported experimental calculations of r_H for SiC [106,107], whose findings should be considered for a correct analysis of the currently available data. The activation of the p-type Al-dopant has been investigated by means of Van der Pauw and Hall Effect measurements, taking into account the concentration dependence of r_H [106,107]. This study was preparatory for the study of the electrical properties of Ohmic contacts fabricated on these layers, described in section 5.1.3.

As mentioned before, the formation of Ohmic contacts on p-type 4H-SiC is a challenge for 4H-SiC technology, due to the wide band gap of the material and the high ionization energy of the acceptors [35,108]. Nickel is the metal generally employed to fabricate Ohmic contact to n-type 4H-SiC. The Ohmic behaviour is related to nickel silicide formation upon annealing at temperatures higher than 900°C [109]. In the case of p-type 4H-SiC, Ohmic contacts, achieved with Ti- based metallization, have been considered [110][111]. In fact, with such metallization, Ti forms new phases by reacting with SiC that are able to reduce the barrier height for holes upon thermal processes [112]. Generally, Al is used over Ti to prevent oxidation through the formation of Ti-Al phases and the temperature required to show an Ohmic behaviour are usually high, over 800°C. Finally, many solutions have been reported as cap layer (e.g., Si, W or Ni [108,113,114]) to improve the reproducibility of the contact, obtaining different microstructure and electrical properties after annealing. These literature results reveal the importance of Ti-Si, Ni-Si and Ti-Al phases. Hence, the use of Ti/Al/Ni stack can be very promising. Despite the many steps forward that have been made, Ohmic contact formation is still an open issue, mostly about the improvement of the stability of the metallization within thesystem operating under high temperatures.

5.1.2 Electrical activation of the p-type dopant after high temperature annealing

N-type doped 4H-SiC (0001) epitaxial layers grown onto heavily doped substrates with a nominal doping concentration of $N_{D\text{-}epi}=1\times10^{16}$ at/cm^3 were used. The samples were implanted in STMicroelectronics at 500°C

with Al-ions at different energies (30-200 keV) and doses of 3×10^{14} – 1×10^{15} at/cm^2 in order to obtain an almost flat (box-like) profile with a thickness t_{imp} = 300 nm and a concentration of 1×10^{20} at/cm^3. After implantation, the samples were annealed at three different temperatures (1675°C for 30 minutes, 1775°C and 1825°C for 15 minutes).
It is known that the thermal budgets necessary for the electrical activation of implanted dopants strongly modify the surface morphology of SiC [101]. In fact, at high temperatures (~ 1500 °C) Si from the surface starts to evaporate, leading to a roughening of the surface. Hence, during annealing, the sample surface was protected by a graphite-capping layer, formed by an appropriate thermal backing of photoresist [115].
Fig. 5.1 shows the AFM images of p-type implanted 4H-SiC samples, subjected to three different annealing temperatures.

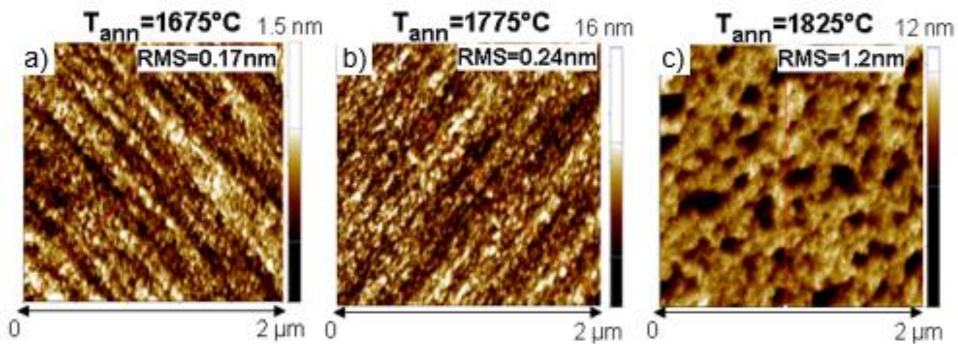

Fig. 5.1. AFM images of p-type implanted 4H-SiC layers after activation annealing at different temperatures T_{ann}: (a) 1675°C, (b) 1775°C and (c) 1825°C.

The root mean square (RMS) roughness of the sample annealed at 1675°C is 0.17 nm and increases with increasing the annealing temperature (e.g., RMS=0.24 nm at 1775°C) until a certain deterioration of the surface morphology is observed after annealing at 1825°C (RMS=1.2 nm). In this latter case, the sample surface is characterized by the presence of holes that reach a depth of about 8-10 nm and a diameter of about 200 nm. The implanted layers have been electrically characterized by means of Van der Pauw and Hall-effect measurements. The Hall structures were fabricated by defining isolated p-type implanted square structures and contacting their four corners by Ti (70nm)/Al (200nm) Ohmic contacts annealed at 950°C

(see section 3.3). First, the current-voltage (I-V) curves (Fig. 5.2 (a)) have been acquired on the Van der Pauw structures fabricated on the three samples (inset of Fig. 5.2 (a)), which allowed the determination of the sheet resistance of the implanted layer (R_{SH}) as described in section 3.1.2 (see Eq. 56). The slope of the I-V curves increases with increasing the annealing temperature, due to the decrease of R_{SH}. The following values of R_{SH} of the p-type implanted 4H-SiC were found at the different post-implantation annealing temperatures T_{ann}: 12.0 kΩ/sq (T_{ann}=1675°C), 9.75 kΩ/sq (T_{ann}=1775°C) and 7.47 kΩ/sq (T_{ann}=1825°C).

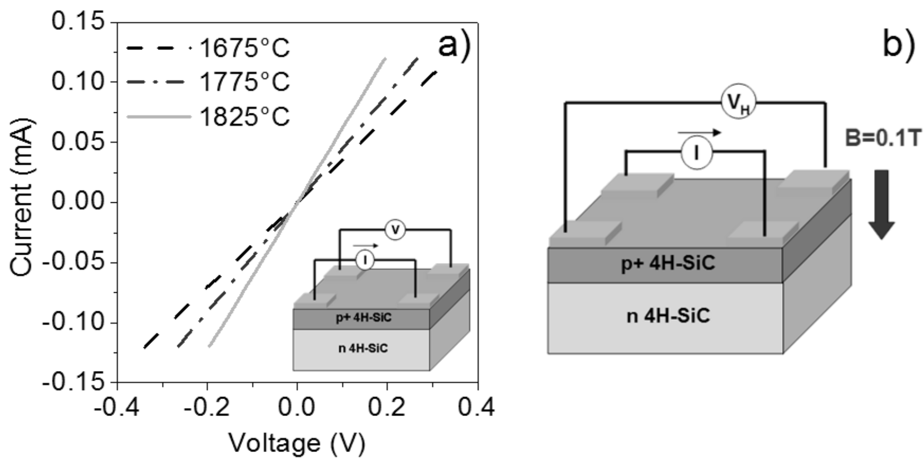

Fig. 5.2. (a) I-V curves acquired on Van der Pauw structures (inset) fabricated on p-type implanted 4H-SiC samples annealed at three different temperatures: 1675°C, 1775°C and 1825°C. (b) Schematic of the Hall effect measurement.

Useful information on the mechanism of activation of the implanted dopant can be obtained from the dependence of the resistivity on the annealing temperature. By assuming a uniform doping concentration in the entire implanted layer thickness t_{imp}, it was possible to quantify the decrease of the resistivity of the p-type 4H-SiC upon annealing, i.e., from ρ_c = 0.36 Ωcm (1675°C) down to ρ_c = 0.22 Ωcm (1825°C). The obtained data are reported in Table 5.1. Fig. 5.3 reports an Arrhenius plot of the sheet resistance of the Al-implanted 4H-SiC layers as a function of the annealing temperature. This plot allows estimating the activation energy of the dopant, i.e., the energy needed from the implanted Al atoms to contribute as acceptors to the p-type doping of the 4H-SiC layer. From the linear fit

of the data an activation energy of about 1eV has been determined. For comparison, other literature data referring to 4H-SiC layers implanted with a similar Al content ($1\text{-}3\times10^{20}cm^{-3}$) are reported [36]. Almost the same activation energy has been extracted, meaning that the mechanism of electrical activation of Al for high concentrations (i.e., in the order of $10^{20}cm^{-3}$) is the same in the two cases. *Giannazzo et al.* [116] found a value of 6.3 eV for Al electrical activation. However, in that work, Al was implanted at room temperature (not at 500°C as in our case), while the post-implantation annealing temperatures ranged from 1550 to 1650 °C (much lower than in our case). These differences explain the strong discrepancy in the activation energy values.

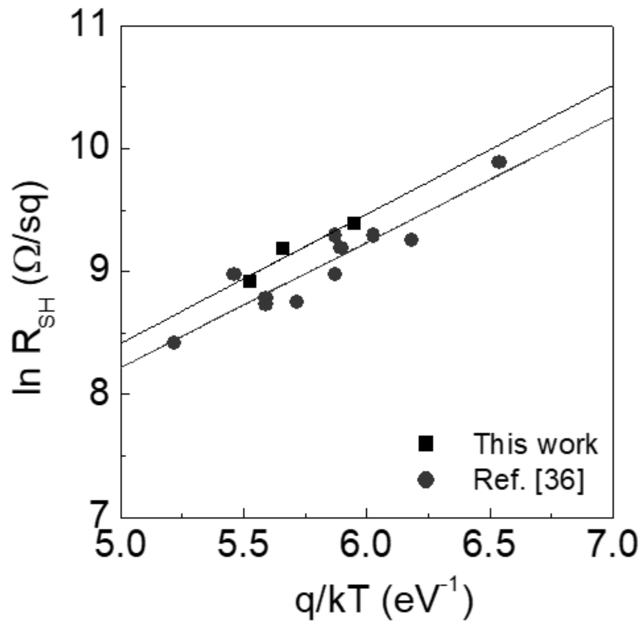

Fig. 5.3: Arrhenius plot of the sheet resistance of the Al-implanted 4H-SiC samples as a function of the annealing temperature, giving an activation energy of 1 eV. For comparison, a similar Arrhenius plot for the data reported in Ref. [36] is also reported.

The carrier density and mobility values have been calculated from Hall-effect measurements. The experiments have been carried out by applying a magnetic field of intensity B = 0.1 T perpendicular to the sample surface, as schematically reported in Fig. 5.2 (b). Using Eqs. (65) and (67) the

following values have been extracted: p=1.38×10^{18} cm^{-3} and μ=13 cm^2/Vs (1675°C), p=2.29×10^{18} cm^{-3} and μ=10.7 cm^2/Vs (1775°C), p=2.58×10^{18} cm^{-3} and μ=10.9 cm^2/Vs (1825°C). These values of p and μ at room temperature have been evaluated, in a first approximation, assuming a Hall scattering factor $r_H = 1$.

As mentioned before, the study of the electrical activation and the compensation ratio of the p-type implanted dopant can be performed by meaning of temperature dependent Hall measurements. The hole concentration p as a function of the temperature can be described by the neutrality equation [104]:

$$\frac{p(p+N_D)-n_i^2}{N_A-N_D-p+n_i^2/p} = \frac{N_V}{g} exp\left(-\frac{E_A}{kT}\right) \quad (79)$$

where N_A is the acceptor concentration, N_D is the compensating donor concentration, N_V is the density of states in the valence band, E_A is the activation energy (i.e., the energy level of the acceptors above the valence band) and g is the degeneracy factor of the ground level of the Al-acceptor fixed to 4 [106].

For WBG semiconductors, the intrinsic carrier concentration n_i is extremely low. Hence, the expression of the hole concentration in Eq. (4) can be approximated by [37]:

$$p \approx \frac{1}{2}\left[-N_D - x + \sqrt{(N_D - x)^2 + 4N_A x}\right] \quad (80)$$

where

$$x = \frac{N_V}{g} exp\left(-\frac{E_A}{kT}\right) \quad (81)$$

The hole concentration p is related to the Hall coefficient R_H by the expression [104]:

$$p = \frac{r_H}{qR_H} \quad (82)$$

As mentioned before, the correct determination of the hole concentration p, presents the methodology issues relating to r_H. In fact, by simply assuming $r_H = 1$ typically leads to an overestimation of the carrier density in SiC [37]. To overcome this problem, firstly *Pensl et al.* [106] proposed to derive the Hall scattering factor r_H for p-type epitaxial SiC from the

comparison between the temperature dependence of experimental and theoretical values of p:

$$r_H = \frac{p_{theor}(T)}{p_{exp}(T)} \qquad (83)$$

where p_{exp} (T) is the experimental hole concentration obtained assuming r_H=1 and p_{theor} (T) is the theoretical value calculated from the neutrality Eq. (79) using values of N_A and N_D obtained by independent chemical and electrical analyses [106].

Then, the Hall scattering values should be considered in order to estimate the correct value of carrier concentration. As first approach, the temperature dependent Hall scattering factor r_H reported by *Pensl et al.* [106] was considered to analyse our results, thus resulting into values of N_A larger than the total Al-implanted concentration when fitting the experimental data with the neutrality equation. However, such an overestimation could be related to the fact that the values of r_H reported in Ref. [106] were determined for Al-doping levels of about 1×10^{18} cm^{-3}, i.e., about two orders of magnitude smaller that the Al-implanted concentration of our samples (1×10^{20} cm^{-3}).

More recently, *Asada et al.* [107] derived the Hall scattering factor r_H for a wider range of Al-concentration in 4H-SiC epilayers.. Hence, we considered these results [107] to correct our experimental data for all the measurement temperatures. Namely, the experimental values of the hole concentration $p_{exp.}(T)$, determined by temperature dependent Hall measurements, were corrected using the expression:

$$p_{theor}(T) = p_{exp}(T) \cdot r_H(T) \qquad (84)$$

As an example, Fig. 5.4 shows the values of the hole concentration on the sample annealed at 1675°C assuming r_H=1 (black squares) and after correction (red circles). A significant decrease of the hole concentration occurs after correction, since in the temperature range of our experimental measurements (300-500K) the values of r_H decrease from 0.5 to 0.25 [107].

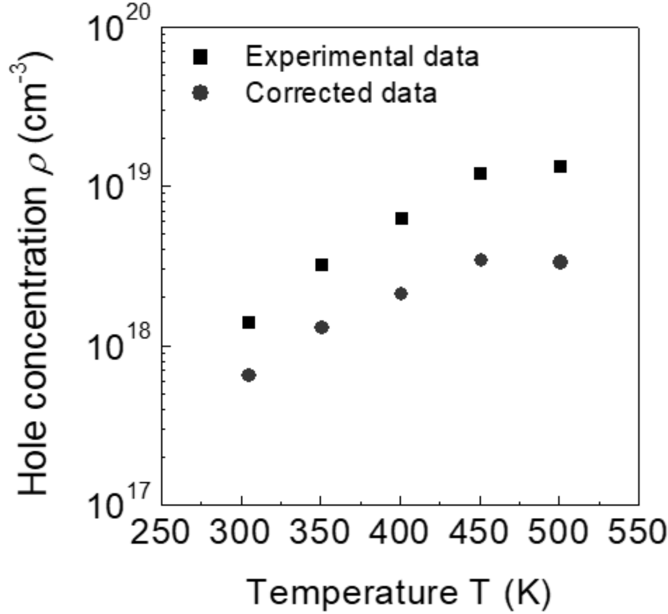

Fig. 5.4. Experimental data (r_H=1) of the hole concentration measured on the Al-implanted 4H-SiC sample annealed at 1675°C (black squares) and data corrected ($r_H \neq 1$) using the r_H factor reported in Ref. [107] (red circles).

The experimental Hall mobility values have been corrected considering the Hall scattering factor. Then, the same correction has been applied for the other samples annealed at 1775°C and 1825°C. Table 5.1 summarizes all the physical parameters calculated by Van der Pauw and Hall effect measurements for the three samples at room temperature.

Annealing Temperature	R_{SH} (Ω/sq)	ρ (Ωcm)	p (cm^{-3})	μ ($cm^2V^{-1}s^{-1}$)
1675°C	12000	0.36	6.49×10^{17}	26.7
1775°C	9750	0.29	9.68×10^{17}	22.1
1825°C	7470	0.22	1.34×10^{18}	20.8

Table 5.1. Summary of the parameters extracted by Van der Pauw and Hall.effect measurements at room temperature on p-type implanted 4H-SiC samples, annealed at three different temperatures T_{ann}: 1675°C, 1775°C and 1825°C.

The Hall mobility values are in the range 21-27 cm^2/Vs for these annealing temperatures, which is in good agreement with the results reported by *Rambach et al.* [102] for similar doping and annealing conditions.
From the temperature dependent Hall effect measurements is possible to determine the acceptor concentration N_A and the compensation N_D, as expressed in the neutrality equation (Eq. (81)). For this calculation, it is necessary to know the ionization energy of the Al acceptors E_A. The temperature dependent sheet resistance $R_{SH}(T)$ of an implanted layer arises from both $\mu(T)$ and carrier concentration $p(T)$,i.e.,:

$$R_{SH}(T) = \frac{1}{q\mu(T)p(T)t_{imp}} \qquad (85)$$

where t_{imp} is the thickness of the implanted layer.
From the neutrality equation (see Eqs. (81) and (82)), it can be deduced that the temperature dependence of the carrier concentration is dominated by an

exponential of the ionization energy of the Al-dopant E_A:

$$p(T) \propto exp\left(-\frac{E_A}{kT}\right) \qquad (86)$$

On the other hand, the carrier mobility shows a much weaker dependence on the measurement temperature [115]. Hence, it is possible to approximate the sheet resistance as:

$$R_{SH}(T) \propto \frac{1}{exp\left(-\frac{E_A}{kT}\right)} \qquad (87)$$

Under this approximation, the value of the ionization energy E_A can be estimated from a linear fit of $\ln(R_{SH})$ as a function of q/kT. As an example, Fig. 5.5 shows this plot for the sample annealed at 1675°C, from which an activation energy E_A=110 meV could be determined.

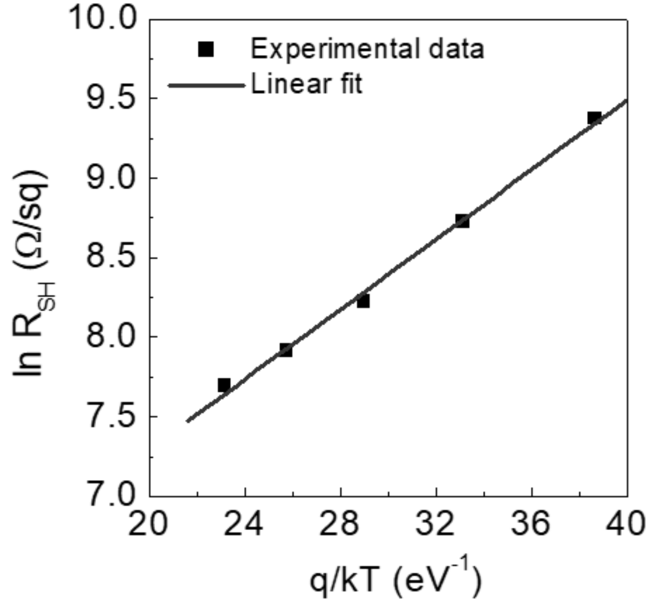

Fig. 5.5. Logarithmic values of R_{SH} as a function of q/kT for the sample annealed at 1675°C. Solid lines represents the linear fit of the experimental data.

Following this method, it was possible to determine the values of E_A for higher annealing temperatures, i.e., E_A=105meV and E_A=99meV for the sample annealed at 1775°C and 1825°C, respectively.
The temperature dependence of the hole concentration for the three samples annealed at 1675°C, 1775°C and 1825°C is shown in Fig. 5.6.

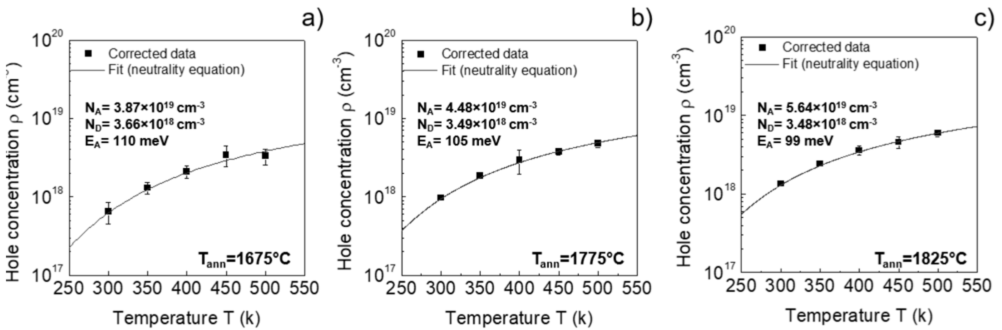

Fig. 5.6. Temperature dependence of the hole concentration for the Al-implanted 4H-SiC samples annealed at T_{ann}=1675°C (a)), T_{ann}=1775°C (b)) and T_{ann}=1825°C (c). The solid line represents the fits of the experimental data with the neutrality equation.

The solid lines represent the fit of the experimental data with the Eq. (87), assuming the values of E_A estimated by the temperature dependence of R_{SH} (as the example in Fig. 5.5) and considering the acceptor concentration N_A and the compensating donor concentration N_D as free parameters. Table 5.2 reports the acceptor and donor concentration values determined from the best-fits procedure, together with the value of the ionization energy E_A. It can be observed that the acceptor concentration increases with increasing the annealing temperature, thus being accompanied by a slight decrease of the compensating donors concentration. The obtained values correspond to an increase of the Al activation from 39% to 56%, with increasing the annealing temperature from 1675°C to 1825°C, consistently with the decrease of the sample resistivity. Similar activation values have been obtained by *Negoro et al.* [98] considering an annealing temperature of 1800°C and similar values of Al implanted concentration and temperature of implantation. However, *Nipoti et al.* [117], reported a higher activation values, of 69%, using a microwave system which reaches an annealing temperature of 2100°C. In our case, the estimated activation percentage can be justified by the lower annealing temperature. In fact, for a value of 1750°C, an activation of 35% has been reported by *Saks et al.* [118]. Moreover, a further improvement of the Al activation (up to close to 100%) was reported by increasing the implantation temperature up to 1000°C [101].

Annealing Temp.	**E_A (meV)**	**N_A (cm^{-3})**	**N_D (cm^{-3})**	**Al activ.**	**Compens.**
1675°C	110	3.87×10^{19}	3.66×10^{18}	39 %	9.4 %
1775°C	105	4.84×10^{19}	3.49×10^{18}	48 %	7.2 %
1825°C	99	5.64×10^{19}	3.48×10^{18}	56 %	6.2 %

Table 5.2. Values of activation energy E_A, acceptor concentration N_A, compensating donor concentration N_D, Al activation and compensation ratio for the Al-implanted 4H-SiC samples annealed at 1675°C, 1775°C and 1825°C.

As could be deduced from our analysis, an Al activation of 56% could be obtained with an annealing at 1825 °C. At his temperature, however, a deterioration of the surface morphology has been observed by AFM (Fig.

5.6 (c)), which in turn may be detrimental in MOSFETs technology where the p-type region is a part of the transistor channel. However, in other cases, such as in the case of JBS or bipolar devices, the need of a high acceptor concentration is required to minimize the specific contact resistance of Ohmic contacts on the implanted regions. In this case, considering that the current transport in metal/p-type 4H-SiC interfaces is typically ruled out by TFE mechanism [119] and assuming a barrier height of 0.56 eV [108], the increase of the acceptor concentration from 3.9×10^{19} cm^{-3} to 5.6×10^{19} cm^{-3} should result in an 82% improvement of ρ_c (i.e., from 1.8×10^{-4} Ωcm^2 to 3.2×10^{-5} Ωcm^2).
Finally, as mentioned before and reported in Table 5.2, the ionization energy E_A decreases with increasing the acceptor concentration N_A. In fact, it is known that E_A is inversely proportional to the average distance between Al atoms, which in turn decreases with the increase of the acceptor density N_A [37].
In general, this dependence of the ionization energy on the acceptor concentration is described by the empirical expression [120]:

$$E_A = E_0 - \alpha \cdot N_A^{1/3} \quad (88)$$

where E_0 is the ionization energy for an isolated impurity centre, and α is a constant.
Fig. 7 reports a plot of E_A as a function of N_A of our experimental data together with other literature works [100,101] on Al-implanted 4H-SiC layers. This collection of data has been fitted with the theoretical behaviour of E_A as function of N_A (Eq. (89)), giving a ionization energy E_0=216 meV and a coefficient $\alpha = 3\times10^{-5}$ meV cm^{-1}. Noteworthy, *Frazzetto et al.*[115] determined an activation energy of 144 meV and a doping level of 2×10^{-19} cm^{-3} by modelling the temperature dependence of the specific contact resistance of Ohmic contacts on p-type implanted 4H-SiC layers using transmission line model (TLM) structures. This data, reported in Fig. 5.7, is also well described by the experimental fit obtained using Eq. (88). This results suggests that an appropriate analysis of temperature dependent TLM measurements can also provide useful information on the electrical activation of Al dopant in 4H-SiC. This point is an open issue for future activities and also other groups in the SiC community are currently working on that [121].

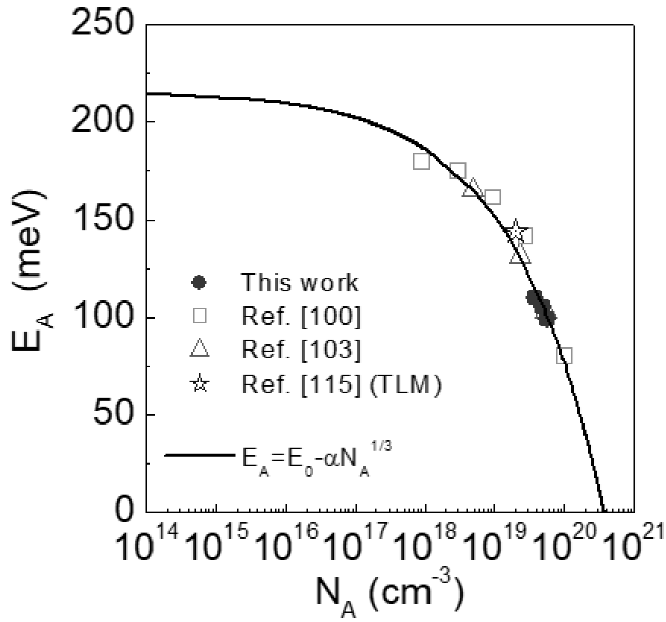

Fig. 5.7. Ionization energy of the acceptors (E_A) in 4H-SiC as a function of the acceptor concentration (N_A) determined by Hall measurements. The experimental data of this work (red circles) are reported together with data from Refs. [100,103,115]. The solid line corresponds to a fit with the empirical expression $E_A=E_0- \alpha N_A^{1/3}$ with $E_0=216$ meV and $\alpha=3\times10^{-5}$ meV cm^{-1}.

In conclusions, our analysis allowed to determine an active Al-doping concentration of 3.87×10^{19} cm^{-3} after annealing at 1675°C, corresponding to an activation of 39%. The electrical activation increased up to 56% at 1825°C. This information can be useful for JBS technology to improve the quality of Ohmic contacts. However, a further optimization of the capping layer process could be required to prevent the RMS increase of Al-implanted 4H-SiC regions upon annealing at such high temperature.

5.1.3 Study of Ti/Al/Ni Ohmic contacts on p-type implanted 4H-SiC

In this section, Ti(70nm)/Al(200nm)/Ni(50nm) contacts have been studied on the p-type implanted 4H-SiC layers described in section 5.1.2. These contacts have been fabricated by sputtering and then annealed at 950°C in Ar atmosphere for 60s (see section 3.3).
Fig. 5.8 (a), (b) and (c) show the AFM images of as deposited Ti/Al/Ni contacts on p-type implanted 4H-SiC samples, subjected to three different implantation annealing temperatures.

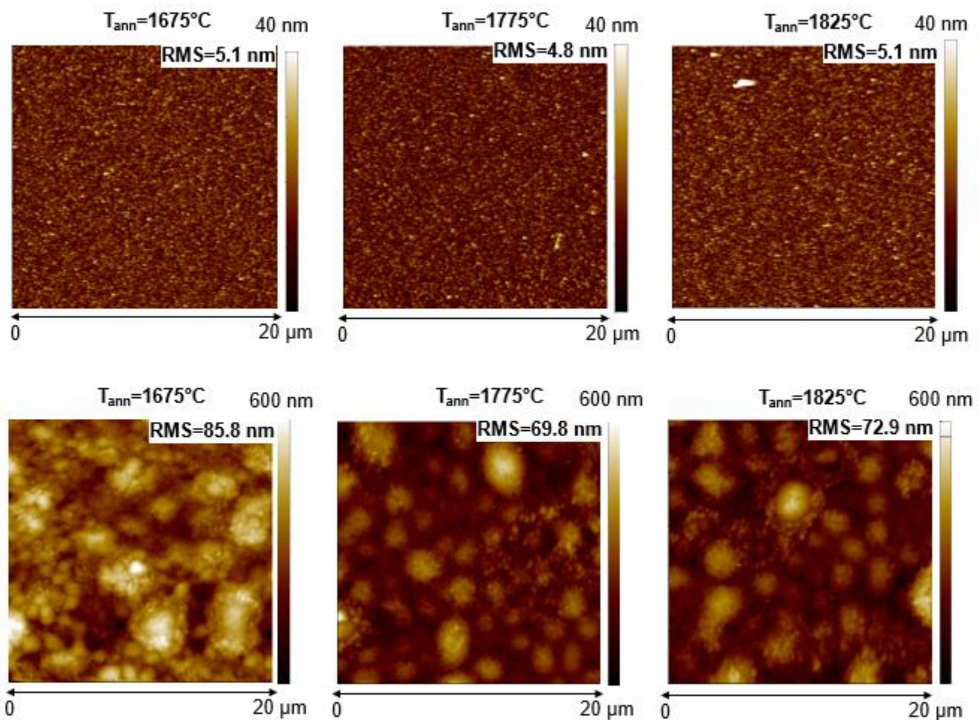

Fig. 5.8 AFM images of the Ti/Al/Ni contacts formed at 950°C on p-type implanted 4H-SiC samples, activated at three different post-implantation annealing temperatures.

The morphologies are very similar and quite smooth. Fig. 5.8 (d), (e) and (f) show the morphologies of the Ti/Al/Ni contacts annealed at 950°C. The root mean square (RMS) roughness of the sample are very similar, resulting

in the values of 85.8 nm at 1675°C, 69.8 nm at 1775°C and 72.9 nm at 1825°C.
The electrical characterization of the contacts has been performed by I-V measurements on TLM structures, with the standard procedure adopted for the other materials. Fig 5.9 shows the comparison of I-V curves acquired between adjacent contacts on TLM structures (distance of 20 μm) at different post-implantation annealing temperatures.
As can be seen, linear characteristics are obtained in all three cases. Moreover, an increase of the current is observed with the increase of the post-implantation annealing temperature.

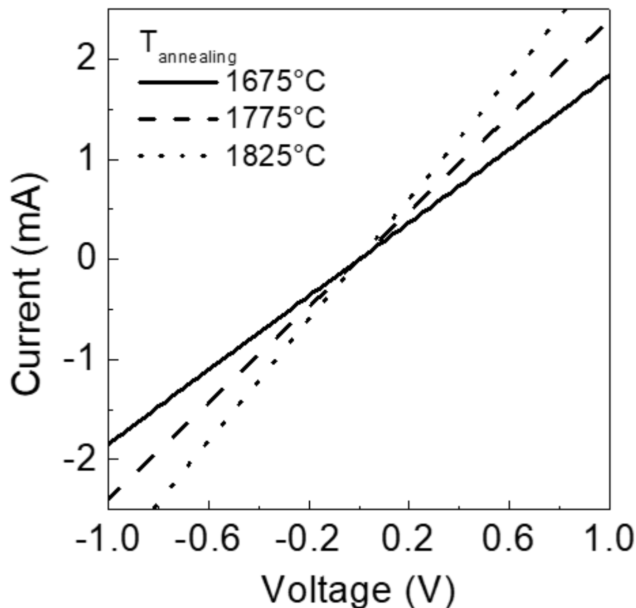

Fig. 5.9. I-V curves acquired between Ti/Al/Ni contacts at a distance of 20 μm on p-type 4H-SiC implanted subjected to different post-implantation annealing temperatures.

The I-V curves acquired in the three samples on the TLM structures with different pad distances are shown in Fig5.10. From the slope of these curves, it was possible to extract the total resistance R_{TOT}. Fig. 5.11 reports the plots of the total resistance R_{TOT} measured as a function of the distance

d between adjacent TLM pads. The different slope of R_{TOT} in the three

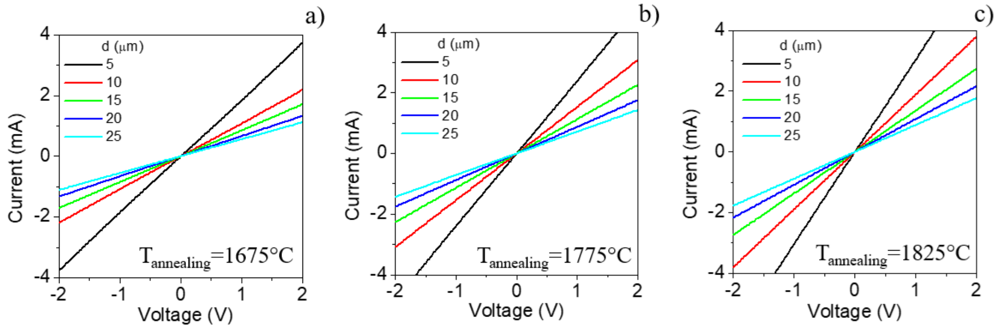

samples is due to the different sheet resistance of the implanted layer.

Fig. 5.10. I-V curves acquired on L-TLM structures at different distances for annealed (950°C) Ti/Al/Ni contacts on Al-implanted 4H-SiC samples annealed at T_{ann}=1675°C (a)), T_{ann}=1775°C (b)) and T_{ann}=1825°C (c).

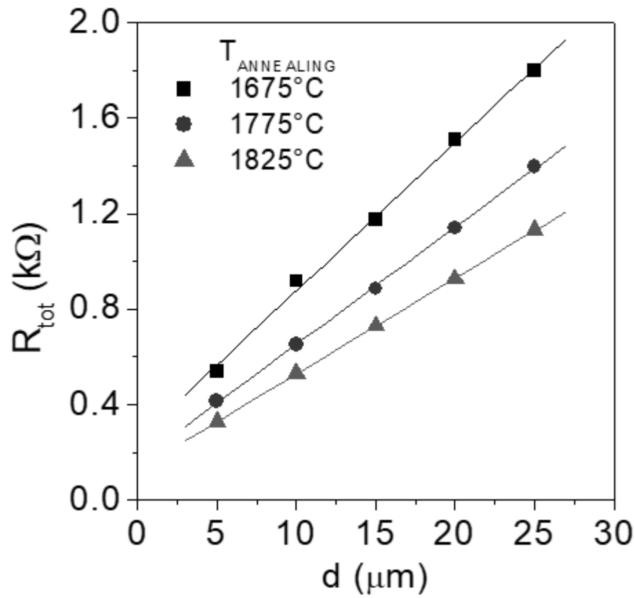

Fig. 5.11. Plots of the total resistance R_{TOT} as a function of the pad distance d, used for the extraction of the specific contact resistance, on Al-implanted 4H-SiC samples annealed at T_{ann}=1675°C, T_{ann}=1775°C and T_{ann}=1825°C.

The L-TLM analysis (see section 3.1.2) allowed to determine the following values of the specific contact resistance values: $(5.2\pm0.9)\times10^{-4}$ Ωcm^2 (T_{ann}=1675°C), $(2.6\pm0.3)\times10^{-4}$ Ωcm^2 (T_{ann}=1775°C) and

$(2.0\pm0.1)\times10^{-4}$ Ωcm^2 (T_{ann}=1825°C). As can be seen, the values of ρ_c decreases with the increase of the annealing temperature. This result is linked to the increase of the active Al-doping concentration as a function of the annealing temperature, calculated from the analysis Hall effect measurements. The values of sheet resistance of the p-type implanted 4H-SiC were: 12.4 kΩ/sq (T_{ann}=1675°C), 9.8 kΩ/sq (T_{ann}=1775°C) and 8.0 kΩ/sq (T_{ann}=1825°C). These results are consistent with the sheet resistance values calculated from Van der Pauw measurements, previously discussed.

Finally, Fig. 5.12 Shows the values of specific contact resistance as a function of the acceptor concentration N_A.

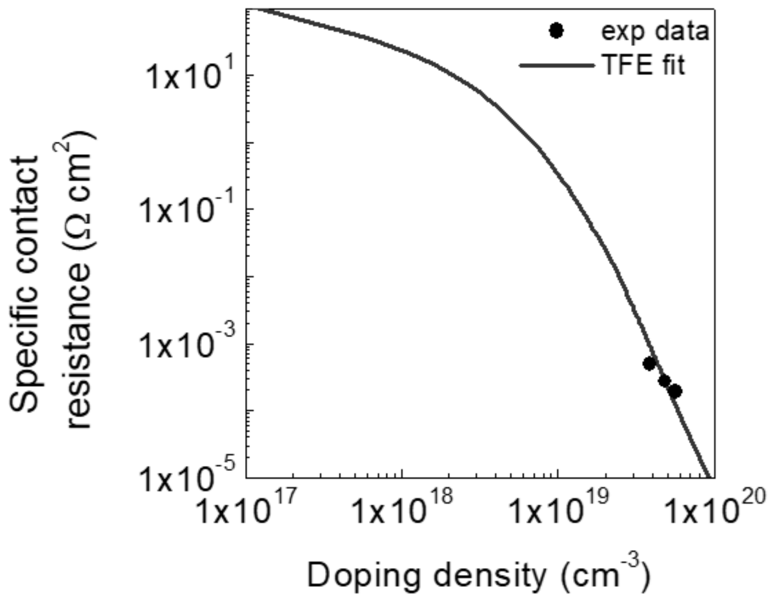

Fig. 5.12. Specific contact resistance of Ti/Al/Ni contacts as a function of the doping density on Al-implanted 4H-SiC samples annealed at T_{ann}=1675°C, T_{ann}=1775°C and T_{ann}=1825°C. The continuous line represents the fits of the experimental data with the neutrality equation.

The experimental data have been fitted with the Termionic Fied Emission (Eq. 37) mechanism in order to extrapolate the value of the Schottky barrier eight. This parameter resulted in a barrier height of 0.63 eV. Other literature works reported a TFE current transport mechanism for similar values of acceptor concentration in Ti/Al based contacts [115]. In these works, the barrier height depends on several parameters, such as the

doping, deposition technique, metal thickness, and annealing conditions. In fact, for a doping concentration of 4×10^{19} cm^{-3} barrier height values of 0.82eV [122], and 0.37 eV [110] have been reported. Slightly lower values of Schottky barrier have been obtained by Frazzetto et al. [115] (0.51 eV) and Vivona et al. [108] (0.56 eV) using Ti/Al based contacts on p-type 4H-SiC implanted at the same conditions. However, in this work the extrapolation of Φ_B has been made with a different method, e.g. by the dependence of ρ_c from the doping density.

5.2 *Ohmic contacts on 3C-SiC*

5.2.1. State of the art on Ohmic contacts on 3C-SiC

In the past years, Ohmic contacts formed using annealed Nickel- and Titanium-based metallic layers have been investigated on n-type heavily doped 3C-SiC layers, grown on different substrates [123,124,125]. Nickel is the most used metal for n-type 3C-SiC after annealing at temperatures up to 950°C [126]. In this context, the surface preparation method and the sample morphology are crucial issues affecting the contacts properties. Some treatments like the chemical mechanical polishing (CMP) are typically used to reduce the surface roughness and to improve the electrical properties of the contacts (reproducibility, specific contact resistance, reliability).

Very recently, Ohmic contacts were obtained on heavily doped (degenerate) n-type implanted 3C-SiC without annealing and applied to the fabrication of 3C-SiC MOSFETs [127]. However, only a limited work has been reported on moderately doped n-type 3C-SiC and on p-type doped 3C-SiC [128,129].

To overcome this lack of literature data, in this thesis, the properties of Ohmic contacts have been studied on n-type and p-type doped 3C-SiC layers grown on Si substrates, considering Ni and Ti/Al/Ni contacts.

5.2.2 Ohmic contacts on n-type 3C-SiC

The investigation on Ohmic contacts has been carried out on a moderately doped n-type 3C-SiC layer (with a nominal donor concentration of $N_D \sim 10^{17}cm^{-3}$) and thickness of 5 μm. The metal contacts consisted of $Ni_{(100nm)}$ films. In order to carry out the electrical characterization of the contacts, C-TLM structures have been fabricated on the sample surface combining optical lithography and lift-off of the metal (see section 3.3). In this case, differently from the case of 4H-SiC and AlGaN/GaN heterostructrures, here we have used C-TLM structures due to the difficulty to create a lateral isolation on such thick (5 μm) 3C-SiC layer. Then, the contacts were subjected to rapid thermal annealing at different temperatures up to 950°C in Ar atmosphere for 60s.

First, the electrical response of the contact has been studied as a function of the annealing temperature. For this purpose, the Ni contacts have been subjected to thermal process at temperature from 400°C to 950°C. Fig 5.13 shows the comparison of I-V curves acquired between adjacent contacts on C-TLM structures (distance d= 25 μm). As can be seen, the electrical behavior shows a gradual improvement upon annealing until achievement of Ohmic characteristics at 950°C.

Fig. 5.14 reports the I-V characteristics acquired on adjacent C-TLM pads for the Ni contacts annealed at 950°C together with the extrapolated values from the linear fit of the equation (53). By using the C-TLM analysis, it was possible to determine a specific contact resistance of 3.7×10^{-3} Ωcm^2, which is a reasonably good value for the moderate doping level ($N_D \sim 10^{17}cm^{-3}$) of the 3C-SiC layer.

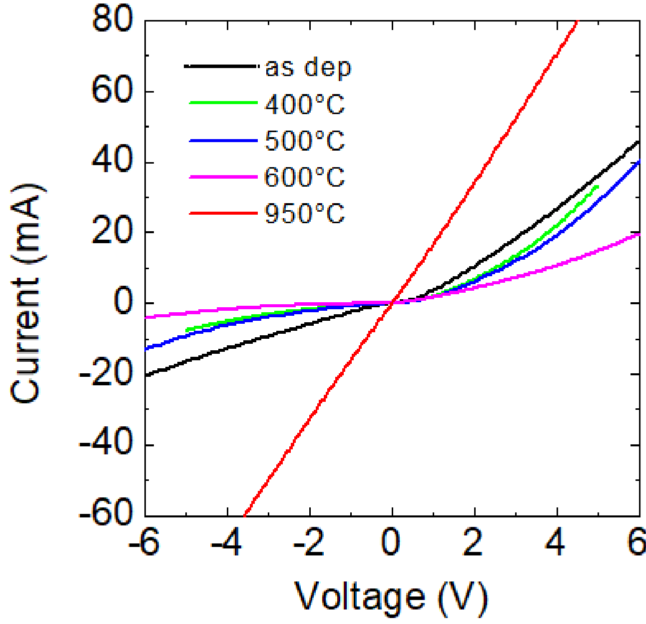

Fig. 5.13 I-V curves acquired between Ni contacts at a distance of 25 µm on n-type 3C-SiC at different annealing temperatures, showing an Ohmic behavior at 950°C.

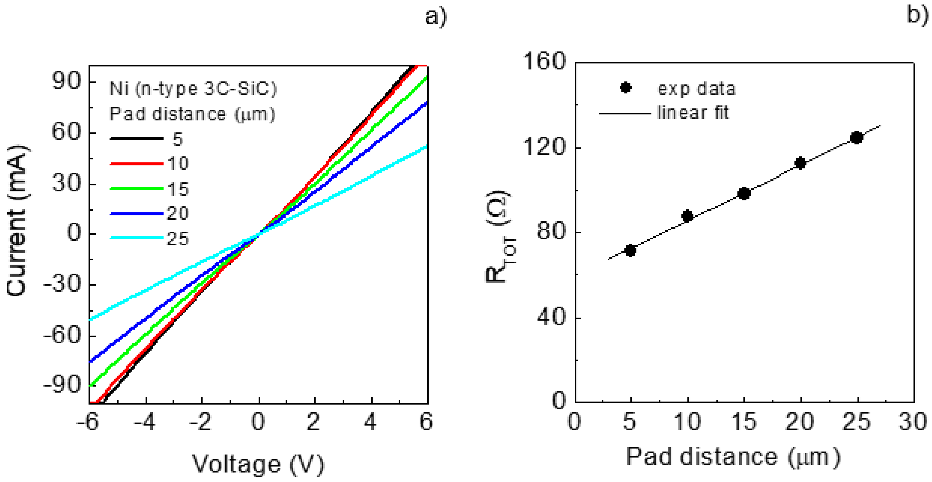

Fig. 5.14. I-V curves acquired on C-TLM structures at different distances for annealed (950°C) Ni contacts on moderately doped n-type 3C-SiC (a). Linear fit of the total resistance R_{TOT} as a function of the pad distance (b), used for the extraction of the specific contact resistance.

Fig 5.15 shows the AFM images acquired on the n-type 3C-SiC surface (Fig 5.15a) and on the Ni-contact surface annealed at 950°C, i.e., after Ohmic behaviour is reached (Fig 5.15b). The as-grown 3C-SiC material shows irregular morphology, resulting in a high surface roughness with a root mean square (RMS) value of 18.6 nm. As mentioned in section 1.1.3, such features are typically observed in 3C-SiC layers grown on Si, and are related to the presence of planar defects, such as anti-phase boundaries, twins and stacking faults characterizing the heteroepitaxial 3C-SiC layers [130].

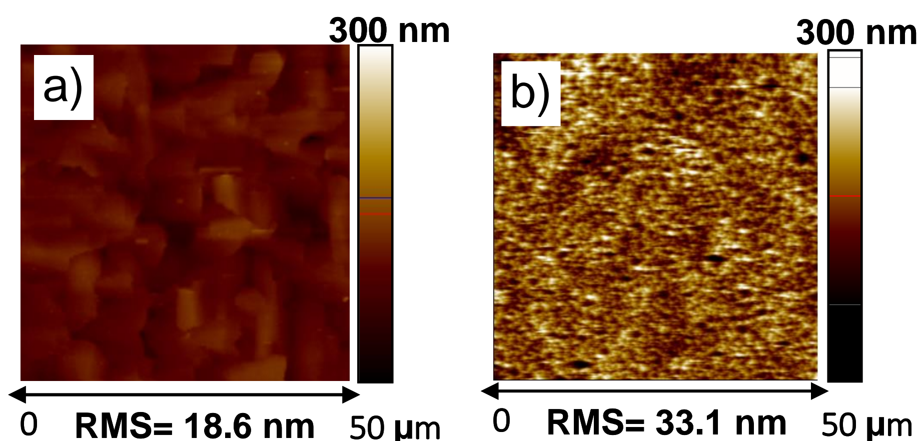

Fig. 5.15. AFM images of the bare n-type 3C-SiC sample surface (a) and of the Ni contact after annealing at 950°C (b).

After contact deposition and annealing, the metal surface exhibits a higher RMS value (33.1 nm) and its morphology suggest the occurrence of a solid state reaction. Then, XRD and TEM analysis have been performed in order to get more information on the contact microstructure after annealing. The XRD analysis of the Ni/3C-SiC sample after annealing at 950 °C are reported in Fig. 5.16 [131]. As can be seen, the XRD patterns indicate the formation of the nickel silicide phase (Ni_2Si) [132]. Fig. 5.17 shows the cross section TEM analysis of the sample. After the annealing treatment, the interface becomes very irregular , showing a reacted layer composed of Ni_2Si nickel silicide phase (confirming the XRD result) with embedded spherical carbon clusters. Hence, it can be argued that the formation of the silicide (Ni_2Si) is a key factor for the achievement of a Ohmic behavior in Ni/3C-SiC system.

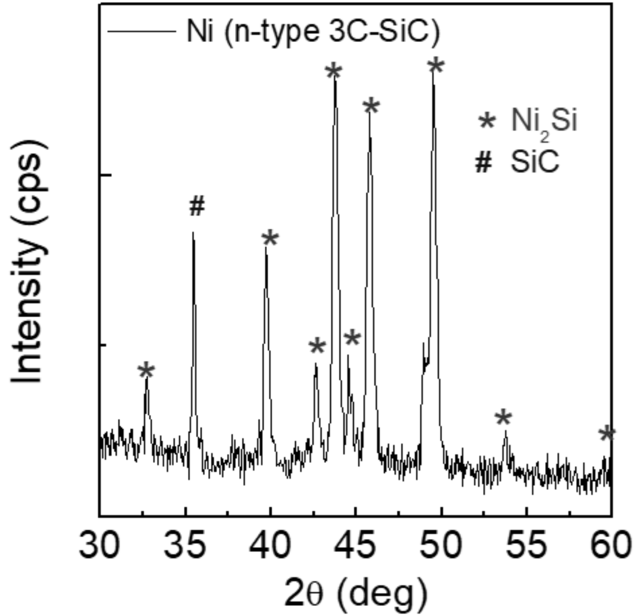

Fig. 5.16. XRD diffraction patterns of Ni/3C-SiC samples after annealing at 950°C.

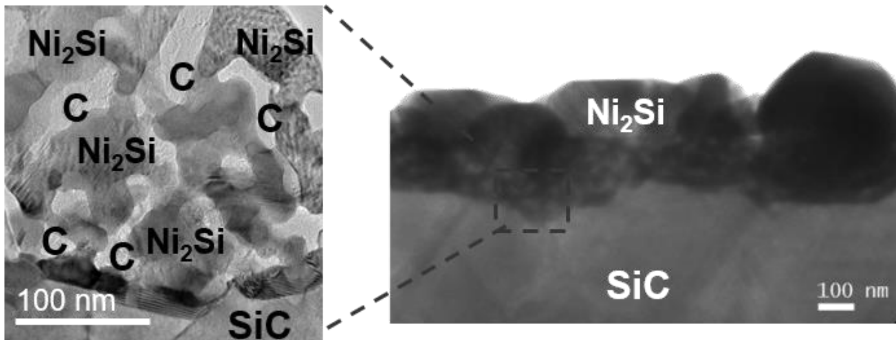

Fig. 5.17. Cross section TEM micrographs of Ni/3C-SiC samples after annealing at 950°C.

Finally, a $Ti_{(70nm)}/Al_{(200nm)}/Ni_{(50nm)}$ multilayer has been fabricated on the same n-type material. The contacts exhibited a Ohmic behaviour with similar values of ρ_c as the Ni_2Si contacts (i.e., in the order of 10^{-3} Ωcm^2). The AFM scans (Fig. 5.18) on the contacts surface showed a different

morphology with respect to Ni contacts. Also in this case high values of surface roughness have been detected.

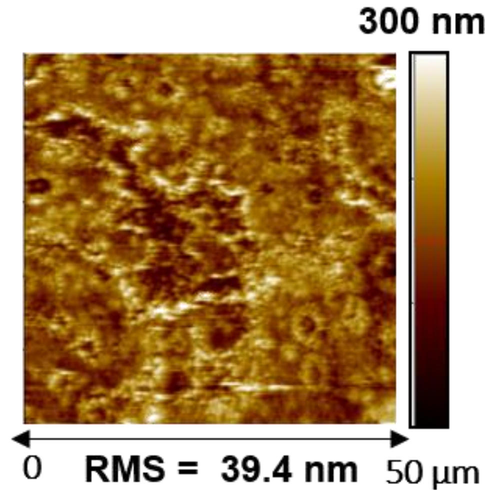

Fig. 5.18. AFM surface morphology of 950 °C annealed Ti/Al/Ni contacts to n-type 3C-SiC.

5.2.3 Ohmic contacts on p-type 3C-SiC

Heavily doped p-type 3C-SiC layers (1.1 µm thickness) with a nominal acceptor concentration of $N_A \sim 5\times10^{19}cm^{-3}$ were used to study the Ohmic contacts on p-type 3C-SiC. The p-type doping of the layer has been confirmed by Hall-effect measurements, not reported here. The metal contacts consisted of a $Ti_{(70nm)}/Al_{(200nm)}/Ni_{(50nm)}$ multilayer. Also in this case, C-TLM structures were used for the electrical characterization. These contacts have been annealed directly at 950°C. The I-V characteristics acquired on the C-TLM structures showed a linear behavior (Fig 5.19). The C-TLM analysis gave a very low value of the specific contact resistance, i.e., 1.8×10^{-5} Ωcm^2 , with respect to that found on Ni contacts on n-type 3C-SiC.

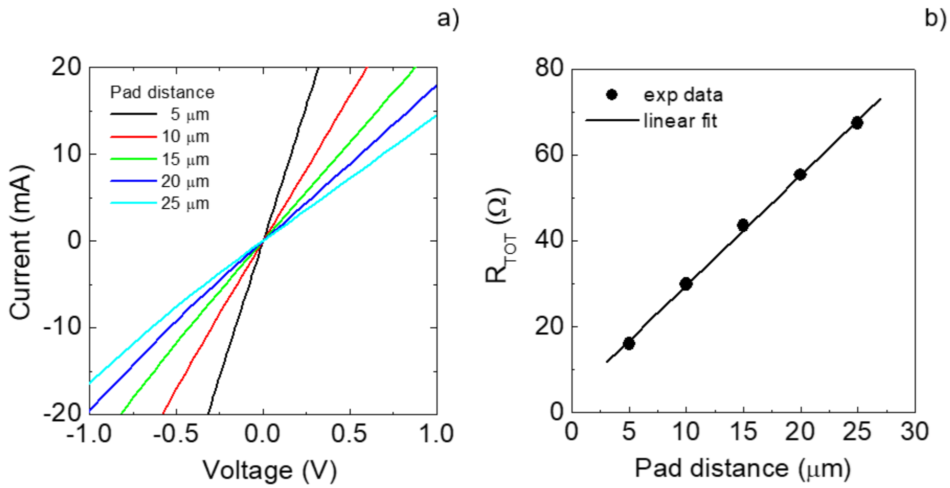

Fig. 5.19. I-V curves acquired on C-TLM structures at different distances for annealed (950°C) Ti/Al/Ni contacts on heavily doped p-type 3C-SiC (a). Linear fit of the total resistance R_{TOT} as a function of the pad distance, used for the extraction of the specific contact resistance (b).

Fig. 5.20 shows the AFM images of the surface of the p-type 3C-SiC material and that of the Ti/Al/Ni contact formed on it after annealing at 950°C with RMS values of 14.2 nm and 44.9 nm, respectively. Comparing the two contacts on n- and p-type 3C-SiC, the annealed Ti/Al/Ni layers exhibit a higher RMS with respect to the Ni ones.

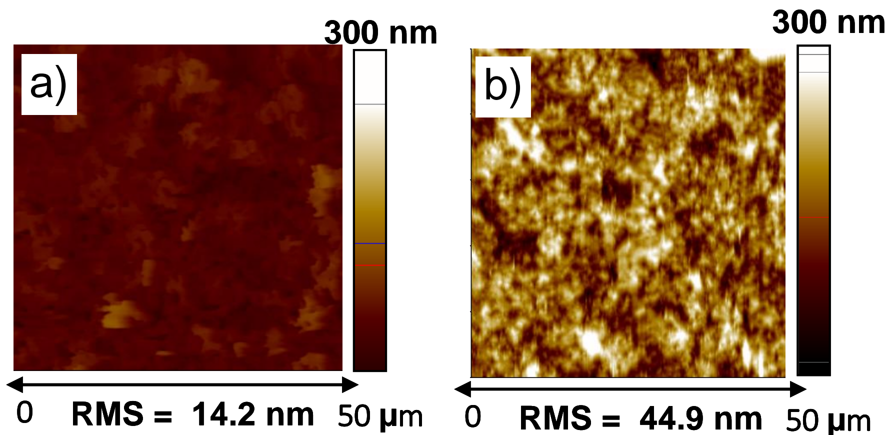

Fig. 5.20. AFM images of the bare p-type 3C-SiC sample surface (a) and of the Ti/Al/Ni contact after annealing at 950°C (b).

TEM image reported in Fig. 5.22 shows that this phase is typically localized in the uppermost part of the reacted stack. This result is rather similar to the behavior of the same Ti/Al/Ni multilayer on p-type 4H-SiC [108]. The lower part of the reacted metal shows a layered structures with a more irregular interface. With the help of EELS chemical maps, we were able to identify a ~6 nm thin TiC layer at the interface with 3C-SiC, which is probably responsible for the Ohmic behavior of the contact.

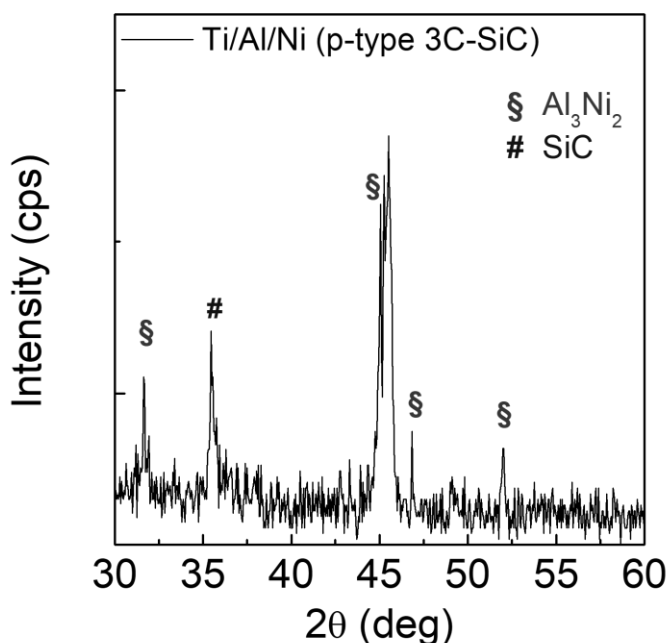

Fig. 5.21. XRD diffraction patterns of Ti/Al/Ni/3C-SiC samples after annealing at 950°C.

Sometimes, Ti/Al bilayers on 4H-SiC shows the ternary phase Ti_3SiC_2 upon annealing of 950°C [115], but in our Ti/Al/Ni system it was not observed, i.e., in the presence of a Ni cap layer.

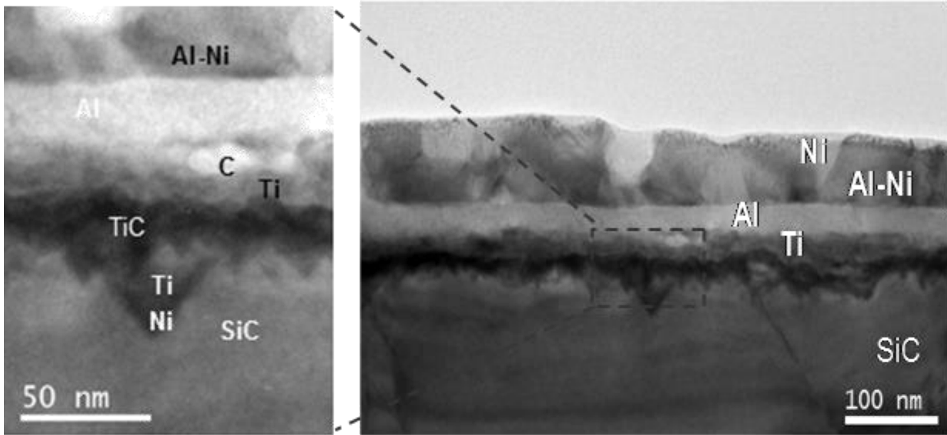

Fig. 5.22. Cross section TEM micrographs of Ti/Al/Ni/3C-SiC samples after annealing at 950°C.

In order to get insights into the transport mechanism at the metal/semiconductor interface, the temperature dependence of the specific contact resistance in Ti/Al/Ni contacts on the heavily doped p-type 3C-SiC was studied. Fig. 5.23 (a) shows the I-V characteristics acquired on adjacent C-TLM pads (d=25 μm) as a function of the measurement temperature in a range from 25°C to 150°C.

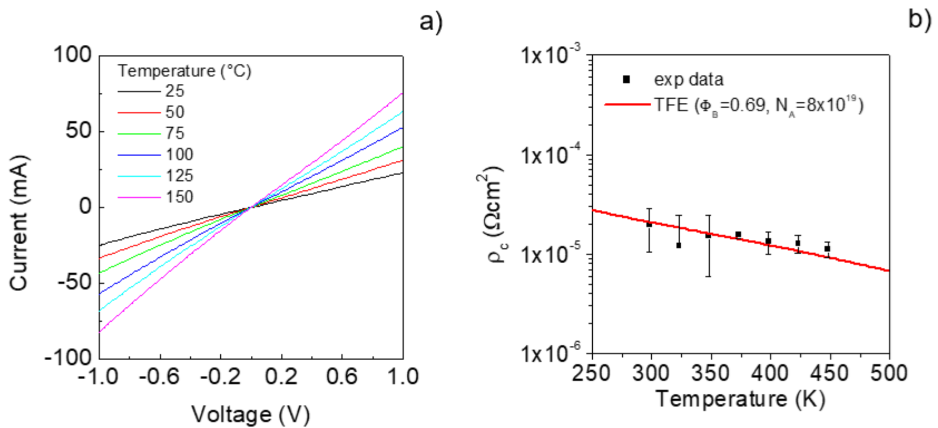

Fig. 5.23. I-V curves acquired between Ti/Al/Ni contacts at a distance of 25 μm on p-type 3C-SiC as a function of measurement temperatures (a). Temperature dependence of the specific contact resistance. The continuous line is the fit of the experimental data with the TFE model (b).

As can be seen, there is an increase of the current with the increase of the temperature. From the C-TLM analysis, the values of the specific contact resistance have been determined as a function of the measurement temperature and are reported in Fig. 5.23 (b). The values of ρ_c slightly decreased with increasing the measurement temperature. The current transport mechanism that better fitted the experimental ρ_c values was the TFE [46]. From the fit with the TFE model of the experimental data (depicted as continuous line in Fig. 7) a barrier height of Φ_B=0.69 eV and a carrier concentration $N_A=8\times10^{19}$ cm^{-3} have been determined. The value of the barrier height is higher that measured on 4H-SiC (0.56 eV) [108]. A lower barrier could be expected for the cubic polytype, this result suggests that the interface composition and roughness of the reacted layer on 3C-SiC plays a role in the formation of the Ohmic contact and of its barrier.
For completeness, the morphological and electrical behaviour of Ni contacts on the p-type material has been studied. In this case, the values of ρ_c (~ 4.9×10^{-3} Ωcm^2) were almost two orders of magnitude higher with respect to those obtained in annealed Ti/Al/Ni.

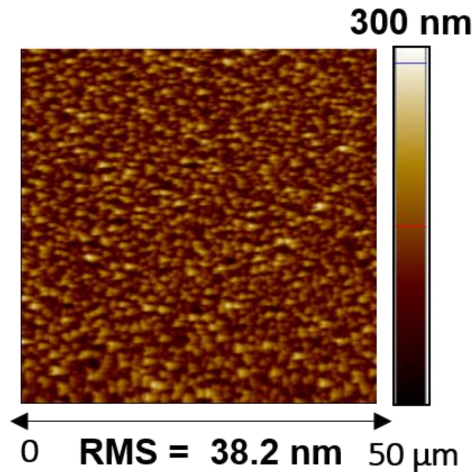

Fig. 5.24. AFM surface morphology of 950 °C annealed Ni contacts to p-type 3C-SiC.

This result confirms the difficulty of achieving good Ohmic contacts on p-type wide band gap materials and must be taken into account during device fabrication. Also in this case, from the morphological point of view, the

two types of contacts exhibited a different surface morphology (see Fig.5.24).

In conclusion, independently of the 3C-SiC substrate (n-type or p-type), annealed Ni contacts exhibited a better surface morphology than Ti/Al/Ni ones, but, these latter showed a better electrical behavior on p-type doped material. In general, the carrier transport properties are strongly influenced by the quality of the metal-semiconductor interface [124] and the improvement of the 3C-SiC morphology still remains a crucial issue. In this context, in the future, additional structural analyses of the interface could enable to clarify the physics behind Ohmic contact formation on 3C-SiC materials of different quality.

Conclusion and outlook

This thesis was focused on some physical issues related to Ohmic contacts formation on the wide band gap (WBG) semiconductors silicon carbide (SiC) and gallium nitride (GaN). Thanks to their properties, these semiconductors have become important candidate to replace silicon (Si) in power electronics devices. The formation of good Ohmic contacts on WBG semiconductors is still a challenging task, due to the high values of metal/semiconductor barrier height in these materials. Hence, this topic is continuous object of investigation.

The semiconductors studied in this thesis were AlGaN/GaN heterostructures, hexagonal silicon carbide (4H-SiC) and cubic silicon carbide (3C-SiC). The metal/semiconductor interfaces have been investigated with different techniques and with temperature dependent measurements, to identify the carrier transport mechanisms, determine the barrier height values, and correlate the electrical properties with the chemical and physical modification occurring upon annealing.

AlGaN/GaN heterostructures are mainly used for the fabrication of high electron mobility transistors (HEMTs). In this work, Au-free non-recessed Ta/Al/Ta and Ti/Al/Ti metal stacks have been compared to clarify the role of the interfacial metal in the Ohmic contact formation. In particular, both systems exhibited an Ohmic behavior after an annealing treatment of 600°C, with specific contact resistance values of $4.0\pm1.1\times10^{-4}$ Ω.cm^2 for Ta/Al/Ta and $1.6\pm0.6\times10^{-4}$ Ω.cm^2 for Ti/Al/Ti. The current transport at the interfaces was ruled by the Thermionic Field Emission (TFE) mechanism. The Schottky barrier height measured in these systems was 0.63 eV for Ta/Al/Ta and 0.58 eV for Ti/Al/Ti. These measurements were not previously reported in literature. The better electrical behavior of Ti-based contacts with respect to Ta-based ones has been associated with the different interfacial microstructure. In fact, the best Ohmic behavior in Ti-based contacts has been related to the creation of a TiN layer at the interface, thus leading to a lower barrier height and a better specific contact resistance. In our Au-free systems, the surface morphology of the contacts was improved with respect to the conventional Au-containing

metallization. A nanoscale analysis carried out by means of C-AFM demonstrated that isolated hillocks, present on the surface, have no significant impact on the contact resistance value. Preliminary experiments carried out on the Ti/Al/Ti contact indicated a further improvement of the electrical performance with the increase of the annealing time. On the other hand, an increase of the Ti thickness in contact to the AlGaN/GaN heterostructures leads to a higher barrier and a higher specific contact resistance, as well as a higher surface roughness.

Another subject of investigation was the modification of the sheet resistance (R_{SK}) under the contact. In fact, the structural modification occurring upon annealing can lead to significant changes on the electrical properties of the semiconductor underneath. In this case, only a limited number of literature data have been reported previously. To address this issue, "end contact resistance" measurements have been performed using appropriate test patterns. Experiments performed on a conventional Ti/Al/Ni/Au Ohmic contact demonstrated the significant decrease of the sheet resistance of the AlGaN/GaN heterostructure under the contact with respect to the sheet resistance outside the contact. This findings was correlated with the structural modification occurring upon annealing. The comparison with other literature results and additional measurements in Au-free systems (Ti/Al/Ti, Ta/Al/Ta, TiAlW) suggested that the modification of R_{SK} in AlGaN/GaN heterostructures can depend on several parameters, such as the contact resistance, the metal resistivity or even the geometry of the TLM pads. In particular, the correlation found between R_{SK} and ρ_C suggests the need of additional investigations to develop an analytical model describing this effect.

Hexagonal silicon carbide, 4H-SiC, is the most mature polytype already used for the fabrication of a wide variety of power devices, such as JBS and MOSFETs. In these devices, the fabrication of Ohmic contacts on p-type doped 4H-SiC regions is critical, due to the large Schottky barrier heights at metal/p-type semiconductor interface and the high ionization energy of the p-type dopants. Moreover, the semiconductor doping strongly influences the specific contact resistance. Hence, the comprehension of the electrical activation mechanism of the dopant is very important to achieve good Ohmic contacts on p-type 4H-SiC. In this work, the electrical

activation of the p-type implanted Al dopant on 4H-SiC was studied for different annealing conditions. The estimation of the active doping fraction has been performed by means of van der Paw and Hall-effect measurements, using an accurate analysis that considered the Hall scattering factor r_H recently reported in literature. In particular, an increase of the Al activation from 39% to 56% was found with increasing the post-implantation annealing temperature from 1675°C to 1825°C. On these implanted layers, a study of Ti/Al/Ni Ohmic contacts has been also carried out. A decrease of the specific contact resistance ρ_c was observed with the increase of the post-implantation annealing temperature, consistently with the increased active Al-doping concentration. The dependence of ρ_c on the active Al concentration was well modelled by the TFE theory, extracting a Schottky barrier height of 0.63 eV.

Finally, Ohmic contacts on the cubic polytype 3C-SiC have been studied. 3C-SiC is promising with respect to 4H-SiC, as it can be heteroepitaxially grown on large diameter Si substrates, facilitating the fabrication of power devices on a large scale and at a low cost. However, the quality of the available material severely limits its practical applications, and the electrical behaviour of metal/3C-SiC contacts can be strongly influenced by the material properties (defect density, surface roughness, surface preparation, etc.). In this case, Ni and Ti/Al/Ni contacts, annealed at 950°C, were studied on both n-type and p-type 3C-SiC. The specific contact resistance of annealed Ni contacts on moderately doped n-type 3C-SiC was 3.7×10^{-3} Ωcm^2. The formation of nickel silicide phase (Ni_2Si) has been detected after the annealing process, in a similar way as commonly observed in the hexagonal polytype. On the other hand, Ti/Al/Ni contacts on heavily doped p-type 3C-SiC showed a very low value of the specific contact resistance ($1.8\ \times10^{-5}$ Ωcm^2). After annealing, the intermixed stacks are characterized by the presence of Al_3Ni_2. In this case, a barrier height of 0.69 eV was determined, this value is higher than that measured on 4H-SiC, probably due to different interface composition and material quality. In fact, the 3C-SiC material typically shows irregular morphology, which can have an impact on the reaction kinetics. In our experiments, Ni contacts showed a better surface morphology than Ti/A/Ni

ones, independent of the 3C-SiC substrate (n-type or p-type). The Ti/Al/Ni contacts exhibited a better electrical behaviour on p-type doped material.

The experiments carried out in this thesis allowed to obtain some interesting results for a better comprehension of some metal systems for Ohmic contacts on AlGaN/GaN heterostructures, 4H-SiC and 3C-SiC. However, this work revealed the existence of additional scientific open issues that deserve further investigations. The results on Ohmic contacts on AlGaN/GaN heterostructures have a clear importance from a materials science point of view. In addition to that, the performed work has a technological relevance for the possible applications in GaN-on-Si HEMTs technology. In this context, the results suggested the possibility to explore the behaviour of a Ti/Al/Ta stack, in order to take the benefits of both systems, separately studied in this thesis. It is also clear that it is necessary to better clarify the role of the Ti thickness in the reaction kinetics and in the Ohmic properties. Hence, future experiments will be required to correlate the electrical behaviour with the contact microstructure. All the work performed on GaN-based heterostructures concerned "non-recessed" Ohmic contacts. In this frame, a partial or total recession of the AlGaN layer under the Ti/Al/Ti or Ta/Al/Ta contacts could be beneficial for the electrical properties and deserve a further investigation in the future.

The information obtained by this work on 4H-SiC can be particularly useful for JBS technology, where Ohmic contacts on highly doped p-type regions are present in the device structure. Firstly, the work confirmed that an accurate analysis is required to correctly determine the electrical activation of the dopant. Although the results obtained on Ti/Al/Ni Ohmic contacts on p-type implanted 4H-SiC followed the trend of the electrical activation of the Al-dopant, there are still discrepancies with respect to previous literature results on the values of the barrier height and specific contact resistance. This latter suggests that the reproducibility of the contact properties must be improved. To this aim, a better control of the 4H-SiC surface roughness after post-implantation annealing could be required.

Finally, the first results on Ohmic contacts were also reported for the cubic polytype 3C-SiC, focusing on Ni and Ti/Al/Ni contacts on n-type and p-type doped material. The interest for this polytype is growing, but the number of studies is still limited. In this case, it is clear that the quality of

the material strongly influences the contacts properties. For that reason, in the future it will be interesting to monitor the effects of an improvement of the morphology and of the reduction of the defect density in this material and on the electrical behaviour of metal/3C-SiC interfaces. Additionally, while this thesis has been focused on Ohmic contacts, it is clear that the formation of good Schottky contacts on 3C-SiC will be an open issue for the next years, being highly desired for the development of rectifying devices.

The aforementioned open issues can be at the basis of future activities at CNR-IMM in the framework of the running project on GaN and SiC.

Glossary

Abbreviations

2DEG	Two Dimensional Electron Gas
AFM	Atomic Force Microscopy
C-AFM	Conductive Atomic Force Microscopy
C-V	Capacitance-Voltage
EELS	Electron Energy Loss Spectroscopy
FE	Field Emission
HEMT	High Electron Mobility Transistor
HF	High Frequency
I-V	Current-Voltage
JBS	Junction Barrier Schottky
LED	Light Emitting Diode
MOCVD	Metal Organic Chemical Vapor Deposition
MOSFET	Metal Oxide Semiconductor Field Effect Transistor
PL	Photoluminescence
RMS	Root Mean Square
STEM	Scanning Transmission Electron Microscopy
TE	Thermionic Emission
TEM	Transmission Electron Microscopy
TFE	Thermionic Field Emission
TLM	Transmission Line Model
VdP	Van der Pauw
WBG	Wide Band Gap
XRD	X-Ray Diffraction

Commonly used symbols

A^*	Richardson's constant ($Acm^{-2}\ K^{-2}$)
a_0, c_0	Equilibrium lattice constants (Å)
a	lattice constant (Å)
B	Magnetic field (G)
C_{ij}	Elastic constants (GPa)

d_{AlGaN}	Thickness of the AlGaN layer (nm)
E_{00}	Characteristic energy (eV)
e_{ij},	Piezoelectric coefficients (C/m^2)
E	Electric field (MV/cm)
E_C	Critical electric field (MV/cm)
E_G	Band gap (eV)
h	Planck constant (J·s)
k_B	Boltzmann constant (m^2 ·kg/ s· K)
m_e	Electron mass (9.11×10^{-31} kg)
m^*	Effective mass (kg)
n	Electrons density (cm^{-3})
N_D, N_A	Donor, Acceptor density ($atoms/cm^3$)
n_i	Intrinsic carrier concentration (cm^{-3})
n_s	Sheet charge density of 2DEG ($electrons/cm^2$)
p	Holes density (cm^{-3})
P_{PE}	Piezoelectric polarization (C/m^2)
P_{SP}	Spontaneous polarization (C/m^2)
q	Elementary charge (1.6×10^{-19}C)
R_C	Contact resistance (Ω·mm)
R_H	Hall coefficient (m^3/C)
R_{ON}	Specific ON-resistance ($mΩ·cm^2$)
R_{SH}	Sheet resistance (Ω/sq)
R_{SK}	Sheet resistance under the contact (Ω/sq)
V_B	Breakdown voltage (V)
v_{sat}	Electron saturation velocity (cm/s)
V_{th}	Threshold voltage (V)
ΔE_C	Conduction band discontinuity (eV)
Φ_B	Barrier height (eV)
Φ_m	Metal work-function (eV)
Φ_s	Semiconductor work-function (eV)
χ_S	Electron affinity (eV)
k	Thermal conductivity (W/cm·K)
ε_0	Vacuum permittivity (F/cm)
ε_{GaN}, ε_{AlGaN}	Relative permittivity of GaN, AlGaN
ε_x, ε_y, ε_z	Strain coefficients
μ	Carrier mobility ($cm^2/V·s$)

ρ_c	Specific contact resistance ($\Omega \cdot cm^2$)
ρ	Resistivity ($\Omega \cdot cm$)
σ	Polarization-induced charge density (C/cm2)

Curriculum Vitae

Personal Informations

Surname	Spera
First name	Monia
Nationality	Italian
Date of birth	20/09/1988

Education

2007: Scientific High School "B. Croce" of Palermo, Italy.

2013: Bachelor's Degree in Physics (98/110) at University of Palermo, Italy.
Thesis: Luminescence of a photovoltaic cell.
Tutor: Prof. M. Cannas (University of Palermo)

2016: Master's Degree in Physics (110/110 cum Laude) at University of Palermo, Italy.
Thesis: Photoinduced reactions of luminescence silica centres in controlled atmosphere.
Tutor: Prof. M. Cannas (University of Palermo).

2019: PhD in Material Science and Nanotechnology at University of
Catania, Italy.
Thesis: Ohmic contacts on Wide Band Gap semiconductors
Tutor: Prof. M. Cannas (University of Palermo), co-tutor dott. Fabrizio Roccaforte (CNR-IMM, Catania).

Publications:

L. Spallino, **M- Spera,** L. Vaccaro, S. Agnello, F.M. Gelardi, A.F. Zatsepin, M. Cannas, "*Environment assisted photoconversion of luminescent surface defects in SiO_2 nanoparticles",* Appl. Surf. Science **420, (**2017) 94-99.

M. Spera, C. Miccoli, R. Lo Nigro, C. Bongiorno, D. Corso, S. Di Franco, F. Iucolano, F. Roccaforte, G. Greco, "*Modification of the sheet resistance under Ti/Al/Ni/Au Ohmic contacts on AlGaN/GaN heterostructures*", Mater. Sci. Semicond. Proc. **78**, (2018) 111-117.

M. Spera, G. Greco, R. Lo Nigro, S. Di Franco, D. Corso, P. Fiorenza, F. Giannazzo, M. Zielinski, F. La Via, F. Roccaforte, *Fabrication and characterization of ohmic contacts to 3C-SiC layers grown on Silicon*, Mater. Sci. Forum **963** (2019) 485-489

M. Spera, D. Corso, S. Di Franco, G. Greco, A. Severino, P. Fiorenza, F. Giannazzo, F. Roccaforte, "*Effect of high temperature annealing (T > 1650°C) on the morphological and electrical properties of p-type implanted 4H-SiC layers*", Mater. Sci. Semicond. Proc. **93**, (2019) 274-279.

M. Spera, G. Greco, R. Lo Nigro, C. Bongiorno, F. Giannazzo, M. Zielinski, F. La Via, F. Roccaforte, "*Ohmic contacts on n-type and p-type cubic silicon carbide (3C-SiC) grown on Silicon"*, Mater. Sci. Semicond. Proc. **93**, (2019) 295-298

F. Roccaforte, F. Giannazzo, A. Alberti, **M. Spera**, M. Cannas, I. Cora, B. Pécz, F. Iucolano, G. Greco, *"Barrier inhomogeneity in vertical Schottky diodes on free standing gallium nitride"*, Mater. Sci. Semicond. Proc. **94** (2019) 164-170

M. Spera, G. Greco, R. Lo Nigro, S. Scalese, C. Bongiorno, M. Cannas, F. Giannazzo, F. Roccaforte, "*Metal/Semiconductor*

Barrier Properties of Non-Recessed Ti/Al/Ti and Ta/Al/Ta Ohmic Contacts on AlGaN/GaN Heterostructures" *Energies* **12** (2019) 2655

M. Spera, G. Greco, D. Corso, S. Di Franco, A. Severino, A. A. Messina, F. Giannazzo. F. Roccaforte, "*Ohmic contacts on p-type Al-implanted 4H-SiC layers after different post-implantation annealings*" Materials 2019, **12**, 3468

International congresses:

M. Spera, G. Greco, C. Miccoli, R. Lo Nigro, C. Bongiorno, D. Corso, S. Di Franco, F. Iucolano, F. Roccaforte, "Sheet resistance under Ohmic contacts on AlGaN/GaN heterostructures".
Oral communication presented at the WOCSDICE congress (Bucharest, Romania, may 2018).

M. Spera, G. Greco, R. Lo Nigro, C. Bongiorno, S. Scalese, S. Di Franco, P. Badalà, F. Iucolano, M. Krysko, M. Leszczynski, F. Giannazzo, F. Roccaforte, "Comparative study of Ta and Ti-based contacts to AlGaN/GaN heterostructures".
Oral communication presented at the EXMATEC congress (Bucharest, Romania, may 2018).

M. Spera, G. Greco, R. Lo Nigro, C. Bongiorno, S. Scalese, S. Di Franco, F. Iucolano , F. Giannazzo, F. Roccaforte "Ti/Al/Ti and Ta/Al/Ta Ohmic contacts to AlGaN/GaN heterostructures". Oral communication presented at EMRS 2018 congress (Warsaw, Poland, September 2018)

M. Spera, D. Corso, S. Di Franco, G. Greco, A. Severino, P. Fiorenza, F. Giannazzo, F. Roccaforte "Effect of high temperature annealing ($T > 1650°C$) on the morphological and electrical properties of n-type and p-type implanted 4H-SiC layers" Oral

communication presented at EMRS 2018 congress (Warsaw, Poland, September 2018)

M. Spera, D. Corso, S. Di Franco, G. Greco, A. Severino, P. Fiorenza, F. Giannazzo, F. Roccaforte "Electrical activation of n-type and p-type ion-implanted 4H-SiC upon high temperature annealing" Oral communication presented at EMRS 2019 congress (Nice, France, May 2019)

M. Spera, G. Greco, R. Lo Nigro, S. Scalese, S. Di Franco, C. Bongiorno, F. Giannazzo, F. Iucolano , F. Roccaforte "Study of metal/semiconductor current transport mechanism of Ti- and Ta- "Au-free" Ohmic contacts on AlGaN/GaN heterostructures " Oral communication presented at FISMAT 2019 congress (Catania, Italy, 30 Set- 4 Oct 2019)

F. Roccaforte , M. Spera, G. Greco, R. Lo Nigro, M. Zielinski, F. La Via, F. Giannazzo, P. Fiorenza "Ohmic metallizations and gate dielectrics on cubic silicon carbide" Poster presented at EMRS 2019 congress (Nice, France, May 2019)

M. Spera, G. Greco, C. Miccoli, R. Lo Nigro, C. Bongiorno, D. Corso, S. Di Franco, F. Iucolano , F. Roccaforte "Sheet resistance under Ohmic contacts on AlGaN/GaN heterostructures" Poster presented at EMRS 2018 congress (Warsaw, Poland, September 2018)

M. Spera, G. Greco, R. Lo Nigro, S. Di Franco, D. Corso, P. Fiorenza, F. Giannazzo, M.Zielinski, F. La Via F. Roccaforte "Ohmic contacts on n-type and p-type cubic silicon carbide (3C-SiC) grown on Silicon" Poster presented at EMRS 2018 congress (Warsaw, Poland, September 2018)

F. Roccaforte , M. Spera, G. Greco, R. Lo Nigro, M. Zielinski, F. La Via, F. Giannazzo, P. Fiorenza "Electrical properties of Ohmic contacts and gate dielectrics on cubic silicon carbide" Poster

presented at FISMAT 2019 congress (Catania, Italy, 30 Set- 4 Oct 2019)

Conference proceedings:

G. Greco, F. Giannazzo, **M. Spera**, M. Cannas, A. Alberti, F. Iucolano, F. Roccaforte, *"Ni based Schottky contacts in bulk GaN"*, Proc. of Workshop on Compound Semiconductor Devices and Integrated Circuits Held in Europe (WOCSDICE2018), Bucharest (Romania), 14-16 May 2018, edt. M. Dragoman, pp. 39-40.

M. Spera, G. Greco, C. Miccoli, R. Lo Nigro, C. Bongiorno, D. Corso, S. Di Franco, F. Iucolano, F. Roccaforte, *"Sheet resistance under Ohmic contacts on AlGaN/GaN heterostructures"*, Proc. of Workshop on Compound Semiconductor Devices and Integrated Circuits Held in Europe (WOCSDICE 2018), Bucharest (Romania), 14-16 May 2018, edt. M. Dragoman, pp. 56-57.

M. Spera, G. Greco, R. Lo Nigro, C. Bongiorno, S. Di Franco, P. Badalà, F. Iucolano , M. Krysko, Leszczynski, F. Giannazzo, F. Roccaforte, "*Comparative study on non-recessed Au-free Ti- and Ta-based Ohmic contacts on AlGaN/GaN heterostructures"*, Proc. of Expert Evaluation and Control of Compounds Semiconductor Materials and Technologies (EXMATEC 2018), Bucharest (Romania), 16-18 May 2018, edt. M. Dragoman, pp. 31-32.

G.Greco, **M.Spera**, S. Di Franco, R. Lo Nigro, F. Giannazzo, F. Roccaforte, "*Tungsten Carbide (WC) Schottky contacts in AlGaN/GaN heterostructures*" Proceedings of the 43rd Workshop on Compound Semiconductors Devices and Integrated Circuits (WOCSDICE 2019), Eds. Cabourg, France, May 2018

Awards:

Best Graduate Student Award

EMRS 2018 Fall Meeting – Symposium R "*New frontiers in wide-bandgap semiconductors and heterostructures for electronics, optoelectronics and sensing*", Warsaw September 17 - 21, 2018

Best Graduate Student Award

EMRS 2019 Spring Meeting - Symposium X "*Silicon carbide and related materials for energy saving applications*", Nice May 27 - 31, 2019

Acknowledgments

It has been almost three years since the start of my PhD and, looking back, it is unbelievable how quickly this time has passed. Changes and choices are always complicated to deal with, but I am happy to have taken this path, to have worked at the CNR-IMM in Catania, to have entered the world of microelectronics and moved to this wonderful city.

This path has come to the end also thanks to some people, who have shaped me both from a scientific and personal point of view.

The enthusiasm and constructive criticism of both my tutors have been very important to motivate myself. Hence, the first acknowledgment is due to Dr. Fabrizio Roccaforte for giving me the opportunity to work on interesting and challenging topics. With patience, he has been "The Guide" for my research activities offering his scientific experience on the wide band gap semiconductors. Somehow, he believed that I could do it! And I'm very grateful for all the time that he spent with me improving both my skills and my scientific knowledge in the field. Then, a special thank goes to prof. Marco Cannas, for his unwavering advice, motivation and support, other than the useful scientific discussions. He accompanied me morally and professionally in this exciting scientific journey.

I should have never finished my PhD without the daily help of Dr. Giuseppe Greco, since the first time I entered a laboratory. I want to thank him for his support and for always being ready to say that we would have solved any problem.

I sincerely want to thank the entire research group at CNR-IMM in Catania. All the people have contributed to my professional growth. With some of them, I shared unforgettable moments during trips, conferences and convivial events. Dr. Filippo Giannazzo is acknowledged for his suggestions and scientific discussions that have been very useful during the activity, in particular about AFM analyses. Thanks to Dr. Patrick Fiorenza

for sharing of his experience on electrical analyses, and Dr. Raffaella Lo Nigro for the XRD analysis and their interpretation. I want to thank Dr. Domenico Corso for his accuracy in electrical measurements on the Hall-Effect instrumentation. A special thank goes to Dr. Salvo Di Franco for the help in fabricating test patterns and devices and for the assistance in the clean room. A deep thank to Dr. Emanuela Schilirò, companion of all the working days, of trips and, above all, friend. Thanks for your support! Finally, I want to thank Dr. Corrado Bongiorno for the TEM analyses and interpretation, and for the chats and moral support.

During my PhD, the collaboration with STMicroelectronics on silicon carbide and gallium nitride topics was very important. For that, I have to acknowledge several people: Dr. Mario Saggio, Dr. Simone Rascunà, Dr. Ferdinando Iucolano, Dr. Alessia Frazzetto and Dr. Andrea Severino. Among them, Dr. Antonino Parisi and Dr. Tuccio Reina are acknowledged for the precious assistance during the experimental sessions in electrical laboratory. Dr. Paolo Badalà is acknowledged for assistance in sample preparation.

I would like to thank prof. Mike Leszczynski, Dr. Pawel Pristawko and Dr. Piotr Kruszewski from the Institute of High Pressure Physics (Unipress) in Warsaw, for the useful scientific discussions and for the hospitality during several visits in Poland at their institute, in the framework of the bilateral cooperation project ETNA. Moreover, Dr. Ewa Grzanka and Dr. Marcin Kryśko are acknowledged for XRD analysis.

I also want to thank all the colleagues of CNR-IMM of the “boxes 2 and 3” and of the laboratories. With them, I have shared various moments of the working day life and coffee breaks.

I am grateful for the new friendships, with which I learned about a part of Sicily that I did not know yet, confirming the love for this place, with its pros and cons.

A special thank goes to my last roommate, for sharing the house and the moods.

An unquantifiable acknowledge goes to my family, my mother my father, my brother and my cousin/sister, for their endless love and support.

Finally, a special thanks to some people whose gestures were worth than a thousand words.

References

[1] D.A. Neamen, Semiconductor Physics and Devices, Basic Principles (3rd ed., Mc Graw Hill, 2003)

[2] P.Y. Yu, and M. Cardona, Fundamentals of Semiconductors. Physics and Material Properties (Springer, Berlin, 1995)

[3] S.E. Saddow, and A. Agarwal, Advances in Silicon Carbide Processing and Applications (Artech House, Norwood, MA, 2004)

[4] Taylor, A., Jones, R.M. in Silicon Carbide - A High Temperature Semiconductor , Eds. O'Connor, J.R., Smiltens, J., Pergamon Press, Oxford, London, New York, Paris 1960, 147

[5] J. I. Pankove and T. D. Moustakas in Gallium Nitride (GaN), Academic Press, San Diego, 1998.

[6] F. La Via, A. Severino, R. Anzalone, C. Bongiorno, G. Litrico, M. Mauceri, M. Schoeler, P. Schuh, P. Wellmann, Mater. Sci. Semicond. Proc. 78, (2018) 57-68.

[7] Kevin J. Chen et al. IEEE Trans. Electron Device, 64, (2017) NO. 3

[8] A.A. Lebedev, Semicond. Sci. Technol. 21, R17, 2006

[9] F Roccaforte, F Giannazzo, F Iucolano, J Eriksson, MH Weng, V Raineri Appl. Surf. Sci. 256 (19), (2010) 5727-5735

[10] Casady JB, “Processing of Silicon Carbide for Devices and Circuits” in Wide Bandgap Semiconductors, edited by Person SJ, William Andrew Publishing, Norwich, NY, 2000, and references therein.

[11] Harris GL, Properties of Silicon Carbide, London: INSPEC, the Institution of Electrical Engineers, 1995.

[12] H. Morkoc, S. Srite, GB Gao, Lin ME, B. Sverdlov, M. Burns, Journal of Applied Physics, 76 (1994) 1363

[13] JB Casady, RW Johnson, Solid State Electronics, 39 (1996) 1409.
[14] SE Saddow, A Agarwal, Advances in Silicon Carbide Processing and Applications, Boston, MA: Artech House Publisher, 2004.
[15] Ren F. and Zolper J. C., Wide Band Gap Electronic Devices (World Scientific,Singapore) 2003.
[16] Pearton S. J., Abernathy C. R. and Ren F., Gallium Nitride Processing for Electronics, Sensors and Spintronics (Springer Verlag, London) 2006.
[17] Cook T. E., Fulton C. C., Mecouch W. J., Davis R. F., Lucovski G. and Nemanich R. J., J. Appl. Phys., 94 (2003) 3949.
[18] W. J. Choyke, D. R. Hamilton, and L. Patrick, Physical Review, 133 (1964) A1163–A1166
[19] S.M. Sze, "Physics of Semiconductor Devices", John Wiley & Sons, New York, 1981.
[20] S. C. Jain, M. Willander, J. Narayan, and R. Van Overstraeten, Journal of Applied Physics 87 (2000) 965
[21] O. Ambacher, B. Foutz, J. Smart, J. R. Shealy, Journal of Applied Physics, vol.87 (2000)
[22] O. Ambacher, J. Smart, J. R. Shealy, N. G. Weimann, K. Chu, M. Murphy, W. J. Schaff, L. F. Eastman, J. Appl. Phys. 85 (1999) 3222
[23] L. S. Yu, D. J. Qiao, Q. J. Xing, S. S. Lau, K. S. Boutros, J. M. Redwing, Appl. Phys. Lett. 73 (1998) 238
[24] K. Brennan and A. Brown, Theory of modern electronic semiconductor devices, John Wiley and Sons, New York (2002)
[25] B. Jayant Baliga, Fundamentals of Power Semiconductor Devices, Springer (2008)
[26] F. Roccaforte P. Fiorenza, G. Greci, R. Lo Nigro, F. Giannazzo, F. Iucolano, M. Saggio, Microelectronic Engineering 187–188 (2018) 66–77
[27] EO. Johnson, RCA Review 26, 163, (1965)

[28] F. Roccaforte, G. Greco, P. Fiorenza and F. Iucolano, Materials 2019, 12, 1599

[29] B. Baliga, IEEE Electron Device Lett., VOL. 10, NO. 10, OCT.1989

[30] https://www.electronicsweekly.com/uncategorised/gan-on-si-power-transistors-french-lab-leti-2015-07/

[31] G. Greco Expert Evaluation and Control ofCompounds of Semiconductor Materials and Technologies (EXMATEC) 2018 conference, Bucharest, Romania, 16-18 MAY 2018, invited talk.

[32] F. Roccaforte, G. Brezeanu, P. M. Gammon, F. Giannazzo, S. Rascunà, M. Saggio, Advancing Silicon Carbide Electronics Technology I, Materials Research Foundations 37 (2018)

[33] R. Quai, Gallium Nitride Electronics, Springer Verlag, Berlin Heidelberg, 2008

[34] F. Roccaforte, F. Iucolano, F. Giannazzo, A. Alberti, V. Raineri Appl. Phys. Lett. 89 (2006) 022103

[35] F. Roccaforte, A. Frazzetto, G. Greco, F. Giannazzo, P. Fiorenza, R. Lo Nigro, M. Saggio, M. Leszczyński, Prystawko, V. Raineri, Appl. Surf. Sci. 258 (2012) 8324

[36] R. Nipoti, H.M. Ayedh, B.G. Svensson, Defects related to electrical doping of 4H-SiC by ion implantation, Mater. Sci. Semicond. Proc. 78, (2018) 13-21

[37] S. Contreras, L. Konczewicz, R. Arvinte H. Peyre1, T. Chassagne M. Zielinski, and S. Juillaguet Phys. Status Solidi A 214 (2017) 1600679

[38] K.K. Lee, G. Pensl, M. Soueidan, G. Ferro, Y. Monteil, Jpn. J. Appl. Phys. 45, (2006) 6823-6829

[39] A. Schöner, M. Krieger, G. Pensl, M. Abe, H. Nagasawa, Chem. Vapor Depos. 12 (2006) 523-530.

[40] H. Nagasawa, M. Abe, K. Yagi, T. Kawahara, N. Hatta, Phys. Status Solidi b 245 (2008) 1272-1280

[41] M. Kobayashi, H. Uchida, A. Minami, T. Sakata, R. Esteve, A. Schöner, Mater. Sci. Forum 679-680 (2011) 645-648

[42] E.H. Rhoderick, R.H. Williams, Metal-Semiconductor contacts, Oxford Science Publications, Oxford, 1988

[43] W. Grieshaber E. F. Schubert, and I. D. Goepfert, J. Appl. Phys. 80, 1996, 4615

[44] M. A. Reshchikov, H, Morkoç, J. Appl. Phys. 97 (2005) 061301

[45] H. H. Berger, Solid-State Electron. 15 (1972) 145-158.

[46] D.K. Schroder, Semiconductor Material and Device Characterization, John Wiley & Sons, Inc., Hobeken (USA), Third Edition, 2006.

[47] L. J. van der Pauw, Philips Technical Review, 20 (1958) 220-224

[48] G. Greco, F. Iucolano, F. Roccaforte, Appl. Surf. Sci (2016) 383 -324

[49] L. Wang, F.M. Mohammed, I. Adesidaa, J. Appl. Phys. 101 (2007) 013702

[50] F. Iucolano, G. Greco, F. Roccaforte Appl. Phys. Lett. 103 (2013) 201604

[51] M.W. Fay, G. Moldovan, N.J. Weston, P.D. Brown, I. Harrison, K.P. Hilton, A.Masterton, D. Wallis, R.S. Balmer, M.J. Uren, T. Martin, J. Appl. Phys. 96 (2004) 5588

[52] S.N. Mohammad, J. Appl. Phys. 95 (2004) 7940

[53] F. Iucolano, F. Roccaforte, A. Alberti, C. Bongiorno, S. Di Franco, and V. Raineri, J. Appl. Phys. 100 (2006) 123706

[54] M. Mohamad, F. Mustafa, M.S.Z. Abidin, S.F.A. Rahman, N.K.A. Al-Obaidi,A.M. Hashim, A.A. Aziz, M.R. Hashim, Melaka, Malaysia, 28–30 June, IEEE Proc. of the International Conference on Semiconductor Electronics (ICSE), 301 (2010)

[55] F. Recht, L. McCarthy, S. Rajan, A. Chakraborty, C. Poblenz, A. Corrion, J.S.Speck, U.K. Mishra, IEEE Electron Device Lett. 27 (2006) 205

[56] F. Iucolano, F. Giannazzo, F. Roccaforte, L. Romano, M.G. Grimaldi, V. Raineri, Nucl. Instrum. Methods Phys. Res. B 257 (2007) 336

[57] X. Liu, C. Zhan, K. W. Chan, W. Liu, L. S. Tan, K. J. Chen, and Y. C. Yeo Appl. Phys. Express 5 (2012) 066501

[58] A. Constant J. Baele, P. Coppens, W. Qin, H. Ziad, E. De Backer, P. Moens, and M. Tack J. Appl. Phys. 120 (2016) 104502

[59] A. Pooth J.Bergsten, N. Rorsman, H.Hirshy, R.Perks, P.Tasker, T.Martin, R.F.Webster, D.Cherns, M.J. Uren , M. Kuball Microelectronics Reliability 68 (2017) 2–4

[60] G. Greco F. Giannazzo, F. Iucolano, R. Lo Nigro, and F. Roccaforte, J. Appl. Phys. 114 (2013) 083717

[61] B. Van Daele and G. Van Tendeloo, Appl.Phys. Lett. 87 (2005) 061905

[62] A. Firrincielli, B. De Jaeger, S. You, D. Wellekens, M. Van Hove, and S. Decoutere, Jpn. J. Appl. Phys. 53 (2014) 04EF01

[63] A. Malmros, H. Blanck, N. Rorsman, Semicond. Sci. Technol. 26 (2011) 075006

[64] G. Greco, F. Iucolano, C. Bongiorno, F. Giannazzo, M. Krysko, M. Leszczynski, F. Roccaforte Appl. Surf. Scie. 314 (2014) 546–551

[65] G. Greco, F. Iucolano, C. Bongiorno, S. Di Franco, R. Lo Nigro, F. Giannazzo, P. Prystawko, P. Kruszewski, M. Krysko, E. Grzanka, M. Leszczynski, C. Tudisco, G.G. Condorelli, and F. Roccaforte, Phys. Status Solidi A (**2015**) 1–8

[66] B. P. LutherS. E. MohneyT. N. JacksonM. Asif Khan, Q. Chen, and J. W. Yang, Appl. Phys. Lett. 70 (1997) 57

[67] H. Kim, J.-H. Ryou, R.D. Dupuis, S.-N. Lee, Y. Park, J.-W. Jeon, T.-Y. Seong, Appl. Phys. Lett. 93 (2008) 192106

[68] Z. Fan, S.N. Mohammad, W. Kim, O. Aktas, A.E. Botchkarev, H. Morkoc, Appl.Phys. Lett. 68 (1996) 1672

[69] S. Ruvimov, Z.L. Weber, J. Washburn, K.J. Duxstad, E.E. Haller, Z.F. Fan, S.N.Mohammad, W. Kim, A.E. Botchkarev, H. Morkoc, Appl. Phys. Lett. 69 (1996) 1556

[70] D. Qiao, L. Jia, L. S. Yu, P. M. Asbeck, S. S. Lau, S.-H. Lim, Z. Liliental-Weber, T. E. Haynes, and J. B. Barner Journal of Applied Physics 89 (2001) 5543

[71] S.-H. Lim, J. Washburn, Z. Liliental-Weber, and D. Qiao, Appl. Phys. Lett. 78 (2001) 3797

[72] U. R. Kattner, J. C. Lin, and Y. A. Chang, Metall. Trans. A 23 (1992) 2081

[73] P. R. Subramanian, D. B. Miracle, and S. Mazdiyasni, Metall. Trans. A 21 (1990) 539

[74] Takahiro Yoshida and Takashi Egawa, Phys. Status Solidi A 215 (2018) 1700825

[75] Kanemura M., Yoshikawa S. and Tagi T., 2006 Compound semiconductor device and its manufacturing method, Fujitsu Ltd JP2006165207

[76] M. Spera, C. Miccoli, R. Lo Nigro, C. Bongiorno, D. Corso, S. Di Franco, F. Iucolano, F. Roccaforte, G. Greco, Mater. Sci. Semicond. Process. 78, (2018) 111

[77] E. V. Erofeev I. V. Fedina , V. V. Fedinaa , and A. P. Fazleev, Semiconductors, 53 (2019) 237–240

[78] R. Gong, J. Wang, S. Liu, Z. Dong, M. Yu, C.P. Wen, Y. Cai, B. Zhang, Appl. Phys.Lett. 97 (2010) 062115

[79] Hyung-Seok Lee, Dong Seup Lee, and Tomas Palacios IEEE ELECTRON DEVICE LETTERS, 32 (2011)

[80] M. Sujata, S. Bhargava, S. Sangal, J. Mater. Sci. Lett. 16 (1997) 1175

[81] R. Pretorius, A. M. Vredenberg, F. W. Saris, R. de Reus, J. Appl. Phys. 70 (1991) 3636

[82] F. A. Padovani, R. Stratton Solid-State Electron. 9 (1966) 695

[83] Y.J. Lin, Y.M. Chen, T.J. Cheng, Q. Ker J. Appl. Phys. 95 (2004) 571

[84] B.P. Luther, S.E. Mohney, T.N. Jackson, M.A. Khan, Q. Chen, J.W. Yang, Appl.Phys. Lett. 70 (1997) 57

[85] A. Motayed, R. Bathe, M.C. Wood, O.S. Diouf, R.D. Vispute, S.N. Mohammad, J.Appl. Phys. 93 (2003) 1087

[86] M. Hajlasz, J. J. T. M. Donkers, S. J. Sque, S. B. S. Heil, D. J. Gravesteijn, F. J. R. Rietveld, J. Schmitz Appl. Phys. Lett. 104 (2014) 242109

[87] G. El-Zammar W. Khalfawoui, T. Oheix, A. Yvon, E. Collard, F. Cayrel, Materials Science in Semiconductor Processing 78 (2018) 107–110

[88] G. K. Reeves and H. B. Harrison, IEEE Electron Device Lett., vol EDL-3 (1982) 111-113.

[89] F. Iucolano, F. Roccaforte, A. Alberti, C. Bongiorno, S. Di Franco, V. Raineri, J. Appl. Phys. 100 (2006) 123706

[90] J. G. J. Chern and W. G. Oldam, IEEE Electron Device Lett. EDL-5 (1984) 178-180

[91] N. Lundberg, M. Ostling, Solid State Electron. 39 (1996) 1559

[92] H.G. Henry, IEEE Trans. Electron Devices 36 (1989) 1390

93 H.P. Kattelus, J.L. Tandon, M.-A. Nicolet, Solid-State Electron. 29 (1986) 903.

[94] G. K. Reeves, P. W. Lçeech and H. B. Harrison, Solid State El., 38 (1995) 745-751.

[95] M. Ahmad, A.P. Shah, D.K. Sharma, N.R. Roy and B. R. Arora, Solid State Electron., 46 (2002) 505-512.

[96] T. Kimoto, J. Cooper, Fundamentals of Silicon Carbide Technology: Growth, Characterization, Devices and Applications, John Wiley & Sons, Singapore Pte. Ltd., 2014.

[97] J. Wong-Leung, M.S. Janson, A. Kuznetsov, B.G. Svensson, M.K. Linnarsson, A. Hallén, C. Jagadish, D.J.H. Cockayne, Nucl. Istr. Meth. B 266 (2008) 1367-1372

[98] Y. Negoro, T. Kimoto, H. Matsunami, F. Schmid, G. Pensl, J. Appl. Phys. 96 (2004) 4916-4922

[99] H. Fujihara, J. Suda, T. Kimoto, Jpn. J. Appl. Phys. 56 (2017) 070306

[100] J. Pernot, S. Contreras, J. Camassel, J. Appl. Phys. 98 (2005) 023706

[101] M. Rambach, A.J. Bauer, H. Ryssel, phys. stat. sol. (b) 245 (2008) 1315-1326

[102] M. Rambach, A.J. Bauer, H. Ryssel Materials Science Forum, 556-557 (2007) pp 587-590

[103] A. Parisini, R. Nipoti, J. Appl. Phys. 114 (2013) 243703

[104] D. K. Schroder, T. T. Braggins, and H. M. Hobgood, J. Appl. Phys. 49 (1978) 5256 (1978)

[105] A. Koizumi, J. Suda, T. Kimoto, J. Appl. Phys. 106 (2009) 013716

[106] G. Pensl, F. Schmid, F. Ciobanu, M. Laube, S. A. Reshanov, N. Schulze, K. Semmelroth, H. Nagasawa, A. Schöner, G. Wagner, Mater. Sci.Forum 433-436 (2003) pp 365-370

[107] S. Asada, T. Okuda, T. Kimoto and J. Suda Appl. Phys. Express 9 (2016) 041301

[108] M. Vivona, G. Greco, C. Bongiorno, R. Lo Nigro, S. Scalese, F. Roccaforte, Appl. Surf. Sc. 420 (2017) 331–335

[109] F. Roccaforte, F. La Via, V. Raineri, Int. J. High Speed Electron. Syst. 15 (2005) 781

[110] J. Crofton, S.E. Mohney, J.R. Williams, T. Isaacs-Smith, Solid-State Electron. 46 (2002) 109

[111] B.J. Johnson, M.A. Capano, Solid-State Electron. 47 (2003) 1437

[112] La Via, F. Roccaforte, A. Makhtari, V. Raineri, P. Musumeci, and L. Calcagno, Microelectron. Eng. 60 (2002) 269

[113] H. Tamaso, S. Yamada, H. Kitabayashi, T. Horii, Mater. Sci. Forum 778–780 (2014) 669

[114] P. Fedeli, M. Puzzanghera, F.Moscatelli, R.A. Minamisawa, G. Alfieri, U. Grossner, R.
Nipoti, Mater. Sci. Forum 897 (2017) 391

[115] A. Frazzetto, F. Giannazzo, R. Lo Nigro, V. Raineri, F. Roccaforte, J. Phys. D: Appl. Phys. 44, (2011) 255302

[116] F. Giannazzo, M. Rambach, D. Salinas, F. Roccaforte, and V. Raineri, Mater. Sci. Forum 615-617 (2009) 457-460

[117] R. Nipoti, A. Nath, M. V. Rao, A. Hallen, A. Carnera, Y. L. Tian, Applied Physics Express 4 (2011) 111301

[118] N. S. Saks, A. V. Survov, D. C. Capell, High temperature high dose implantation of aluminumin 4H-SiC, Appl. Phys. Lett. 84 (2004) 5195

[119] F. Roccaforte, M. Vivona, G. Greco, R. Lo Nigro, F. Giannazzo, S. Rascunà, M. Saggio, Mater. Sci. Forum 924 (2018) 339-344

[120] G. L. Pearson and J. Bardeen, Phys. Rev. 75 (1949) 865

[121] M. Kocher, B. Yao, J. Weisse, M. Rommel, Z.W. Xu, T. Erlbacher, A.J. Bauer, Mater. Sci. Forum 963 (2019) 445-448.

[122] A. Scorzoni, F. Moscatelli, A. Poggi, G.C. Cardinali, R. Nipoti, Mater. Sci. Forum 457-460 (2004) 881-884.

[123] J.I. Noh, K.S. Nahm, K.C. Kim, M.A. Capano, Solid-State Electronics 46 (2002) 2273

[124] J. Eriksson, M.H. Weng, F. Roccaforte, F. Giannazzo, S. Leone, and V. Raineri, Appl. Phys. Lett. 95 (2009) 081907

[125] A.E. Bazin, J.F. Michaud, C. Autret-Lambert, F. Cayrel, T. Chassagne, M. Portail, M. Zielinski, E. Collard, D. Alquier, Mater. Sci. Eng. B 171 (2010) 120

[126] M. Spera , G. Greco, R. Lo Nigro, S. di Franco, D. Corso, P. Fiorenza, F. Giannazzo, M. Zielinski, F. La Via, F. Roccaforte, Materials Science Forum, 963 (2019) 485-489

[127] F. Li, et al., IEEE Electron Device Lett. 37 (2016) 1189

[128] J. A. Edmond, J. Ryu, J. T. Glass, R. F. Davis, J. Electrochem. Soc. 135 (1988) 359

[129] A. Moki, P. Shenoy, D. Alok, B. J. Baliga, K. Wongchotigul, M. G. Spencer, J. Electronic Mat. 24 (1995) 315

[130] R. Anzalone, S. Privitera, M. Camarda, A. Alberti, G. Mannino, P. Fiorenza, S. Di Franco, F. La Via, Mater. Sci. Engineering B 198 (2015) 14-19

[131] Joint Committee of Powder Diffraction Standards, PDF card 01-1119

[132] Joint Committee of Powder Diffraction Standards, PDF card 03-0943